

國立臺灣大學工學院環境工程學研究所

碩士論文

Graduate Institute of Environmental Engineering

College of Engineering

National Taiwan University

Master Thesis



以錳銻氧化物與石墨烯複合材於

不同反應環境進行低溫脫硝

Low-temperature NO<sub>x</sub> removal under different  
atmospheres over cerium and manganese oxide  
supported graphene-based materials

諸安均

An-Chun Chu

指導教授：席行正 博士

Advisor: Hsing-Cheng Hsi, Ph.D.

中華民國 109 年 7 月

July 2020



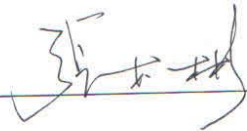
國立臺灣大學碩士學位論文  
口試委員會審定書

以錳銻氧化物與石墨烯複合材於  
不同反應環境進行低溫脫硝

Low-temperature NO<sub>x</sub> removal under different atmospheres  
over cerium and manganese oxide supported graphene-based  
materials

本論文係諸安均君(學號 R07541103)在國立臺灣大學環境工程學研究所完成之碩(博)士學位論文，於民國 109 年 7 月 23 日承下列考試委員審查通過及口試及格，特此證明

論文審查委員：

  
\_\_\_\_\_

張木彬博士  
國立中央大學環境工程研究所特聘教授


  
\_\_\_\_\_

林坤儀博士  
國立中興大學環境工程系教授

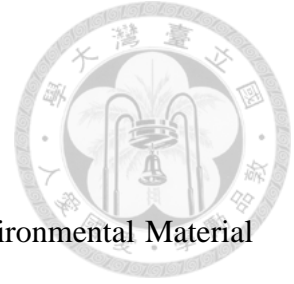
  
\_\_\_\_\_

林亮毅博士  
國立交通大學環境工程研究所助理教授

指導教授：  
\_\_\_\_\_

所 長：  
\_\_\_\_\_

## Acknowledgement



This work is mainly supported by the Air Pollution And Environmental Material Lab. Thanks for the guide and suggestion from professor Hsing-Cheng Hsi and the knowledge exchange from the members of Air Pollution And Environmental Material Lab. Thanks for the devices support and education from Chih-Fu Tseng for TPD and TPR in Taiwan Power Research Institute, Taiwan Power Company.

## 中文摘要



鍋爐燃燒產生之氣狀污染物包含會導致酸雨及次級污染物形成的氮氧化物，故須加處理。現行主要移除方法之一為以氨氣或尿素為還原劑，金屬氧化物做為觸媒的選擇性觸媒還原法(selectivity catalytic reduction, SCR)。該法常用觸媒為鈳鎢鈦複合氧化物觸媒。該法缺點包括所需溫度較高、氨氣為一工安上的可能危險來源，以及廢棄觸媒中的鈳具有毒性等。故大量團隊投入以其他金屬複合物於更低溫度進行不同程序之氮氧化物移除研究。本研究以超音波震盪含浸法合成數種不同氧化石墨烯添加量、錳鈰比例不同 (錳鈰比: 4:1 或 8:1)的錳鈰氧化物與石墨烯複合材( $\text{MnO}_x\text{-CeO}_x\text{-GO}$ )觸媒，並探討了數種  $\text{MnO}_x\text{-CeO}_x\text{-GO}$  觸媒於添加氨氣的還原條件與不添加的氧化條件，不同溫度下對氮氧化物以還原或氧化來進行移除之結果，並以二氧化錳、錳鈰氧化物( $\text{MnO}_2\text{-CeO}_x$ )與錳氧化物與石墨烯複合材( $\text{MnO}_x\text{-GO}$ ) 觸媒比較。實驗結果發現不同 GO 添加量的  $\text{MnO}_x\text{-CeO}_x\text{-GO}$  觸媒於  $60^\circ\text{C}$  到  $120^\circ\text{C}$  於  $\text{NH}_3\text{-SCR}$  條件進行脫硝時具有至少 50% 的 NO 轉化率。最佳者於  $150^\circ\text{C}$  即具有 95% 轉化率，但在更高的溫度其  $\text{NO}_2$  產生量較多。該類觸媒亦能促進 NO 之氧化。於  $240^\circ\text{C}$  到  $270^\circ\text{C}$  具有 80% 以上的轉化率。物化分析結果顯示， $\text{MnO}_x\text{-CeO}_x\text{-GO}$  觸媒具有較多的路易斯酸吸附位、較高的氧化物種移動活性，且金屬活性物較分散，這些特性的協同作用使得  $\text{MnO}_x\text{-CeO}_x\text{-GO}$  觸媒具有好的 low temperature SCR 活性。

對於水氣、二氧化硫等致毒化物種的耐性測試，結果顯示於  $180^\circ\text{C}$  時進行含水氣的 low temperature SCR， $\text{MnO}_x\text{-CeO}_x\text{-GO}$  觸媒具有優異的抗水氣能力，轉化率的恢復也極優異。於二氧化硫的影響下，雖  $180^\circ\text{C}$  時  $\text{NH}_3\text{-SCR}$  轉化率會降低到 40% 到 60%，但  $270^\circ\text{C}$  可保有 70% 到 90% 的轉化率，代表於含硫煙氣下，發生於  $\text{MnO}_x\text{-CeO}_x\text{-GO}$  觸媒表面的毒化大部分為硫酸銨鹽造成，可藉由高溫分解。

關鍵字：氮氧化物、選擇性催化還原、催化氧化、錳鉀氧化物、氧化石墨烯




## Abstract



The gaseous pollutants caused by boiler combustion include different amounts of  $\text{NO}_x$ , which cause the irritation of the respiratory tract and also lead to the formation of acid rain and secondary pollutants. Therefore, the control of these pollutants must be implemented. One of the conventional pollution control methods, selective catalytic reduction, abbreviated as “SCR”, is a universal used process that uses ammonia or urea as reducing agents to reduce  $\text{NO}_x$  with the help of specific catalysts. Vanadium/tungsten/titanium oxide catalysts are popular for the SCR process. The disadvantages of SCR process include high temperature requirement, potential industrial safety concerns due to ammonium storage, and the toxicity of vanadium in waste catalysts. Therefore, studies pertaining to using different types of catalysts to remove  $\text{NO}_x$  at lower temperatures in different processes have been extensively studied.

In this study, several kinds of manganese-cerium oxides and graphene composites ( $\text{MnO}_x\text{-CeO}_x\text{-GO}$ ) catalysts with different amounts of GO and two Mn/Ce ratios (8 and 4) were synthesized by the ultrasonication impregnation method. NO removal efficiency of those catalysts in different temperatures by  $\text{NH}_3\text{-SCR}$  and NO oxidation were investigated.  $\text{MnO}_2$ ,  $\text{MnO}_2\text{-CeO}_x$ , and  $\text{MnO}_x\text{-GO}$  catalysts were also used to compare with the  $\text{MnO}_x\text{-CeO}_x\text{-GO}$  catalysts.



The result showed that  $\text{MnO}_x\text{-CeO}_x\text{-GO}$  catalysts with different GO loading exhibited at least 50% conversion activity for low-temperature  $\text{NH}_3\text{-SCR}$  reaction condition over  $60^\circ\text{C}$  to  $120^\circ\text{C}$ . The best NO conversion was found to be 95% at  $150^\circ\text{C}$ , but they would generate a large amount of  $\text{NO}_2$  at higher temperatures.  $\text{MnO}_x\text{-CeO}_x\text{-GO}$  catalysts also possessed excellent catalytic activity for NO oxidation, which could achieve up to 80% oxidation activity around  $240^\circ\text{C}$  to  $270^\circ\text{C}$ . The results of physicochemical characterization indicate that  $\text{MnO}_x\text{-CeO}_x\text{-GO}$  exhibits better low-temperature  $\text{NH}_3\text{-SCR}$  activity due to the synergistic effect of more Lewis acid sites, higher oxygen species mobility, and higher dispersion of metal oxides.

For the reactive species tolerance,  $\text{MnO}_x\text{-CeO}_x\text{-GO}$  catalysts showed outstanding water tolerance when  $\text{NH}_3\text{-SCR}$  was operated at  $180^\circ\text{C}$ . For the sulfur tolerance, although the NO conversion of  $\text{NH}_3\text{-SCR}$  at  $180^\circ\text{C}$  in the presence of  $\text{SO}_2$  decreased to about 40% to 60%, it could still maintain 70% to 90% NO conversion when  $\text{NH}_3\text{-SCR}$  was  $270^\circ\text{C}$ , which implies that the main cause of the  $\text{SO}_2$  poisoning effect is the formation of ammonium sulfate species that could decompose at a higher temperature.

**Keywords: nitrogen oxides, selective catalytic reduction, catalytic oxidation, Mn-Ce oxides, graphene oxide**

## Content

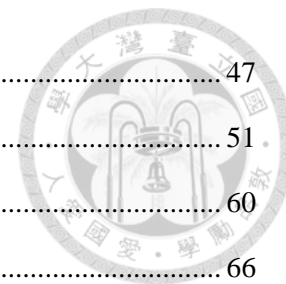


Acknowledgement.....	I
中文摘要.....	II
Abstract .....	IV
Content .....	VI
List of Table .....	IX
List of Figure.....	X
Chapter 1. Introduction .....	1
1.1. Motivation.....	1
1.1.1. Narrow and high operation temperature window .....	1
1.1.2. Toxicity .....	2
1.2. Possible solution .....	2
1.3. Research objective .....	3
Chapter 2. Literature review .....	5
2.1. Generation and environmental impact of NO <sub>x</sub> .....	5
2.2. Emission controlling technique of nitrogen oxide .....	8
2.3. Post-combustion control .....	9
2.3.1. Absorption .....	10
2.3.2. Adsorption .....	10
2.3.3. Electron beam.....	11
2.3.4. NH <sub>3</sub> -SCR .....	12
2.3.5. SNCR.....	19
2.4. Reaction parameter effect on NH <sub>3</sub> -SCR .....	20
2.4.1. Effect on temperature .....	20



2.4.2.	Effect of NH <sub>3</sub> /NO molar ratio .....	21
2.4.3.	Effect of H <sub>2</sub> O and SO <sub>2</sub> .....	22
2.5.	Mn-based catalysts for low-temperature NO <sub>x</sub> removal.....	24
2.5.1.	Metal modification .....	25
2.5.2.	Support modification .....	28
Chapter 3.	Materials and methods.....	30
3.1.	Research framework .....	30
3.2.	Preparation of graphene oxide and catalyst .....	30
3.2.1.	Synthesis of GO by Hummers' method.....	30
3.2.2.	Ultrasonication impregnation of MnO <sub>x</sub> -CeO <sub>x</sub> graphene-based composites .....	31
3.2.3.	Synthesis of MnO <sub>2</sub> and MnO <sub>2</sub> -CeO <sub>x</sub> .....	32
3.3.	Physicochemical characterization of catalyst .....	34
3.3.1.	Surface area and pore volume .....	34
3.3.2.	Scanning electronic Microscopy .....	34
3.3.3.	X-ray diffraction measurement (XRD).....	34
3.3.4.	X-ray photoelectron spectroscopy (XPS).....	35
3.3.5.	NH <sub>3</sub> -Temperature Programmed Desorption (NH <sub>3</sub> -TPD).....	35
3.3.6.	H <sub>2</sub> - Temperature Programmed Desorption (H <sub>2</sub> -TPR) .....	36
3.3.7.	O <sub>2</sub> - Temperature Programmed Desorption (O <sub>2</sub> -TPD) .....	36
3.3.8.	Thermogravimetric analysis (TGA) .....	37
3.4.	NO removal test.....	37
3.4.1.	NH <sub>3</sub> -SCR and NO oxidation activity test.....	39
3.4.2.	Sulfur and water tolerance over NH <sub>3</sub> -SCR.....	39
Chapter 4.	Results and Discussion .....	41
4.1.	Physicochemical characterization of catalyst .....	41
4.1.1.	Surface area and pore volume .....	41
4.1.2.	Scanning electronic Microscopy .....	42

4.1.3.	X-ray diffraction measurement (XRD).....	47
4.1.4.	X-ray photoelectron spectroscopy (XPS).....	51
4.1.5.	NH <sub>3</sub> -Temperature Programmed Desorption (NH <sub>3</sub> -TPD).....	60
4.1.6.	H <sub>2</sub> -Temperature Programmed Desorption (H <sub>2</sub> -TPR) .....	66
4.1.7.	O <sub>2</sub> - Temperature Programmed Desorption (O <sub>2</sub> -TPD) .....	70
4.1.8.	Thermogravimetric analysis (TGA) .....	75
4.2.	NO removal test.....	78
4.2.1.	NH <sub>3</sub> -SCR and NO oxidation activity test.....	78
4.2.2.	Sulfur and water tolerance over NH <sub>3</sub> -SCR.....	83
4.3.	Comprehensive discussion.....	94
Chapter 5.	Conclusion and Recommendations .....	96
5.1.	Conclusion .....	96
5.2.	Recommendations for future work .....	97
Reference.....		98



## List of Table



Table 2-1. Total emissions of NO <sub>x</sub> (thousands of tons) in the United States.....	7
Table 2-2. Common NO <sub>x</sub> control technologies <sup>9</sup> .....	9
Table 3-1. Test parameter .....	38
Table 4-1. Porous structure parameter of the catalyst. ....	42
Table 4-2. Atomic surface compositions of catalysts obtained from XPS. ....	58
Table 4-3. Quantitative analysis of NH <sub>3</sub> -TPD over catalysts. ....	64
Table 4-4. Quantitative analysis of H <sub>2</sub> -TPR over catalysts. ....	69
Table 4-5. Quantitative analysis of O <sub>2</sub> -TPD over catalysts. ....	73

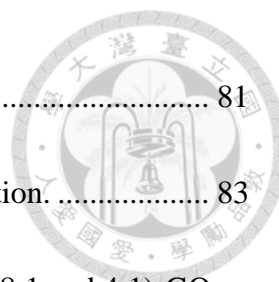
## List of Figure



Figure 1-1. Configuration of air pollution of the control device <sup>1</sup> .....	2
Figure 2-1. Mechanism for the atmospheric oxidation of VOCs and their derivatives....	6
Figure 2-2. Scheme of Langmuir–Hinshelwood (L–H) mechanism and the Eley–Rideal (E–R) mechanism of the NH <sub>3</sub> -SCR <sup>25</sup> . ....	13
Figure 2-3. Chemistry of fast SCR reaction over V <sub>2</sub> O <sub>5</sub> –WO <sub>3</sub> /TiO <sub>2</sub> SCR catalysts <sup>31</sup> ....	15
Figure 2-4. Proposed structure for ammonia adsorbed on V <sub>2</sub> O <sub>5</sub> -TiO <sub>2</sub> : (a) Lewis acid sites bonded NH <sub>3</sub> on Ti (b) H-bonded NH <sub>3</sub> on oxides sites (c) Lewis acid sites bonded NH <sub>3</sub> at vandyl surface site (d) Bronsted acid sites bonded NH <sub>4</sub> <sup>+</sup> <sup>21</sup> .....	16
Figure 2-5. Characteristic diagram for the relation between SCR activity and different temperatures <sup>51</sup> .....	20
Figure 2-6. Characteristic diagram for the relation between SCR activity and temperature over different catalysts <sup>51</sup> .....	21
Figure 2-7. Relation between SCR activity and different NH <sub>3</sub> concentrations in different gas hour space velocity <sup>52</sup> .....	22
Figure 2-8. Effect of the H <sub>2</sub> O and SO <sub>2</sub> poisoning effect during SCR <sup>53</sup> .....	22
Figure 2-9. The proposed mechanism of SO <sub>2</sub> deactivation effect on the SCR reaction. <sup>59</sup> .....	24

Figure 2-10. Scheme about the interaction between SO <sub>2</sub> and MnO <sub>2</sub> <sup>62</sup> .....	25
Figure 2-11. Promotion effect of co-doped metals on Mn/TiO <sub>2</sub> in the NH <sub>3</sub> -SCR.....	27
Figure 2-12. N <sub>2</sub> selectivity and catalytic performance of Mn-M/TiO <sub>2</sub> catalysts <sup>66</sup> .....	27
Figure 3-1. The flow chart of the research framework.....	30
Figure 3-2. The steps of synthesis of MnO <sub>x</sub> -CeO <sub>x</sub> -GO catalysts and MnO <sub>x</sub> -GO catalysts. .....	32
Figure 3-3. The steps of synthesis of MnO <sub>2</sub> and MnO <sub>2</sub> -CeO <sub>x</sub> catalysts.....	33
Figure 3-4. Experimental apparatus for fixed-bed NO <sub>x</sub> removal. ....	37
Figure 4-1. SEM images of MnO <sub>2</sub> (a, b), MnO <sub>2</sub> -CeO <sub>x</sub> (8:1) (c, d) and MnO <sub>2</sub> -CeO <sub>x</sub> (4:1) (e, f) .....	44
Figure 4-2. SEM images of MnO <sub>2</sub> -CeO <sub>x</sub> (8:1)-GO catalyst with 0.3 wt% GO (a, b), 2 wt% GO (c, d) and 4 wt% GO (e, f) .....	45
Figure 4-3. SEM images of MnO <sub>2</sub> -CeO <sub>x</sub> (4:1)-GO catalyst with 0.3 wt% GO (a, b), 2 wt% GO (c, d) and 4 wt% GO (e, f) .....	46
Figure 4-4. SEM images of MnO <sub>x</sub> - GO catalysts with 0.3 wt% (a, b) and 4 wt% (c, d)	47
Figure 4-5. XRD pattern of (a) MnO <sub>x</sub> -GO, (b) MnO <sub>2</sub> -CeO <sub>x</sub> (4:1)-GO and (c) MnO <sub>x</sub> - CeO <sub>x</sub> (8:1)-GO catalysts with different amounts of GO addition. ....	50
Figure 4-6. XPS spectra of Ce 3d (a), O 1s (b) and Mn 2p <sub>2/3</sub> (c) in MnO <sub>2</sub> and MnO <sub>2</sub> -	

CeO <sub>x</sub> catalysts.....	54
Figure 4-7. XPS spectra of O 1s (a) and Mn 2p <sub>2/3</sub> (b) in MnO <sub>x</sub> -GO catalyst.....	55
Figure 4-8. XPS spectra of Ce 3d (a), O 1s (b) and Mn 2p <sub>2/3</sub> (c) in MnO <sub>x</sub> -CeO <sub>x</sub> (8:1)-GO catalysts. ....	56
Figure 4-9. XPS spectra of Ce 3d (a), O 1s (b) and Mn 2p <sub>2/3</sub> (c) in MnO <sub>x</sub> -CeO <sub>x</sub> (4:1)-GO catalysts. ....	57
Figure 4-10. NH <sub>3</sub> -TPD profile over catalyst.....	63
Figure 4-11. H <sub>2</sub> -TPR profile over catalysts.....	68
Figure 4-12. O <sub>2</sub> -TPD profile over catalyst.....	72
Figure 4-13. TGA curves of MnO <sub>x</sub> -GO, MnO <sub>2</sub> -CeO <sub>x</sub> (4:1)-GO and MnO <sub>x</sub> -CeO <sub>x</sub> (8:1)-GO catalysts with different amounts of GO addition.....	77
Figure 4-14. NO conversion and NO <sub>2</sub> formation of MnO <sub>x</sub> -CeO <sub>x</sub> (8:1)-GO catalysts with different amounts of GO over the NH <sub>3</sub> -SCR.....	79
Figure 4-15. NO conversion and NO <sub>2</sub> formation of MnO <sub>x</sub> -CeO <sub>x</sub> (4:1)-GO catalysts with different amounts of GO over the NH <sub>3</sub> -SCR.....	79
Figure 4-16. NO conversion and NO <sub>2</sub> formation of MnO <sub>2</sub> and MnO <sub>2</sub> -CeO <sub>x</sub> catalysts over the NH <sub>3</sub> -SCR. ....	80
Figure 4-17. NO conversion and NO <sub>2</sub> formation of MnO <sub>x</sub> -GO catalysts with different	



amounts of GO over the NH <sub>3</sub> -SCR. ....	81
Figure 4-18. NO conversion of different catalysts over the NO oxidation. ....	83
Figure 4-19. Sulfur tolerance test for NO conversion of MnO <sub>x</sub> -CeO <sub>x</sub> (8:1 and 4:1)-GO over the NH <sub>3</sub> -SCR activity test at 180°C.....	85
Figure 4-20. Sulfur tolerance test for NO conversion of MnO <sub>x</sub> -CeO <sub>x</sub> (8:1 and 4:1)-GO over the NH <sub>3</sub> -SCR activity test at 270°C .....	87
Figure 4-21. Water tolerance test for NO conversion of (a) MnO <sub>x</sub> -CeO <sub>x</sub> (8:1)-GO catalysts and (b) MnO <sub>x</sub> -CeO <sub>x</sub> (4:1)-GO catalysts over the NH <sub>3</sub> -SCR activity test at 180°C. ....	92
Figure 4-22. Water and sulfur tolerance test for NO conversion of MnO <sub>x</sub> -CeO <sub>x</sub> (8:1)-GO over the NH <sub>3</sub> -SCR activity test at 270°C.....	93
Figure 4-23. Proposed mechanism of NO <sub>x</sub> removal over MnO <sub>x</sub> -CeO <sub>x</sub> -GO catalysts. (a): in the absence of SO <sub>2</sub> ; (b): in the presence of SO <sub>2</sub> .....	94

## Chapter 1. Introduction



### 1.1. Motivation

The gaseous pollutants caused by boiler combustion include different amounts of  $\text{NO}_x$ ,  $\text{SO}_x$ , and even mercury, depending on the composition of the fuel and the combustion parameters, lead to irritation in the respiratory tract, and the formation of acid rain and secondary pollutants. Therefore, the control of these pollutants becomes extremely important. Commercial SCR catalyst beds often use vanadium pentoxide ( $\text{V}_2\text{O}_5$ ) as the prominent active component.  $\text{V}_2\text{O}_5$  could be mixed with  $\text{WO}_3$  (tungsten trioxide) and  $\text{TiO}_2$  (titanium dioxide) and be coated on the honeycomb-like catalyst carrier. This kind of catalyst product is widely used for the pollution control of fired power plants. However, it has two drawbacks, including a narrow and high operation temperature window and the toxicity of vanadium oxides.

#### 1.1.1. Narrow and high operation temperature window

A higher operation temperature window means that the catalyst bed needs to be installed at the relative upstream of the pollution control system in fired power plants or industrial energy supply unit. As shown in Figure 1-1, the position may be at the upstream of devices that will drop the temperature of flue gas, like ESP and WFGD. At this position, the catalyst will age due to the effect of sintering, abrasion, clogging and  $\text{SO}_2$  poisoning.



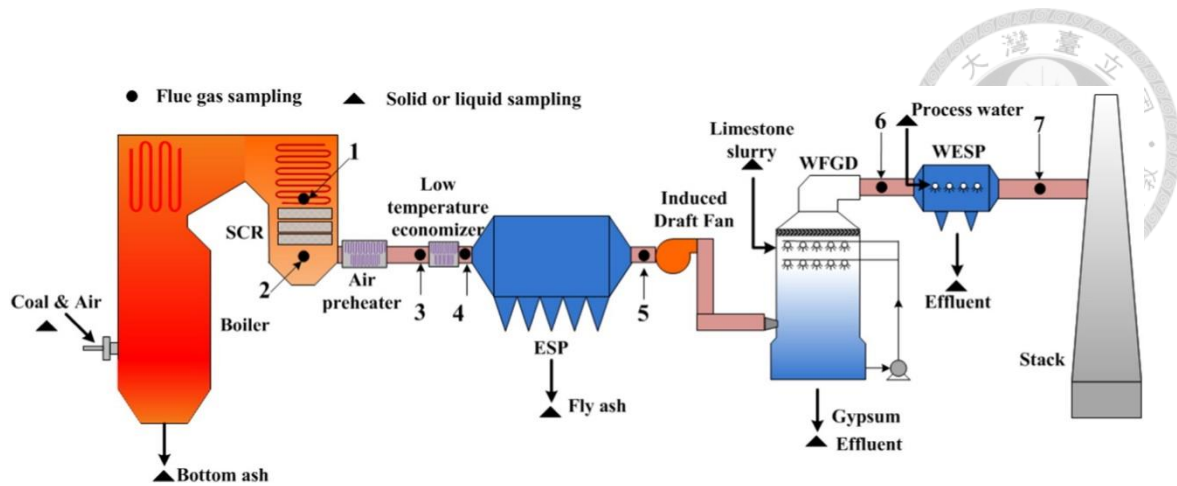


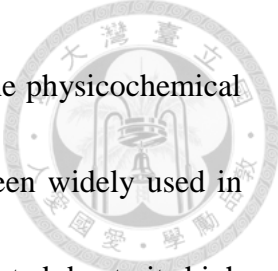
Figure 1-1. Configuration of air pollution of the control device <sup>1</sup>.

### 1.1.2. Toxicity

Vanadium pentoxide is highly toxic, which makes the poisonous catalyst bed become a harsh solid waste management problem <sup>2-3</sup>. Therefore, the development of new kinds of low-temperature SCR catalysts is essential.

### 1.2. Possible solution

To make up the above disadvantages, different ingredients of catalysts had been studied for the usage of SCR catalysts. Manganese oxide and Cerium oxide composite ( $MnO_x-CeO_x$ ) have been considered as the potential choice for the catalyst low temperature SCR due to excellent physicochemical properties including multi-valence chemical composition, efficient redox cycle, and oxygen storage and supply from cerium, which could enhance the SCR activity<sup>4-5</sup>.



Modification of support is also a common method to adjust the physicochemical properties of catalysts. Among them, carbon-based supports have been widely used in environmental catalyst. Graphene-based materials have been investigated due to its high electron conductivity and promotion of charge transfer, and some group found that graphene oxide (GO) could increase the low-temperature NH<sub>3</sub>-SCR activity<sup>6-7</sup>. However, the research about what roles the species in that kinds of composite catalysts individually play is still relative deficient.

### **1.3. Research objective**

In this research, MnO<sub>x</sub>-GO and MnO<sub>x</sub>-CeO<sub>x</sub>-GO with different amounts of GO and Mn/Ce ratios were synthesized by the ultrasonication impregnation method. MnO<sub>2</sub> and MnO<sub>2</sub>-CeO<sub>x</sub> were also synthesized to compare with MnO<sub>x</sub>-GO and MnO<sub>x</sub>-CeO<sub>x</sub>-GO. All of these catalysts were examined to comprehend the activity of NH<sub>3</sub>-SCR and NO oxidation. Several characterizations have been performed to understand the physicochemical and surface properties of the catalyst, including NH<sub>3</sub>-Temperature Programmed Desorption (NH<sub>3</sub>-TPD), H<sub>2</sub>-Temperature Programmed Desorption (H<sub>2</sub>-TPR), X-ray photoelectron spectroscopy (XPS), Brunauer-Emmett-Teller (BET) specific surface area and X-ray diffraction measurement (XRD).

The following are the objectives of this research:

1. Synthesize and characterize the  $\text{MnO}_x$ - $\text{CeO}_x$ -GO catalyst
2. Comprehend the interaction between  $\text{MnO}_x$ ,  $\text{CeO}_x$  and GO, and realize the effect on NO removal activity,  $\text{SO}_2$  tolerance and  $\text{H}_2\text{O}$  tolerance.



## Chapter 2. Literature review



### 2.1. Generation and environmental impact of NO<sub>x</sub>

Nitrogen oxides (NO<sub>x</sub>) not only contribute to the generation of acid rain but also take significant parts in photochemical cycles in the stratosphere, leading to the corrosion of buildings, acidification of the environmental medium, and the promotion of ozone depletion and secondary pollutant formation. NO can catalyze the dissociation of ozone through interactions with O<sub>3</sub> and O:



NO and NO<sub>2</sub> can also react with hydrogen-containing radical species and generate HNO<sub>3</sub>. Ozone, hydroxyl, and HNO<sub>3</sub> radicals can oxidize volatile organic compounds (VOCs). Low volatility organics generated through the VOCs' oxidation will further react with active species like ozone, HNO<sub>3</sub>, and oxygen-containing radicals, and promote the formation of photochemical smog that contains species like PANs and ozone. These strong oxidative species can irritate the respiratory tract and eyes.

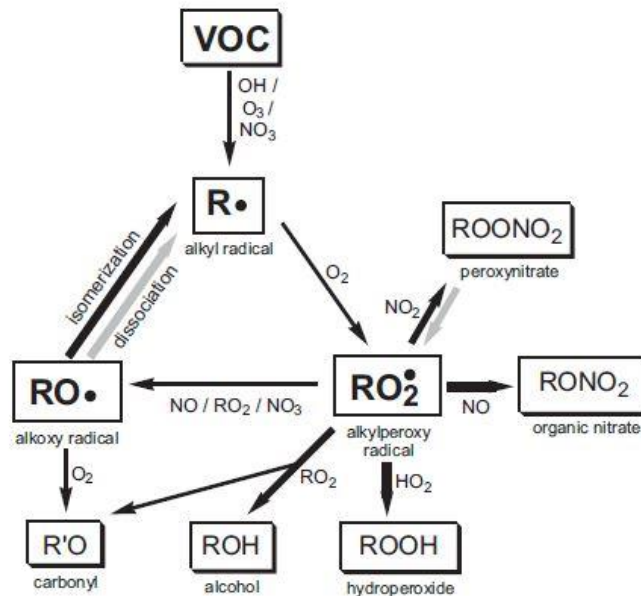


Figure 2-1. Mechanism for the atmospheric oxidation of VOCs and their derivatives.

8

Combustion contributes to the generation of most anthropogenic  $\text{NO}_x$  generation, which can be further divided into stationary sources and mobile sources. Table 2-1 shows the total emissions of  $\text{NO}_x$  in the United States from 2013 to 2018, with stationary sources contributing nearly 30% of the  $\text{NO}_x$  emissions in recent years.

Table 2-1. Total emissions of NO<sub>x</sub> (thousands of tons) in the United States.

Source category	2013	2014	2015	2016	2017	2018
Stationary fuel combustion	3567	3455	3149	2972	2840	2798
Industrial and other process	1276	1282	1282	1282	1282	1282
Transportation	8023	7599	7118	6756	6355	5953
Miscellaneous	373	294	294	294	294	294
Total	13269	12589	11843	11304	10771	10327

The ratio of the different components of NO<sub>x</sub> is nearly 9:1 of NO to NO<sub>2</sub>. According to the formation mechanism, NO<sub>x</sub> formed through combustion can be divided into three groups<sup>9</sup>: thermal NO<sub>x</sub>, prompt NO<sub>x</sub>, and fuel NO<sub>x</sub>. Thermal NO<sub>x</sub>, which contributes a significant part of the overall NO<sub>x</sub>, is generated by the oxidation of atmospheric nitrogen at a high temperature. The concentration of thermal NO<sub>x</sub> is dominated by the molar concentrations of nitrogen and oxygen and the combustion temperature. The ‘Zeldovich-mechanism’ is usually followed to describe the formation of thermal NO<sub>x</sub><sup>10</sup>:



In this mechanism, energy from high temperatures of up to 1800 K during combustion

dissociate oxygen and even break the triple bonds of nitrogen.

Prompt  $\text{NO}_x$  is often formed from nitrogen-containing species like HCN and  $\text{H}_2\text{CN}$ . It is generated from the reaction between hydrocarbon molecules and nitrogen, and will be oxidized to  $\text{NO}$  <sup>11</sup>.

Fuel  $\text{NO}_x$  is formed by the nitrogen-containing species in fuel.

## **2.2. Emission controlling technique of nitrogen oxide**

Based on the previously mentioned  $\text{NO}_x$  formation mechanism,  $\text{NO}_x$  control techniques can be processed through three concepts: fuel selection, combustion control, and post-combustion control. Fuel selection means using low-nitrogen-content fuel, like natural gas. Combustion control is a group of different kinds of methods that are designed to optimize different kinds of combustion parameters for inhibiting the formation of thermal  $\text{NO}_x$  and fuel  $\text{NO}_x$ . The main applied principles include controlling the flame temperature and reducing residence time <sup>9</sup>. They can be performed by different abatement techniques, like low  $\text{NO}_x$  burners.



Table 2-2. Common NO<sub>x</sub> control technologies <sup>9</sup>.

Technique	Description	Advantages	Disadvantages	Applicability
Less Excess Air (LEA)	Reduces oxygen availability	Easy Modification	Low NO reduction	All fuels
Off Stoichiometric Burners Out of Service (BOOS) Over Fire Air (OFA)	Staged combustion	Low cost	Higher airflow for CO High capital cost	-All fuels -Multiple burners for BOOS
Low NO <sub>x</sub> Burner (LNB)	Internal staged combustion	Low operating cost	Moderately high capital cost	All fuels
Flue Gas Recirculation (FGR)	<30% flue gas recirculated with air, decreasing temperature	High NO <sub>x</sub> reduction potential for low nitrogen fuels	- Moderately high capital cost and operating cost - Affects heat transfer and system pressures	-All fuels -Low nitrogen fuels
Water/Steam Injection	Reduces flame temperature	Moderate capital cost NO <sub>x</sub>	-Efficiency penalty -Fan power higher	All fuels
Reduced Air Preheat	Air not preheated, reduces flame temperature	High NO <sub>x</sub> reduction potential	Significant efficiency loss (1% per 40°F)	All fuels

### 2.3. Post-combustion control

Post-combustion control aims to remove the NO<sub>x</sub> from the exhaust gas after it has been formed, which can be performed by separating NO<sub>x</sub> into a different medium or chemically



breaking it down by reducing agents, oxidants, or high energy irradiation<sup>12-13</sup>. Flue gas parameters and the needs of other flue gas post-combustion pollution control equipment should be taken into consideration when designing the post-combustion control of NO<sub>x</sub>.



### **2.3.1. Absorption**

Absorption is used to remove NO<sub>x</sub> and SO<sub>x</sub> simultaneously by transferring the molecules into any medium that has more affinity to them than flue gas. In short, the process consists of a wet scrubber operating with different absorbents to remove water-soluble pollutants.

Absorption is not very efficient for NO<sub>x</sub> because NO is only slightly soluble. A proper absorbent could overcome this problem through different kinds of physicochemical mechanisms, like using a strong oxidant to oxidize NO into soluble NO<sub>2</sub><sup>14-15</sup>, neutralizing acidic SO<sub>x</sub> and NO<sub>x</sub>, or chelating NO<sub>x</sub> with a transition metal complex ion<sup>16</sup>.

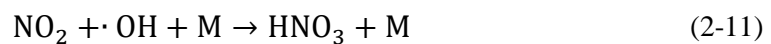
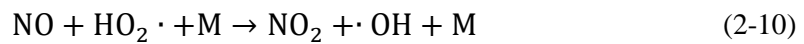
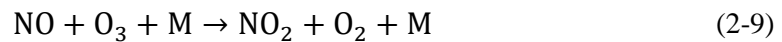
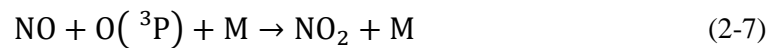
### **2.3.2. Adsorption**

Adsorption is a kind of dry method, which uses some materials, especially waste materials, to adsorb NO<sub>x</sub> and SO<sub>x</sub><sup>17</sup>. It is often operated in a specially designed reactor bed<sup>18</sup>.



### 2.3.3. Electron beam

By the irradiation of the electron beam, different molecules that exist in the flue gas will break down and generate ions and high energy radicals. The relative significant oxidants are  $\text{OH}\cdot$ ,  $\text{HO}_2$ , and  $\text{O}(^3\text{P})$ , which drive  $\text{NO}_x$  and  $\text{SO}_x$  through the oxidation pathway:

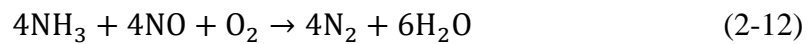


The combination of the usage of the electron beam devices with chemical scavengers<sup>19</sup> or microwaves<sup>20</sup> can further improve the removal efficiency. Devices like wet scrubbers remove oxidative species, such as  $\text{NO}_2$  and  $\text{HNO}_3$  more easily than  $\text{NO}$  from flue gas.

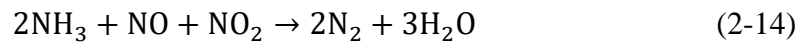
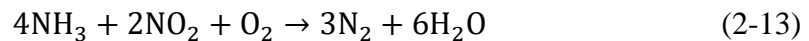


#### 2.3.4. NH<sub>3</sub>-SCR

Selective catalytic reduction (SCR) is a process that uses reducing agents, like ammonia or hydrocarbons, to reduce NO<sub>x</sub> to N<sub>2</sub> and H<sub>2</sub>O with the help of specific catalysts. In the case of NH<sub>3</sub> as the reducing agent, the following equation is the general SCR reaction<sup>21-22</sup>:



If NO<sub>2</sub> is present:



Eq. 2-14 is often called “fast SCR” reactions due to their higher reaction rate than SCR.

The following are the theoretically ideal parameters for SCR<sup>23-24</sup>:

1. The molar ratio of NO/NH<sub>3</sub> is near 1
2. Operation temperature is lower than 400°C
3. Low oxygen concentration



### 2.3.4.1. Mechanism of SCR

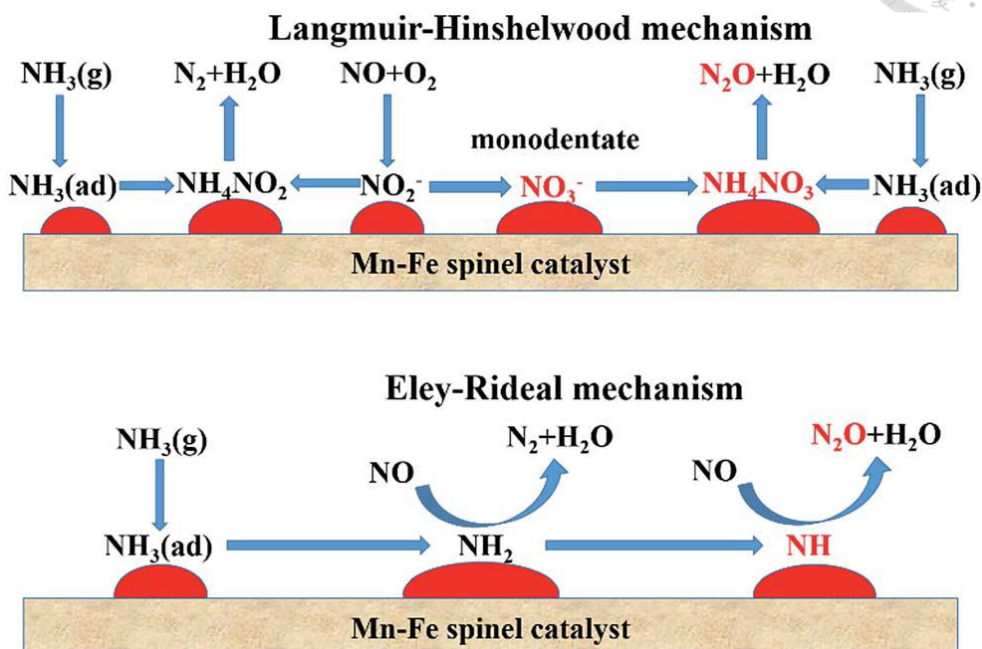
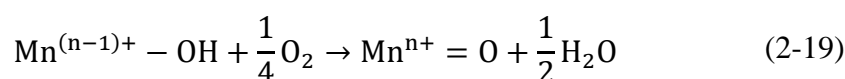
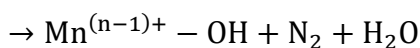
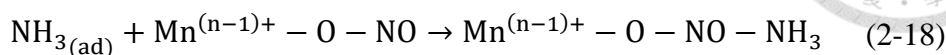
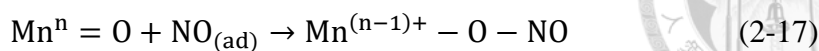


Figure 2-2. Scheme of Langmuir–Hinshelwood (L–H) mechanism and the Eley–Rideal (E–R) mechanism of the  $\text{NH}_3$ -SCR <sup>25</sup>.

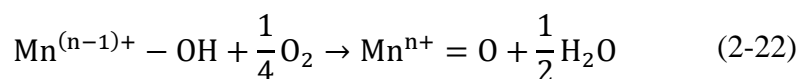
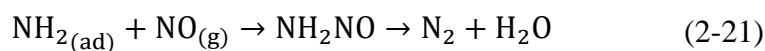
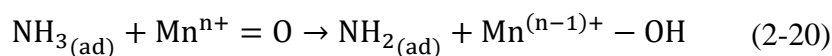
It is believed that the SCR reaction catalyzed by different kinds of catalysts follows both the Langmuir–Hinshelwood (L–H) mechanism and the Eley–Rideal (E–R) mechanism. The choice of mechanism depends on the nature of the catalysts. In the L-H mechanism,  $\text{NH}_3$  and  $\text{NO}$  have to be adsorbed on the surface of catalysts. Take the  $\text{MnO}_x$  catalyst as an example <sup>26-27</sup>:



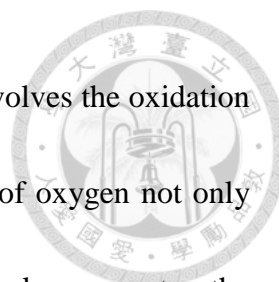


As the equations above describe, after the adsorption of  $\text{NH}_3$  and  $\text{NO}$ ,  $\text{NO}$  will be oxidized by surface active sites and interact with the adsorbed  $\text{NH}_3$ , generating and releasing nitrogen.

For the E-R mechanism, ammonia is activated as it is adsorbed onto the active sites of the catalyst, where gaseous  $\text{NO}$  will then react with the activated  $\text{NH}_3$  species to form  $\text{N}_2$  and  $\text{H}_2\text{O}$  <sup>28-30</sup>:



In the L-H and E-R mechanisms, oxygenated functional groups on surface bind with



adsorbed NO or adsorbed NH<sub>3</sub> respectively and activate it, which involves the oxidation and reduction of adsorbed species and metal oxides. The presence of oxygen not only makes sure that the oxidation state of catalysts can recover but also promotes the adsorption and oxidation of NO.

### 2.3.4.2. Mechanism of fast SCR

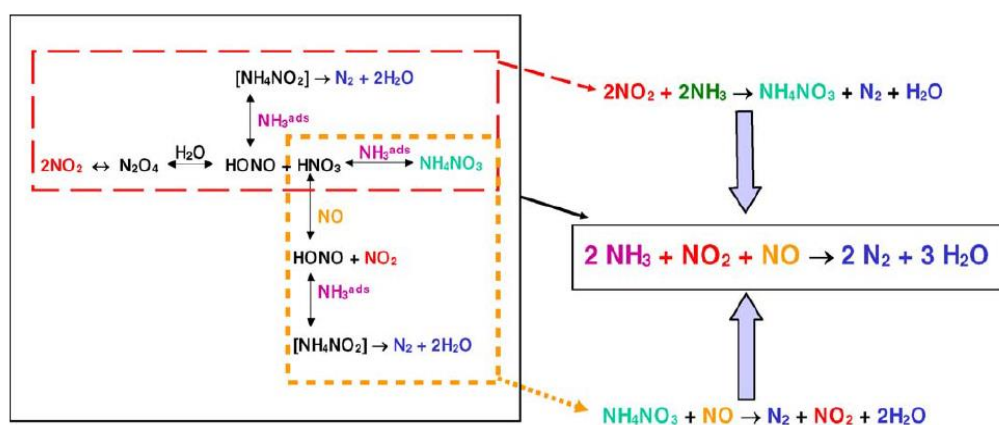


Figure 2-3. Chemistry of fast SCR reaction over V<sub>2</sub>O<sub>5</sub>–WO<sub>3</sub>/TiO<sub>2</sub> SCR catalysts<sup>31</sup>.

NO<sub>2</sub>, the result of NO oxidation, plays a significant role in the so-called “fast SCR”. Marbán, et al.<sup>32</sup> revealed that NO<sub>2</sub> reacts with adsorbed NH<sub>3</sub> species on the carbon-supported Mn<sub>3</sub>O<sub>4</sub>, making the reaction three times faster. Nova, et al.<sup>31</sup> proposed the mechanism of fast SCR over V<sub>2</sub>O<sub>5</sub>–WO<sub>3</sub>/TiO<sub>2</sub>. As shown in Figure 2-3, HNO<sub>3</sub> would form and react with the adsorbed NH<sub>3</sub> species after the dimerization and reaction between

H<sub>2</sub>O. Formed NH<sub>4</sub>NO<sub>2</sub> could then decompose to N<sub>2</sub>. Nova et al. mentioned that NH<sub>4</sub>NO<sub>3</sub> would be the terminal product in the absence of reducing agents like adsorbed NH<sub>3</sub> species to reduce it back to HNO<sub>3</sub>. Some research pointed out that <sup>33</sup> NH<sub>4</sub>NO<sub>3</sub> may react with NO at a higher temperature and generate N<sub>2</sub>, NO<sub>2</sub> and H<sub>2</sub>O. Liu, et al. <sup>34</sup> found that NO<sub>2</sub> can participate in the H-abstraction reaction with the hydroxyl group and coordinated NH<sub>3</sub> species, and subsequently promoted the formation of NH<sub>2</sub> species, which is a crucial intermediate for SCR.

#### 2.3.4.3. Reaction between adsorbed NH<sub>3</sub> species and adsorbed NO<sub>x</sub> species

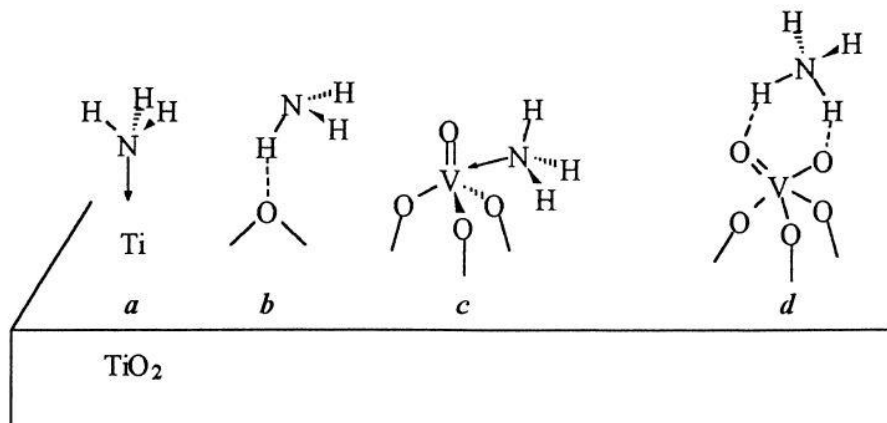
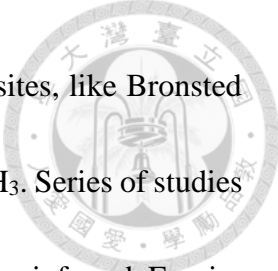


Figure 2-4. Proposed structure for ammonia adsorbed on V<sub>2</sub>O<sub>5</sub>-TiO<sub>2</sub>: (a) Lewis acid sites bonded NH<sub>3</sub> on Ti (b) H-bonded NH<sub>3</sub> on oxides sites (c) Lewis acid sites bonded NH<sub>3</sub> at vanadyl surface site (d) Bronsted acid sites bonded NH<sub>4</sub><sup>+</sup> <sup>21</sup>




As shown in Figure 2-4,  $\text{NH}_3$  can be adsorbed on different active sites, like Bronsted acid sites or Lewis acid sites, and form ionic  $\text{NH}_4^+$  and coordinated  $\text{NH}_3$ . Series of studies through physicochemical methods like TPD and diffuse reflectance infrared Fourier transform spectroscopy (DRIFTS) showed that  $\text{V}_2\text{O}_5\text{-TiO}_2$ ,  $\text{V}_2\text{O}_5\text{-WO}_3/\text{TiO}_2$  and  $\text{V}_2\text{O}_5\text{-MoO}_3\text{-TiO}_2$  displayed vigorous Bronsted acid sites and Lewis acid sites<sup>35-38</sup>. For some catalysts that were active at low or even room temperatures for SCR, like  $\text{CuO-TiO}_2$ <sup>39</sup>,  $\text{FeTiO}_2$ <sup>40</sup>,  $\text{CuO-MgO-Al}_2\text{O}_3$ <sup>41</sup> or  $\text{MnO}_x\text{-TiO}_2$ <sup>42</sup>, Bronsted acid sites were relatively seldom found. The zeolite-based catalysts and  $\text{MnO}_x\text{-Al}_2\text{O}_3$ <sup>43</sup> both had active sites determined to be found.

For NO adsorption, the adsorption and interaction on  $\text{V}_2\text{O}_5$  based catalysts, like  $\text{V}_2\text{O}_5\text{-TiO}_2$ ,  $\text{V}_2\text{O}_5\text{-SiO}_2$  and  $\text{V}_2\text{O}_5\text{-Al}_2\text{O}_3$ , are weak. For other transition metal oxides, adsorption of NO and the generation of NO-adsorbed species are more significant. Adsorbed NO will exist in different species and become other species with respect to changes in time and temperatures.

The kinds of species that tend to take part in SCR depend on the nature of catalysts, the composition of flue gas, and reaction temperature. Liu, et al.<sup>44</sup> found that  $\text{FeTiO}_x$  followed the L-H mechanism with the participation of Bronsted acid site-bonded  $\text{NH}_4^+$  and monodentate nitrate species at temperatures below  $200^\circ\text{C}$ . At a higher temperature,

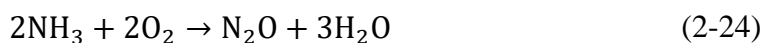
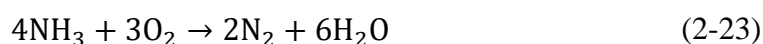


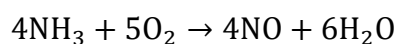


the E-R mechanism with the participation of Lewis acid site-bonded NH<sub>3</sub> species and gaseous NO or NO<sub>2</sub>. Guo, et al.<sup>45</sup> and Liu, et al.<sup>46</sup> also found that E-R mechanism tended to be followed at a higher temperatures (up to 200°C) for the Ce-TiO<sub>2</sub> catalyst, and the addition of Bi and Co would enhance the activity of Lewis acid sites, which led to the promotion of the L-H mechanism at a lower temperature. Gao, et al.<sup>47</sup> found that both Bronsted acid site-bonded and Lewis acid site-bonded NH<sub>3</sub> species take part in SCR, and the reaction mainly followed the L-H mechanism for CoO<sub>x</sub>-MnO<sub>x</sub>/biomass activated carbon catalysts. France, et al.<sup>48</sup> found that both Bronsted acid site-bonded and Lewis acid site-bonded NH<sub>3</sub> species take part in “fast SCR” for FeMnO<sub>x</sub>. Yang, et al.<sup>49</sup> proposed that Lewis acid site-bonded NH<sub>3</sub> species take part in NO<sub>x</sub> removal, and the main reaction mechanism is standard SCR for CuMn<sub>2</sub>O<sub>4</sub> by calculation through the Density Function Theory.

#### 2.3.4.4. Side reaction during the SCR process

Different side reactions take place during the SCR reaction:

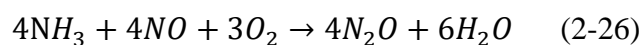




(2-25)



Eqs. 2-23 and 2-24 are referred to as “selective catalytic oxidation (SCO)” of  $\text{NH}_3$ . All these reactions have been observed for transition metal oxide catalysts during the SCR reaction. Generally, Eq. 2-23 is more favored than Eq. 2-25 at higher temperatures and vice versa, which may result from the fact that  $\text{N}_2$  is more thermodynamically stable at high temperatures than  $\text{N}_2\text{O}$  and  $\text{NO}$ . When the concentration of  $\text{NH}_3$  is high enough, the following reaction may take place, which results in unwanted  $\text{N}_2\text{O}$  formation, and implies the waste of excess  $\text{NH}_3$ <sup>25</sup>:



Moreover,  $\text{N}_2\text{O}$  can also be generated by the decomposition of  $\text{NO}$  and  $\text{NH}_4\text{NO}_3$  during the SCR reaction<sup>50</sup>.

### 2.3.5. SNCR

Selective non-catalytic reduction (SNCR) is a technique that aims to reduce  $\text{NO}_x$  to  $\text{N}_2$  by using reducing agents like urea or  $\text{NH}_3$  through similar reactions. However, without



the help of catalysts to lower the activation energy, the operation temperature is higher and varies from the choice of reducing agents. Ammonia is used in the range of 1560°F–1920°F, whereas urea is used in the range of 1830°F–2100°F <sup>12</sup>.

## 2.4. Reaction parameter effect on NH<sub>3</sub>-SCR

### 2.4.1. Effect on temperature

SCR activity increases with the increase of temperature. However, the activity of different kinds of side reactions may occur at a higher temperatures. The result of the competition is the bell-shaped SCR activity variation. The location of the optimized operation temperature window depends on the nature of the catalysts.

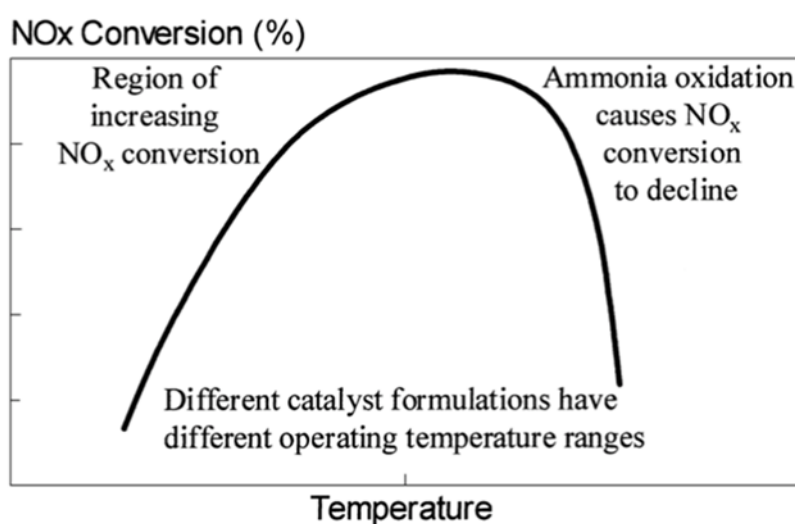


Figure 2-5. Characteristic diagram for the relation between SCR activity and different temperatures <sup>51</sup>.

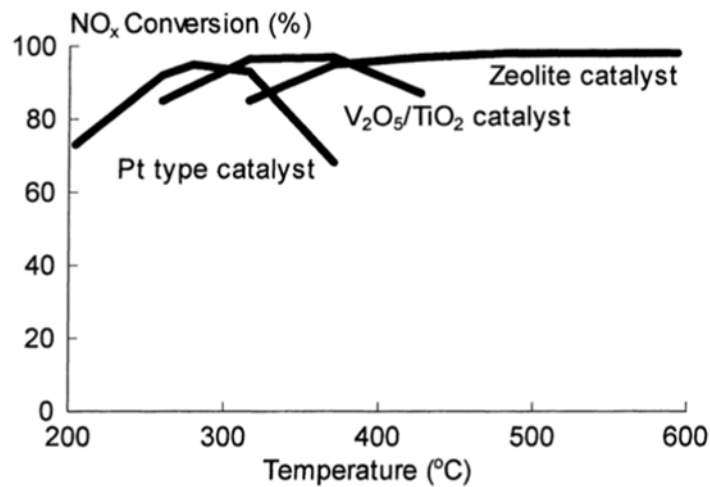


Figure 2-6. Characteristic diagram for the relation between SCR activity and temperature over different catalysts <sup>51</sup>.

#### 2.4.2. Effect of NH<sub>3</sub>/NO molar ratio

Theoretically, 1 mol NH<sub>3</sub> can remove 1 mol NO<sub>x</sub>. The deficiency of NH<sub>3</sub> will decrease the NO<sub>x</sub> removal efficiency. Overdose of NH<sub>3</sub> will result in a secondary pollutant and promote the formation of (NH<sub>4</sub>)<sub>2</sub>SO<sub>4</sub>. This occurs when the flue gas temperature is so low that (NH<sub>4</sub>)<sub>2</sub>SO<sub>4</sub> does not decompose, which causes fouling and lowers the efficiency of pollutant control devices. Generally, the amount of NH<sub>3</sub> slip should not exceed 5 mg/L. Figure 2-7 shows that SCR activity rises as the ratio of NH<sub>3</sub>/NO increases from 0.2 to 1, and when NH<sub>3</sub> is in excess, no more NH<sub>3</sub> can participate in the reaction.

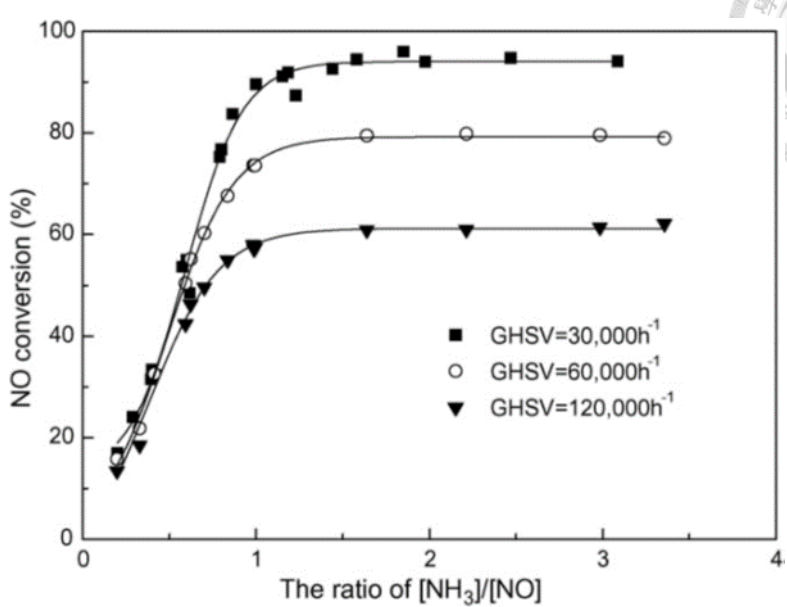


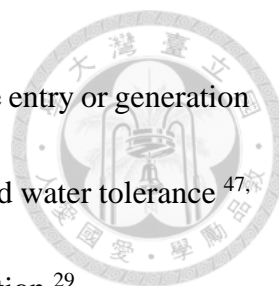
Figure 2-7. Relation between SCR activity and different NH<sub>3</sub> concentrations in different gas hour space velocity<sup>52</sup>.

### 2.4.3. Effect of H<sub>2</sub>O and SO<sub>2</sub>



Figure 2-8. Effect of the H<sub>2</sub>O and SO<sub>2</sub> poisoning effect during SCR<sup>53</sup>.

Water vapor may come from the reducing agents or fuel. Water vapor can compete with NH<sub>3</sub> for active acid sites and can lead to the inhibition of SCR activity. This inhibition



can be reversed by raising the reaction temperature or even halting the entry or generation of water vapor. Catalysts with hydrophobic support often exhibit good water tolerance<sup>47</sup>.<sup>54</sup>. Some research pointed out that water vapor can inhibit  $\text{NH}_3$  oxidation<sup>29</sup>.

$\text{SO}_2$  mainly comes from fuel like coal. As shown in Figure 2-8, the deactivation caused by  $\text{SO}_2$  can be divided into two parts: reversible deactivation and irreversible deactivation. For reversible deactivation,  $\text{SO}_2$  will often be oxidized to  $\text{SO}_3$  by  $\text{O}_2$  in the flue gas, and  $\text{NO}_2$  can oxidize  $\text{SO}_2$  to  $\text{SO}_3$ . Ammonium species will react with  $\text{SO}_3$  and generate ammonium sulfate species. The formation and deposition of ammonium sulfate species hinder the adsorption of adsorbed  $\text{NO}_x$  species<sup>55-56</sup>. The ammonium sulfate species can be removed by raising the operating temperature to induce decomposition or removed by washing it with water vapor and acid gas<sup>57</sup>. Guo, et al.<sup>58</sup> found that on the  $\text{Fe}_2\text{O}_3$ -SBA, as pore sizes of the catalyst increased, the decomposition temperature of ammonium sulfate species decreased due to the higher vapor pressure of ammonia and sulfur oxide species. Sulfation of metal oxide causes irreversible poisoning effects for SCR catalysts, as Jiang, et al.<sup>59</sup> mentioned that on the Fe-Mn/ $\text{TiO}_2$  catalyst,  $\text{SO}_2$  could adsorb onto the active sites. This also hindered the formation of the adsorbed  $\text{NO}_x$  species, and the new Bronsted acid sites could form simultaneously, promoting  $\text{NH}_3$  adsorption. Guo, et al.<sup>60</sup> and Peng, et al.<sup>61</sup> found an enhancement of SCR activity in the presence of  $\text{SO}_2$  on



$V_2O_5/TiO_2$  and  $CeO_2-WO_3/TiO_2-SiO_2$ , respectively, due to an increase in Bronsted acid sites.

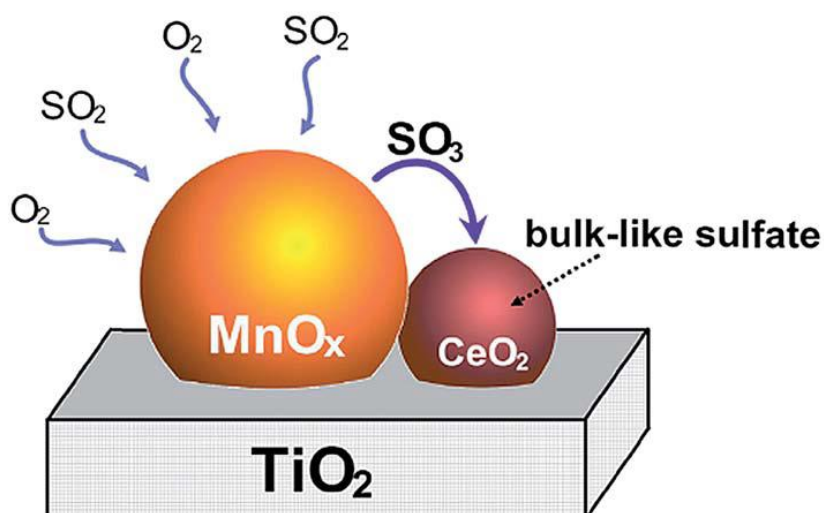


Figure 2-9. The proposed mechanism of  $SO_2$  deactivation effect on the SCR reaction. <sup>59</sup>

## 2.5. Mn-based catalysts for low-temperature $NO_x$ removal

Manganese based catalysts (Mn-based catalyst), including single crystal  $MnO_x$ , transition metal oxide modified catalyst, and  $MnO_x$  loaded on different supports, have attracted great attention due to the outstanding activity of both  $NH_3$ -SCR activity and  $NO$  oxidation. Different research has been published for the further promotion of  $NO_x$  removal activity and prevention of deactivation caused by  $SO_x$  and water vapor.



### 2.5.1. Metal modification

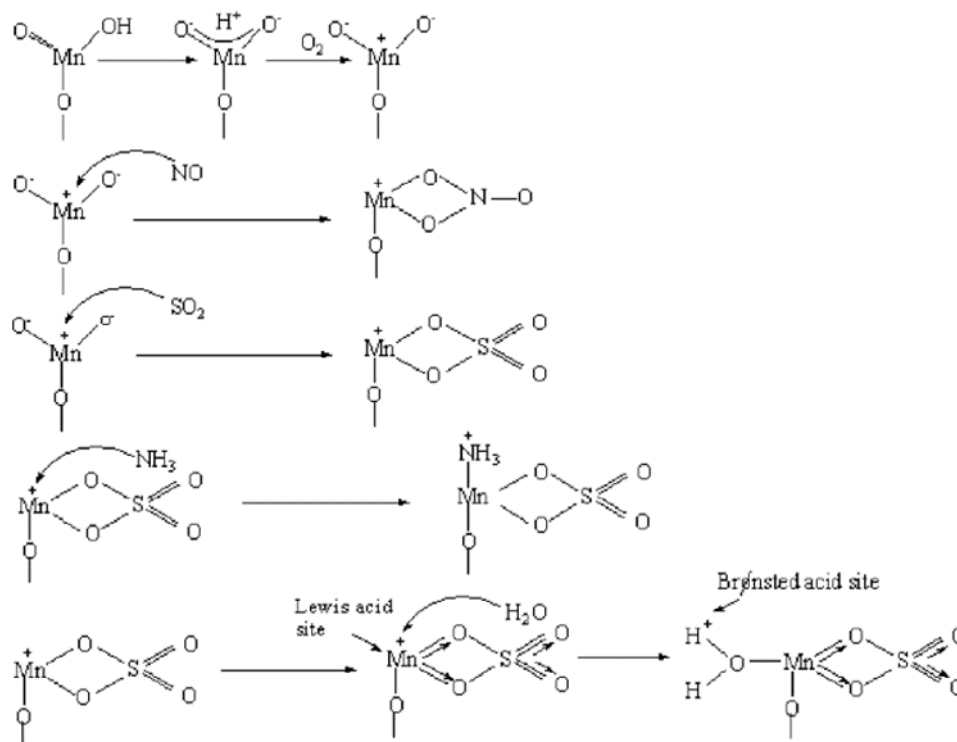
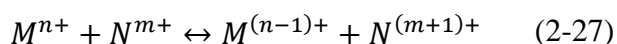


Figure 2-10. Scheme about the interaction between  $\text{SO}_2$  and  $\text{MnO}_2$  <sup>62</sup>.

Cerium (Ce) has also received considerable attention on the SCR catalyst because of its oxygen storage ability, redox cycle between  $\text{Ce}^{3+}$  and  $\text{Ce}^{4+}$ , and promotion for sulfur tolerance over transition metal oxide catalysts. The highly efficient electronic cycle property originates from the removal of neutral oxygen, leaving behind excess electrons in empty f orbitals of Ce, thereby leading to the efficiency of valence change <sup>63-64</sup>. By the formation of the redox cycle caused by  $\text{Ce}^{3+}$  and  $\text{Ce}^{4+}$  shown in Eq. 2-27, the recovery of

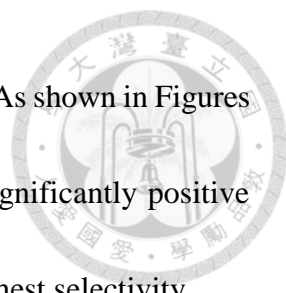


active metal species' valence states will be promoted.



Shen, et al.<sup>4</sup> found that Ce not only increased the concentration of surface adsorbed oxygen but also promoted the dispersion of MnO<sub>x</sub>, which caused an increase in active surface sites for SCR activity. Jin, et al.<sup>62</sup> indicated that Ce was more likely to react with SO<sub>x</sub> species and form less thermally stable species than manganese ammonium species on Mn-Ce/TiO<sub>2</sub> (Figure. 2-10). France, et al.<sup>48</sup> also found that Ce increased the concentration of surface adsorbed oxygen. Fan, et al.<sup>5</sup> found that on the MnO<sub>x</sub>/SAPO, Ce addition both on a support or mixed with active metal oxide precursor had a positive effect on the SCR activity and sulfur tolerance. No detectable XRD peaks of ammonium sulfate species on the catalyst modified with Ce meant that SO<sub>2</sub> tended to react with Ce rather than the adsorbed NH<sub>3</sub> species. This led to less formation of ammonium sulfate species and less blockage of the active sites on the catalyst. Chang, et al.<sup>65</sup> found that Ce could enhance HCl resistance and provide basic sites for adsorbed NO<sub>x</sub> species adsorption on CeO<sub>2</sub>-MoO<sub>3</sub>.

The effect of other metal doping has also been investigated. Thirupathi and Smirniotis



<sup>66</sup> investigated the doping effect of Cr, Fe, Co, Ni, Cu, Zn, Ce on Mn. As shown in Figures 2-11 and 2-12, the result indicated that Fe, Ni, Cu and Ce had a significantly positive effect on the SCR activity of Mn-TiO<sub>2</sub>, and Mn-Ni possessed the highest selectivity.

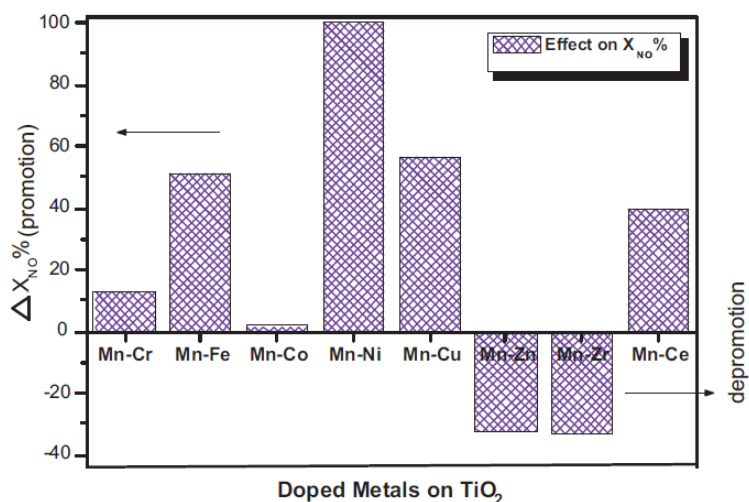


Figure 2-11. Promotion effect of co-doped metals on Mn/TiO<sub>2</sub> in the NH<sub>3</sub>-SCR at 200°C <sup>66</sup>

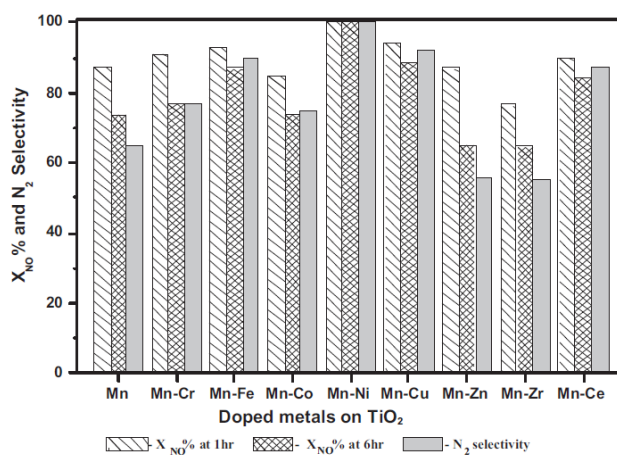


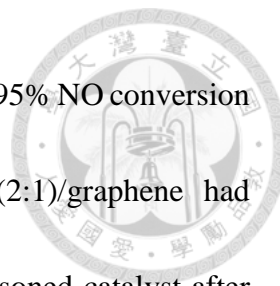
Figure 2-12. N<sub>2</sub> selectivity and catalytic performance of Mn-M/TiO<sub>2</sub> catalysts <sup>66</sup>.

### 2.5.2. Support modification

Catalysts with different support had also been studied. Yao, et al.<sup>67</sup> studied the MnO<sub>x</sub> supported on  $\gamma$ -Al<sub>2</sub>O<sub>3</sub>, TiO<sub>2</sub>, CeO<sub>2</sub> and SiO<sub>2</sub>. XRD results indicated that MnO<sub>x</sub> species could be dispersed well on  $\gamma$ -Al<sub>2</sub>O<sub>3</sub> due to the presence of different vacancy sites.

For carbon-based supports, Shu, et al.<sup>68</sup> investigated the NH<sub>3</sub>-SCR activity and physicochemical characters of Mn-Ce mixed oxides supported on commercial activated carbon (Mn-Ce-SAC) and rice husk based AC (Mn-Ce-RAC). The results of X-ray photoelectron spectroscopy (XPS) and DRIFT revealed that Mn-Ce-RAC had a higher ratio of Mn<sup>4+</sup>/Mn<sup>3+</sup> and more Bronsted acid sites. Besides this, Mn-Ce-RAC also had better sulfur tolerance. Tang, et al.<sup>57</sup> revealed that MnCoO<sub>4</sub>@RGO exhibited excellent NH<sub>3</sub>-SCR activity and N<sub>2</sub> selectivity at 140°C to 180°C. Moreover, SO<sub>2</sub> poisoned MnCoO<sub>4</sub>@RGO could be regenerated by water washing due to the 3-dimension morphology of MnCoO<sub>4</sub>@RGO. Lu, et al.<sup>54</sup> studied the SCR activity of MnO<sub>x</sub>-CeO<sub>x</sub>/TiO<sub>2</sub>-graphene. The result showed that 7 wt% metal oxide in addition with 0.8 wt% graphene oxide had the highest activity, with more than 95% NO conversion at 180°C. Xiao, et al.<sup>6</sup> found that 0.3 wt% graphene addition could enhance the NH<sub>3</sub>-SCR activity over MnO<sub>x</sub>-CeO<sub>x</sub>. You, et al.<sup>7</sup> investigated the NH<sub>3</sub>-SCR activity of MnO<sub>x</sub>-CeO<sub>x</sub>/graphene with different Mn/Ce molar ratios. The result showed that MnO<sub>x</sub>-

CeO<sub>x</sub>(8:1)/graphene had the best NH<sub>3</sub>-SCR activity, with more than a 95% NO conversion below 100°C. Both MnO<sub>x</sub>-CeO<sub>x</sub>(8:1)/graphene and MnO<sub>x</sub>-CeO<sub>x</sub>(2:1)/graphene had outstanding sulfur and water tolerance that could regenerate the poisoned catalyst after turning off sulfur and water for 100 min or so.



## Chapter 3. Materials and methods



### 3.1. Research framework

As shown in Figure 3-1, this research is divided into three parts, including the synthesis of Mn and Ce oxide supported graphene-based materials ( $\text{MnO}_x\text{-CeO}_x\text{-GO}$ ); (b) physicochemical characterization of  $\text{MnO}_x\text{-CeO}_x\text{-GO}$ ; (c) NO removal activity test for  $\text{MnO}_x\text{-CeO}_x\text{-GO}$ .

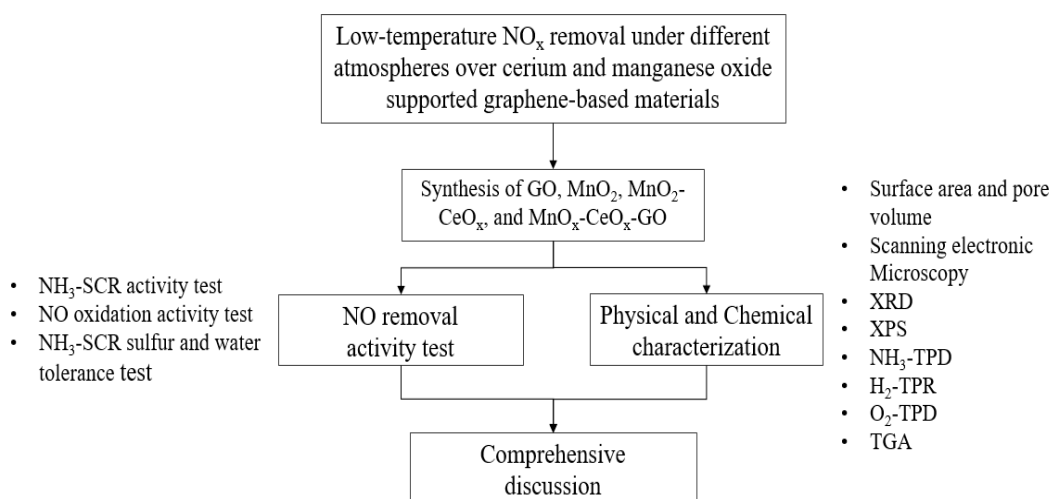
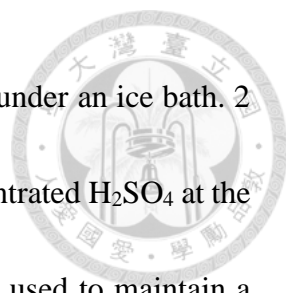


Figure 3-1. The flow chart of the research framework.

### 3.2. Preparation of graphene oxide and catalyst

#### 3.2.1. Synthesis of GO by Hummers' method

GO synthesis in this study is referred to Hummers and Offeman<sup>69</sup> and Achari, et al.<sup>70</sup>.

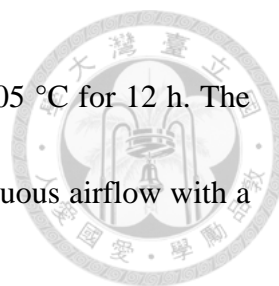


First, 46 mL of concentrated H<sub>2</sub>SO<sub>4</sub> was placed in a 250 mL beaker under an ice bath. 2 g graphite and 1 g NaNO<sub>3</sub> were mixed and slowly added to the concentrated H<sub>2</sub>SO<sub>4</sub> at the stirring speed of 250 rpm for 1 min in an ice bath. An ice bath was used to maintain a consistent low temperature and prevent the bump splash of reaction. Subsequently, 6 g of KMnO<sub>4</sub> was slowly added to the mixture at 250 rpm stirring speed in an ice bath until all the chemicals were dissolved and mixed uniformly. The stirring was kept at 250 rpm at 35°C for 3 h, after which 92 mL DI water was added and stirred at 250 rpm at 98°C for 30 min. Then 100 mL DI water and 10 mL H<sub>2</sub>O<sub>2</sub> were added and stirred for 1 min at 98°C. The GO precipitate was washed and centrifuged at 6000 rpm by 5% HCl one time and DI water five times subsequently. The final product was dried at 45°C in an oven for 3 days.

### **3.2.2. Ultrasonication impregnation of MnO<sub>x</sub>-CeO<sub>x</sub> graphene-based**

#### **composites**

Synthesis procedure of MnO<sub>x</sub>-CeO<sub>x</sub>-GO catalysts in this study took reference from Su, et al.<sup>71</sup> and You, et al.<sup>7</sup>. Mn(NO<sub>3</sub>)<sub>2</sub>·4H<sub>2</sub>O and Ce(NO<sub>3</sub>)<sub>3</sub>·6H<sub>2</sub>O acted as precursors of Mn and Ce. For 3 g catalyst to be synthesized, different weights of Mn(NO<sub>3</sub>)<sub>2</sub>·4H<sub>2</sub>O and Ce(NO<sub>3</sub>)<sub>3</sub>·6H<sub>2</sub>O were dissolved in 50 mL DI water in the Mn/Ce molar ratio of 8:1 and 4:1. Different amounts of the synthesized GO (0.1, 0.3, 1, 2, 4 wt% in catalysts) were dispersed in the metal nitrate solution by ultrasonication at 40°C for 1.5 h. After the



dispersion, the solution was poured into a glass plate and dried at 105 °C for 12 h. The black product was transferred to a quartz tube at 450°C under continuous airflow with a heating rate of 5°C/min.

To investigate the role of Ce, MnO<sub>x</sub>-GO was synthesized using the same method. For 3 g catalyst, different weights of Mn(NO<sub>3</sub>)<sub>2</sub>·4H<sub>2</sub>O were dissolved in 50 mL DI water, and a specific amount of GO was dispersed in the above solution by ultrasonication at 40°C for 1.5 h. The ultrasonicated mixture was poured on a glass plate and dried at 105°C for 12 h. The black product was transferred to a quartz tube at 450°C under continuous airflow with a heating rate of 5 °C/min.

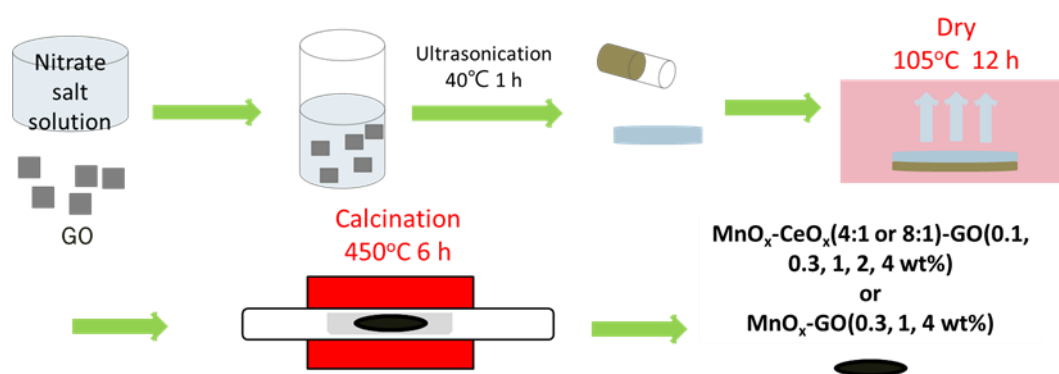


Figure 3-2. The steps of synthesis of MnO<sub>x</sub>-CeO<sub>x</sub>-GO catalysts and MnO<sub>x</sub>-GO catalysts.

### 3.2.3. Synthesis of MnO<sub>2</sub> and MnO<sub>2</sub>-CeO<sub>x</sub>

Synthesis procedure of MnO<sub>2</sub> in this study took reference from Chen, et al.<sup>72</sup>. 8.208 g

(NH<sub>4</sub>)<sub>2</sub>S<sub>2</sub>O<sub>8</sub> and 6.084 g MnSO<sub>4</sub>·H<sub>2</sub>O were dissolved in 144 mL of distilled water, and the mixed solution was stirred for 30 min to form a brown homogeneous solution. This was subsequently transferred to a stainless steel sealed autoclave (200 mL) at 90°C for 24 h. The resulting solution was filtered and washed three times with distilled water. The black precipitate was dried overnight at 80°C and then calcined under continuous airflow at 300°C for 2 h.

For synthesis of 3 g MnO<sub>2</sub>-CeO<sub>x</sub> catalyst, different weights of Ce(NO<sub>3</sub>)<sub>2</sub>·4H<sub>2</sub>O were dissolved in 50 mL DI water and ultrasonication was performed at 40°C for 1.5 h. The ultrasonicated mixture was poured on a glass plate and dried at 105°C for 12 h. The black product was transferred to a quartz tube at 450°C under continuous airflow with a heating rate of 5 °C/min.

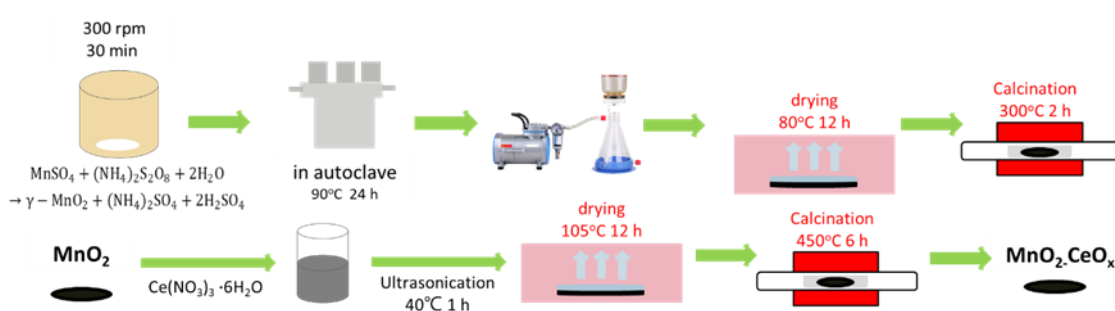


Figure 3-3. The steps of synthesis of MnO<sub>2</sub> and MnO<sub>2</sub>-CeO<sub>x</sub> catalysts.





### **3.3. Physicochemical characterization of catalyst**

#### **3.3.1. Surface area and pore volume**

The BET specific surface area ( $S_{\text{BET}}$ ), total pore volume ( $V_t$ ) of samples were determined by  $\text{N}_2$  adsorption at 77 K (Micromeritics ASAP-2420). Samples were dried at 105°C overnight to remove the humidity and degassed at 10–20 Torr vacuum and 200°C for 7 h before the  $\text{N}_2$  adsorption measurements.  $S_{\text{BET}}$  was calculated by the Brunauer-Emmett-Teller equation based on ASTM D4820-96a.

#### **3.3.2. Scanning electronic Microscopy**

Samples' surface morphology photographs were taken by Hitachi Tabletop TM-3000 Scanning Electron Microscope.

#### **3.3.3. X-ray diffraction measurement (XRD)**

The crystalline phase of catalysts was examined with X-ray diffraction measurement (XRD; Bruker D2 phase) with  $\text{Cu K}\alpha$  radiation (300 W, 20 kV,  $\lambda = 1.5405 \text{ \AA}$ , 30 mA max target current). Continuous scans were performed from  $2\theta = 5^\circ$  to  $80^\circ$  with a  $0.03^\circ$  step size and a counting time of 4 seconds/step. The crystalline phases were identified with JCPDS (Joint Committee on Powder Diffraction Standards) and information in the referenced literature.



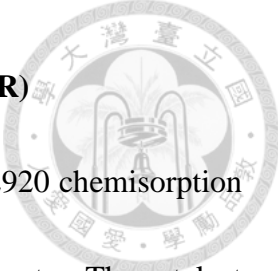
### **3.3.4. X-ray photoelectron spectroscopy (XPS)**

X-ray photoelectron spectroscopy (XPS; VG Scientific ESCALAB 250) was with Al K $\alpha$  irradiation (15 kV, 200 W) performed to understand the surface chemical compositions and valence states of the catalysts. For XPS analysis, all binding energies referred to the C1s peak at 285 eV.

### **3.3.5. NH<sub>3</sub>-Temperature Programmed Desorption (NH<sub>3</sub>-TPD)**

The NH<sub>3</sub>-TPD was performed using a Micromeritics II Autochem 2920 chemisorption analyzer with 0.2 g of powder sample loaded in a U-shaped quartz reactor. Samples were pretreated with 30 mL/min of helium flow at 300°C for 1 h with a heating temperature rate of 10°C/min. Subsequently, the sample was cooled down to 100°C and saturated with 10% NH<sub>3</sub>/He for 1 h under a flow of 30 mL/min. After saturation, the sample was purged by a 30 mL/min helium flow for 30 min at 100°C to remove excess gaseous NH<sub>3</sub>. Finally, the sample was heated up to 800°C with a heating rate of 10°C/min under a flow of 30 mL/min helium. NH<sub>3</sub> desorption of samples was detected by a thermal conductivity detector (TCD).

### 3.3.6. H<sub>2</sub>- Temperature Programmed Desorption (H<sub>2</sub>-TPR)



The H<sub>2</sub>-TPR was performed using a Micromeritics II Autochem 2920 chemisorption analyzer with 0.1 g of powder sample loaded in a U-shaped quartz reactor. The catalyst was purged in a flow of 30 mL/min Ar at 300°C with the heating rate of 10°C/min for 1 h and cooled to 100°C before measuring the H<sub>2</sub>-TPR. The catalyst was treated in 10% H<sub>2</sub>/Ar, and the hydrogen consumption was monitored by a thermal conductivity detector (TCD) in the Micromeritics II Autochem 2920 during an increase in temperature up to 800°C at a rate of 10°C/min.

### 3.3.7. O<sub>2</sub>- Temperature Programmed Desorption (O<sub>2</sub>-TPD)

The O<sub>2</sub>-TPD was performed using a Micromeritics II Autochem 2920 chemisorption analyzer with 0.2 g of powder sample loaded in a U-shaped quartz reactor. Samples were pretreated with 30 mL/min of He at 300°C for 1 h with 10°C/min heating temperature rate. Subsequently, the sample was cooled down to 50°C and saturated with 10% O<sub>2</sub>/He for 1 h in a flow of 30 mL/min. After saturation, the sample was purged by 30 mL/min helium flow for 30 min at 100°C to remove excess gaseous O<sub>2</sub>. Finally, the sample was heated up to 850°C with a heating rate of 10°C/min in a flow of 30 mL/min helium. O<sub>2</sub> desorption of the sample was detected by a thermal conductivity detector (TCD).



### 3.3.8. Thermogravimetric analysis (TGA)

TGA was performed by SHIMADU TGA-15. A sufficient amount of the sample would be filled into a Pt plate. Then samples were heated up to 900°C with a heating rate of 10°C/min under a flow of 50 mL N<sub>2</sub>. The weight loss was automatically recorded.

### 3.4. NO removal test

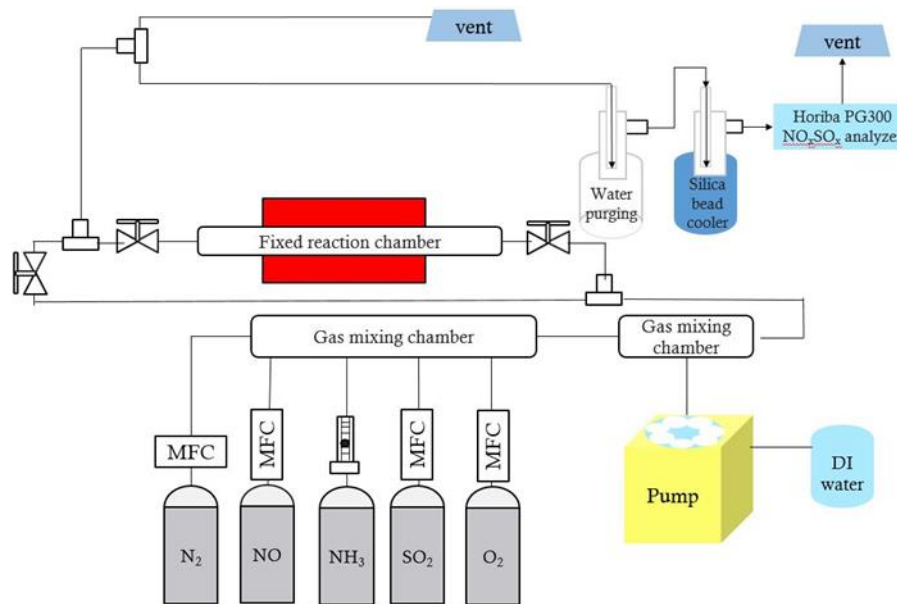
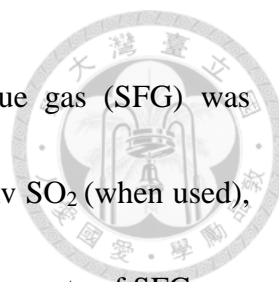


Figure 3-4. Experimental apparatus for fixed-bed NO<sub>x</sub> removal.

0.6 g catalyst sample was mixed and dispersed by the glass wool, and the whole catalyst/glass wool mixture was put into the middle of a quartz tube (1-in i.d.). The length



of the whole catalyst/glass was about 1.5 cm. The simulated flue gas (SFG) was comprised of 200 ppmv NO<sub>2</sub>, 200 ppmv NH<sub>3</sub> (when used), 200 ppmv SO<sub>2</sub> (when used), 6% O<sub>2</sub>, 10% H<sub>2</sub>O (when used), and N<sub>2</sub> as the balanced gas<sup>73</sup>. The flow rate of SFG was about 900 mL/min at 25°C. The concentration of NO and NO<sub>x</sub> was continuously monitored with a Horiba PG-350E portable gas analyzer. A water purging bottle and silica bead cooler were used in order to decrease corrosion and clogging on the inner unit of the analytical device caused by NH<sub>3</sub> and ammonium sulfate. Reaction temperature was maintained by the fixed reaction chamber. For every NO<sub>x</sub> removal experiment, the values of NO and NO<sub>x</sub> were recorded after removing the water purging bottle and silica bead cooler.

Table 3-1. Test parameter

Catalyst weight	Temperature	Gas flow	GHSV
0.6 g	60°C ~ 330°C	0.9 L/min	7100 h <sup>-1</sup>
Flue gas condition			
NO		200 ppm	
NH <sub>3</sub>		200 ppm (when used)	
O <sub>2</sub>		6%	
SO <sub>2</sub>		200 ppm (when used)	
H <sub>2</sub> O		10% (when used)	
N <sub>2</sub>		Balanced gas	



### 3.4.1. NH<sub>3</sub>-SCR and NO oxidation activity test

As in the above description, the real values of NO and NO<sub>x</sub> were recorded after removing the water purging bottle and silica bead cooler to prevent their consumption by water.  $C_{NO}^{bypass}$  is the NO concentration of SFG that bypassed the catalyst.  $C_{NO}^{out}$  is the NO concentration that SFG passes through the catalyst.  $C_{NO_x}^{out}$  is the NO<sub>x</sub> concentration passed through the catalyst. For the NH<sub>3</sub>-SCR activity test:

$$\text{NO conversion(\%)} = \frac{(C_{NO}^{bypass} - C_{NO}^{out})}{C_{NO}^{bypass}} \times 100\% \quad (3-1)$$

$$\text{NO}_2 \text{ formation(ppm)} = C_{NO_x}^{out} - C_{NO}^{out} \quad (3-2)$$

For NO oxidation activity test:

$$\text{NO conversion/oxidation(\%)} \quad (3-3)$$

$$= \frac{(C_{NO}^{bypass} - C_{NO}^{out})}{C_{NO}^{bypass}} \times 100\%$$

### 3.4.2. Sulfur and water tolerance over NH<sub>3</sub>-SCR

For the investigation of sulfur and water tolerance of the catalyst, the SCR activity test was continuously conducted for 1 h at 180°C. Subsequently, 200 ppm SO<sub>2</sub> and/or 10% H<sub>2</sub>O were added to flue gas for 1.5 h. After being exposed to poisoning, reactive species

for 1.5 h, the standard  $\text{NH}_3$ -SCR experiment was continued for 2 h to evaluate the reversibility of the poisoning effect on catalysts.



## Chapter 4. Results and Discussion



### 4.1. Physicochemical characterization of catalyst

#### 4.1.1. Surface area and pore volume

The specific BET surface area of catalysts is listed in Table 4-1. The specific surface area of  $\text{MnO}_x\text{-CeO}_x\text{-GO}$  catalysts was larger than all other kinds of catalysts. Moreover, the value of the specific surface area of  $\text{MnO}_x\text{-CeO}_x\text{-GO}$  and  $\text{MnO}_x\text{-GO}$  catalysts increased as the amount of GO increased, which indicated that the GO provided a more extensive interface<sup>7, 71</sup> for the impregnation of Mn and Ce ion, and prevented severe agglomeration during the calcination. A high specific surface area had generally been considered as a beneficial factor for most of the catalytic reaction.



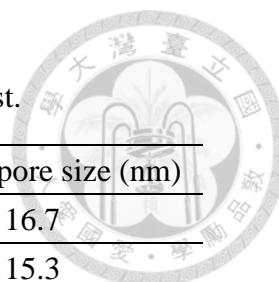


Table 4-1. Porous structure parameter of the catalyst.

Sample	S <sub>BET</sub> (m <sup>2</sup> /g)	V <sub>t</sub> (cm <sup>3</sup> /g)	Average pore size (nm)
MnO <sub>2</sub>	48.5	0.200	16.7
MnO <sub>2</sub> -CeO <sub>x</sub> (8:1)	41.4	0.166	15.3
MnO <sub>2</sub> -CeO <sub>x</sub> (4:1)	53.7	0.143	10.7
MnO <sub>x</sub> -GO(0.3 wt%)	4.96	0.022	13.3
MnO <sub>x</sub> -GO(1 wt%)	13.0	0.055	14.1
MnO <sub>x</sub> -GO(4 wt%)	32.7	0.122	14.3
MnO <sub>x</sub> -CeO <sub>x</sub> (8:1)-GO(0.3 wt%)	90.0	0.191	8.5
MnO <sub>x</sub> -CeO <sub>x</sub> (8:1)-GO(1 wt%)	105	0.212	8.1
MnO <sub>x</sub> -CeO <sub>x</sub> (8:1)-GO(4 wt%)	133	0.223	6.7
MnO <sub>x</sub> -CeO <sub>x</sub> (4:1)-GO(0.3 wt%)	73.8	0.166	8.5
MnO <sub>x</sub> -CeO <sub>x</sub> (4:1)-GO(1 wt%)	129	0.222	6.8
MnO <sub>x</sub> -CeO <sub>x</sub> (4:1)-GO(4 wt%)	150	0.222	5.9

#### 4.1.2. Scanning electronic Microscopy

Figures 4-1 to 4-4 show the SEM images of catalysts. Figures 4-1(a) and (b) show urchin-like clusters with diameters of about 30 to 40  $\mu\text{m}$ . The urchin-like structure was composed of rod-shaped structures, which could usually be observed from synthesized MnO<sub>2</sub><sup>74</sup>. The morphologies of MnO<sub>2</sub>-CeO<sub>x</sub> are shown in Figure 4-1(c) to Figure 4-1(f). With the increase of the Ce ratio, the urchin-like clusters became a globular structure with



small clusters dispersed on the surface gradually, which originated from the insertion of Ce on the  $\text{MnO}_2$  lattice structure.

Figures 4-2 to 4-3 show the SEM images of  $\text{MnO}_x\text{-CeO}_x\text{-GO}$  catalysts.  $\text{MnO}_x\text{-CeO}_x\text{-GO}$  showed more dispersive and smaller metal oxides than  $\text{MnO}_x\text{-GO}$  (Figure 4-4) and  $\text{MnO}_2\text{-CeO}_x$ . The SEM images of  $\text{MnO}_x\text{-CeO}_x(4:1 \text{ and } 8:1)\text{-GO}(0.3 \text{ wt}\%)$  show that there were large particles with small clusters and needle-like structures irregularly dispersed on their surface, which was caused by the higher specific surface area and flexible structure of GO. The needle-like structure was the crystal of  $\text{MnO}_2$ . With the increase of GO, the dispersive effect on the morphology became more significant, as the metal clusters increased with the decrease of the needle-like structure. For the  $\text{MnO}_x\text{-CeO}_x\text{-GO}(4 \text{ wt}\%)$  catalysts, large amounts of small clusters with a diameter of about 2-10  $\mu\text{m}$  adhered to a bigger particle or surface, which indicated that the metal oxide was fully dispersed on the surface of GO or the crystallization of metal oxide had been inserted by GO. For  $\text{MnO}_x\text{-GO}$  catalysts,  $\text{MnO}_x\text{-GO}(0.3 \text{ wt}\%)$  surprisingly showed an aggregate morphology (Figures 4-4(a) and (b)), which was consistent with its specific surface area.  $\text{MnO}_x\text{-GO}(4 \text{ wt}\%)$  showed that huge amounts of small metal oxide clusters adhered to large particles more densely than the other two  $\text{MnO}_x\text{-CeO}_x\text{-GO}(4 \text{ wt}\%)$  catalysts. Compared with the morphology of all catalysts and BET data, the high dispersion of the metal oxide of  $\text{MnO}_x\text{-$



CeO<sub>x</sub>-GO may have been resulted by Ce rather than GO. Nevertheless, the extent of contribution from GO in metal oxide dispersion could still be observed based on the BET data.

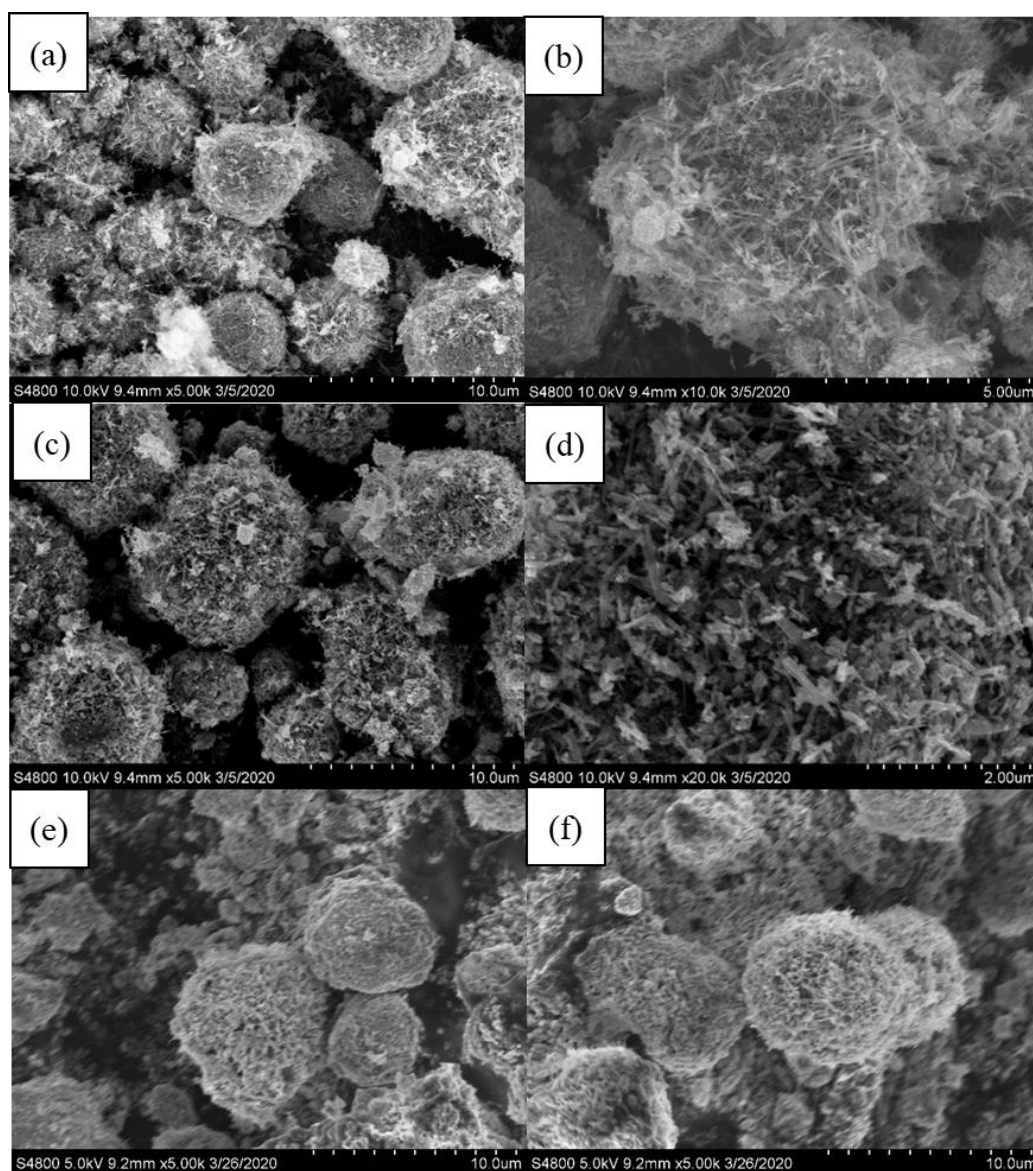


Figure 4-1. SEM images of MnO<sub>2</sub> (a, b), MnO<sub>2</sub>-CeO<sub>x</sub>(8:1) (c, d) and MnO<sub>2</sub>-CeO<sub>x</sub>(4:1) (e, f)

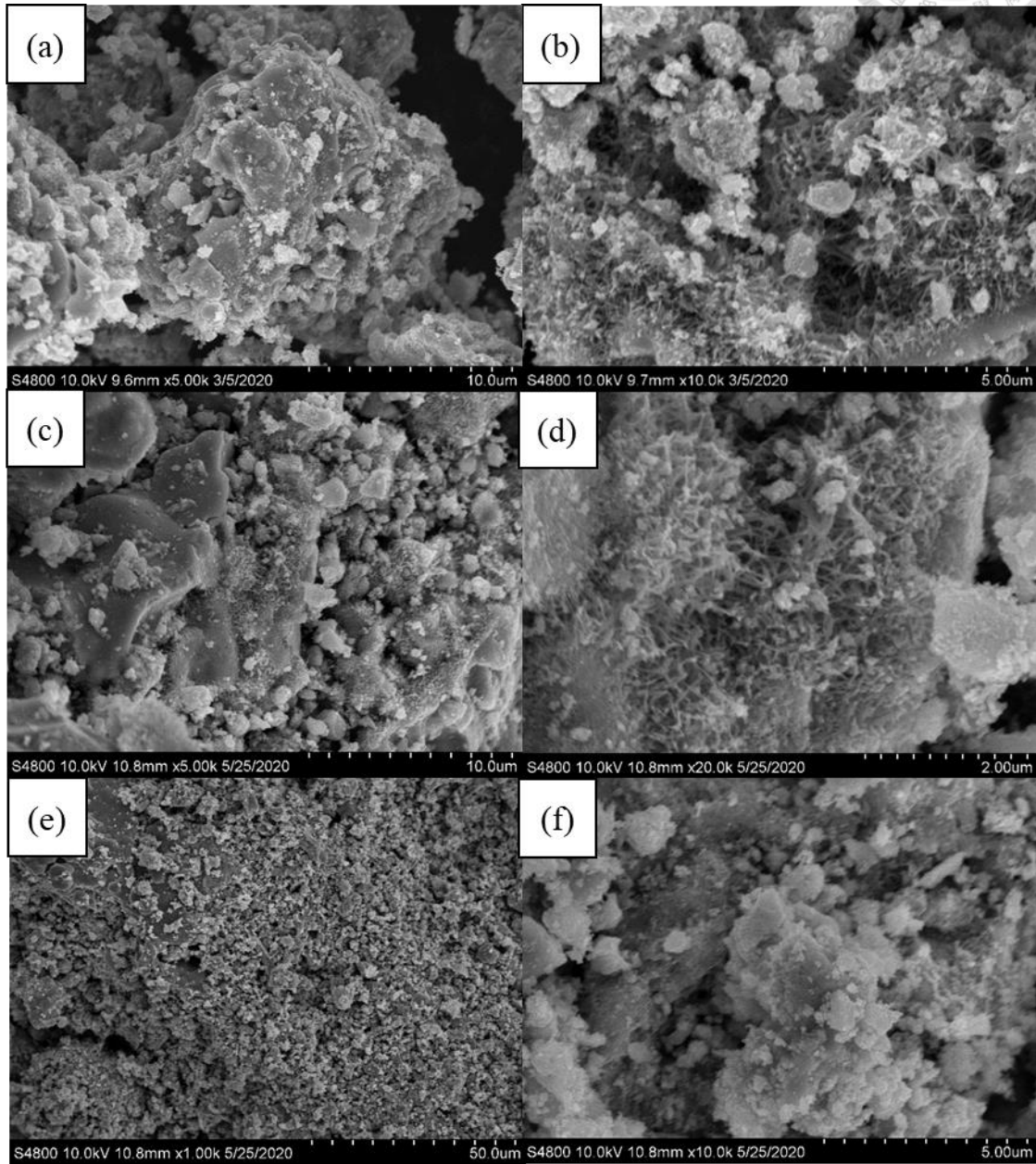


Figure 4-2. SEM images of  $\text{MnO}_2\text{-CeO}_x(8:1)\text{-GO}$  catalyst with 0.3 wt% GO (a, b), 2 wt% GO (c, d) and 4 wt% GO (e, f)

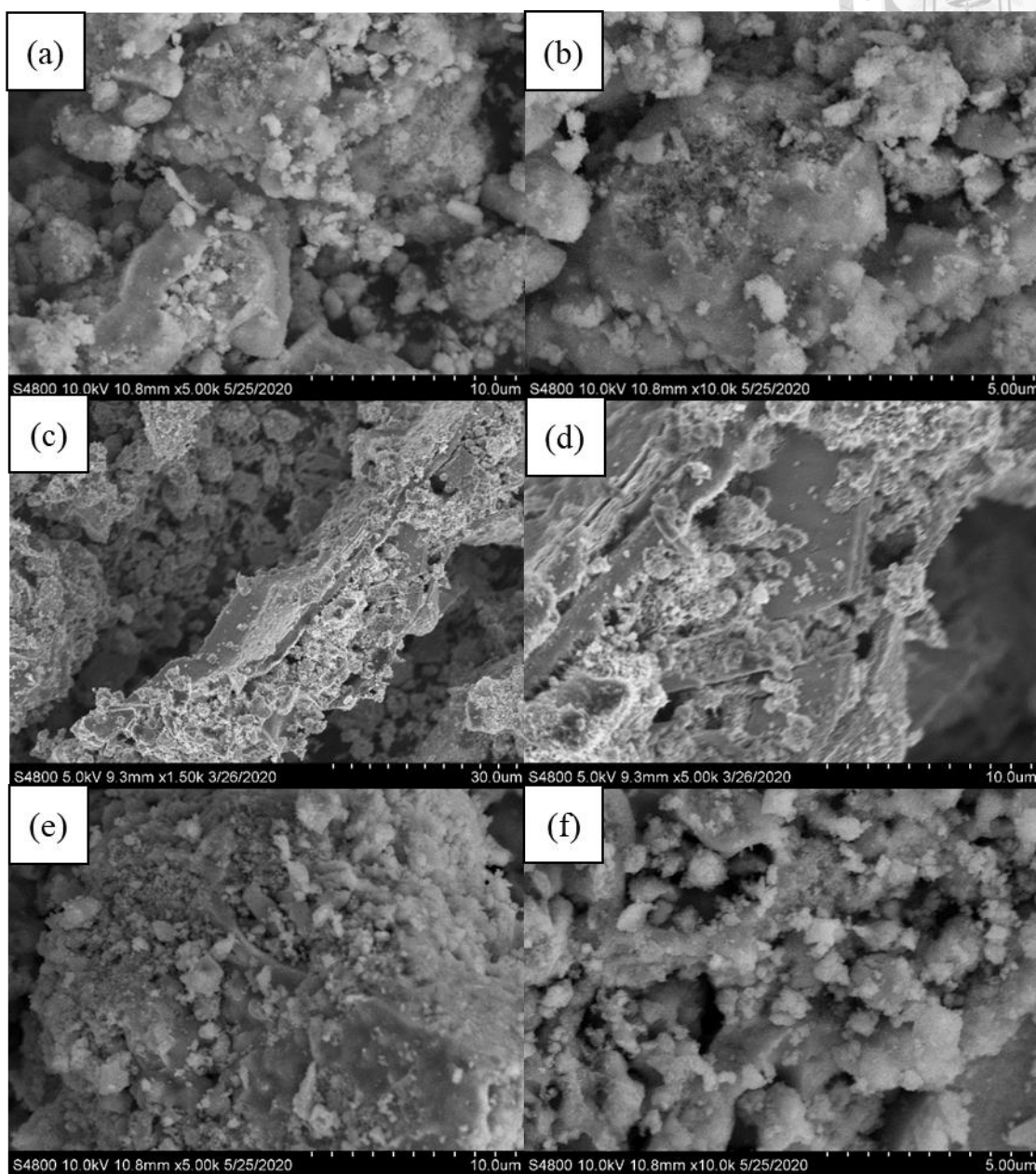


Figure 4-3. SEM images of  $\text{MnO}_2\text{-CeO}_x(4:1)\text{-GO}$  catalyst with 0.3 wt% GO (a, b), 2 wt% GO (c, d) and 4 wt% GO (e, f)

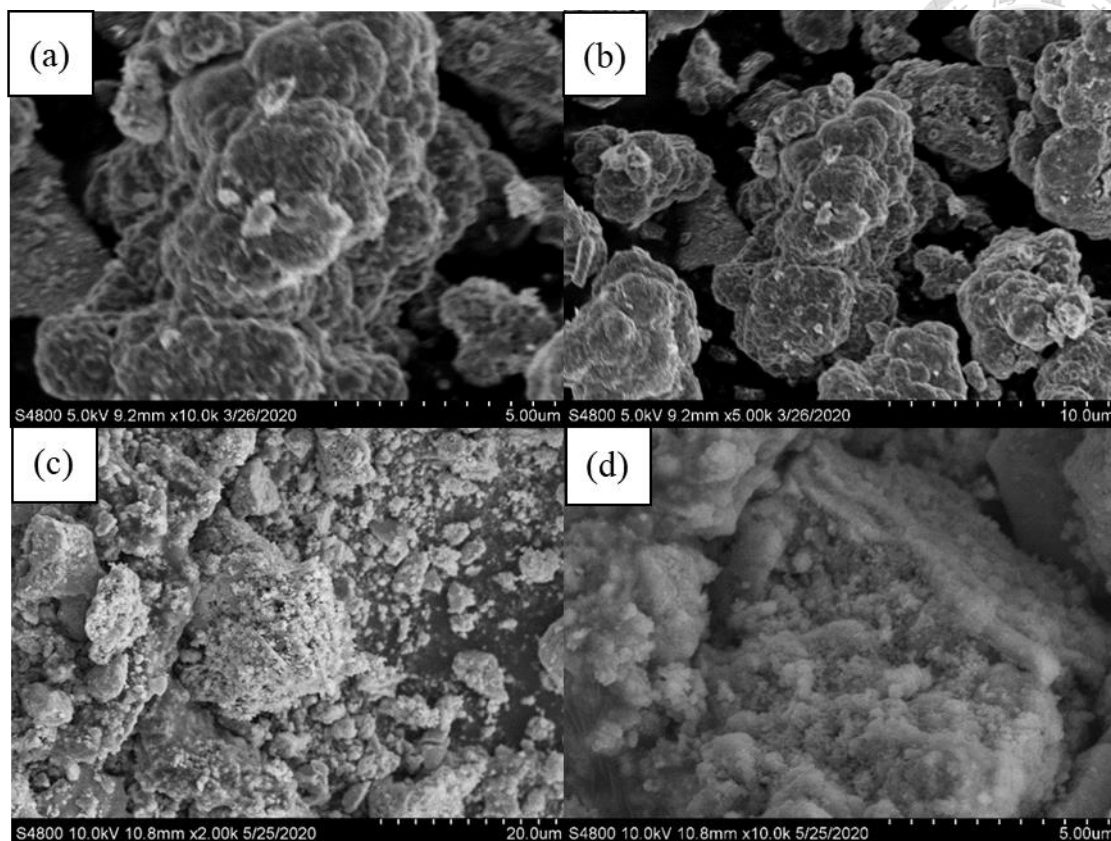
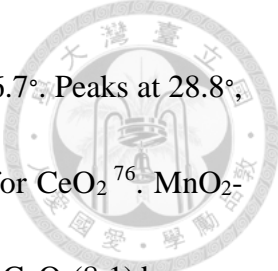


Figure 4-4. SEM images of MnO<sub>x</sub>- GO catalysts with 0.3 wt% (a, b) and 4 wt% (c, d)

#### 4.1.3. X-ray diffraction measurement (XRD)

Figure 4-5 shows the crystal lattice character of all catalysts. For self-synthesized MnO<sub>2</sub>, four distinct peaks at 37.3°, 42.7°, 56.6° and 65.4° could be assigned to  $\gamma$ -MnO<sub>2</sub> (JCPDS 14-0644) and corresponded to the (131), (300), (160), and (421) planes. MnO<sub>2</sub>-CeO<sub>x</sub>(8:1) showed diffraction peaks at 29.0°, 37.5°, 42.9°, 56.84°, and 65.1°<sup>74-75</sup>. The peaks at 37.5°, 42.9°, 56.6°, and 65.4° could be ascribed to  $\gamma$ -MnO<sub>2</sub>. MnO<sub>2</sub>-CeO<sub>x</sub>(4:1)



showed the diffraction peaks at 28.8°, 33.2°, 37.5°, 42.8°, 47.7° and 56.7°. Peaks at 28.8°, 33.2° and 47.7° could be ascribed to (111), (200), and (220) planes for  $\text{CeO}_2$ <sup>76</sup>.  $\text{MnO}_2$ - $\text{CeO}_x$  (4:1) possessed a much more apparent peak of  $\text{CeO}_2$  than  $\text{MnO}_2$ - $\text{CeO}_x$ (8:1) because of the higher ratio of Ce on  $\text{MnO}_2$ - $\text{CeO}_x$ (4:1). It could be noticed that the diffraction peaks of  $\text{MnO}_2$  on  $\text{MnO}_2$ - $\text{CeO}_x$ (4:1) was smaller than the peaks on  $\text{MnO}_2$ - $\text{CeO}_x$ (8:1), which indicates that additional Ce makes the formation of the solid solution of Mn and Ce more apparent.

Figure 4-5(a) shows the diffraction peak of  $\text{MnO}_x$ -GO catalysts. All the  $\text{MnO}_x$ -GO catalysts showed diffraction peaks at 37.3°, 42.7°, 56.6°, which could be attributed to  $\text{MnO}_2$ . These peaks became weaker as the amounts of GO increased due to the dispersion of Mn oxide on GO.  $\text{MnO}_x$ -GO catalysts also showed diffraction peaks at 23.1°, 28.8°, 33.0°, 38.3°, 49.4°, 55.3°, and 72.2°. Peaks at 23.1°, 33.0°, 38.3°, 49.4°, 55.3° could be attributed to (211), (222), (400), (431), and (440) planes of  $\text{Mn}_2\text{O}_3$  (JCPDS 41-1442). Peaks at 28.8° and 59.4° could be attributed to (112) and (224) planes of  $\text{Mn}_3\text{O}_4$  (JCPDS 24-0734). Between different  $\text{MnO}_x$ -GO catalysts, most of the intensity of the diffraction peaks gradually decreased as amounts of GO increased, which could be explained by the further dispersion and partially reduction of  $\text{MnO}_x$  on GO. From Figure 4-5 (b and c), it could be noticed that  $\text{MnO}_x$ - $\text{CeO}_x$ -GO catalysts exhibited low-intensity diffraction peaks,

which could be attributed to Ce and GO. Ce enhanced the dispersion of metal oxide and formed the solid solution with nearby metal oxide, and GO could act as the flexible surface for the distribution of metal oxide<sup>7, 71</sup>. Most of the crystal phase of MnO<sub>x</sub>-GO and MnO<sub>x</sub>-CeO<sub>x</sub>-GO catalysts showed the diversity of MnO<sub>x</sub>, which corresponded to the results of XPS that will be presented in the following section.





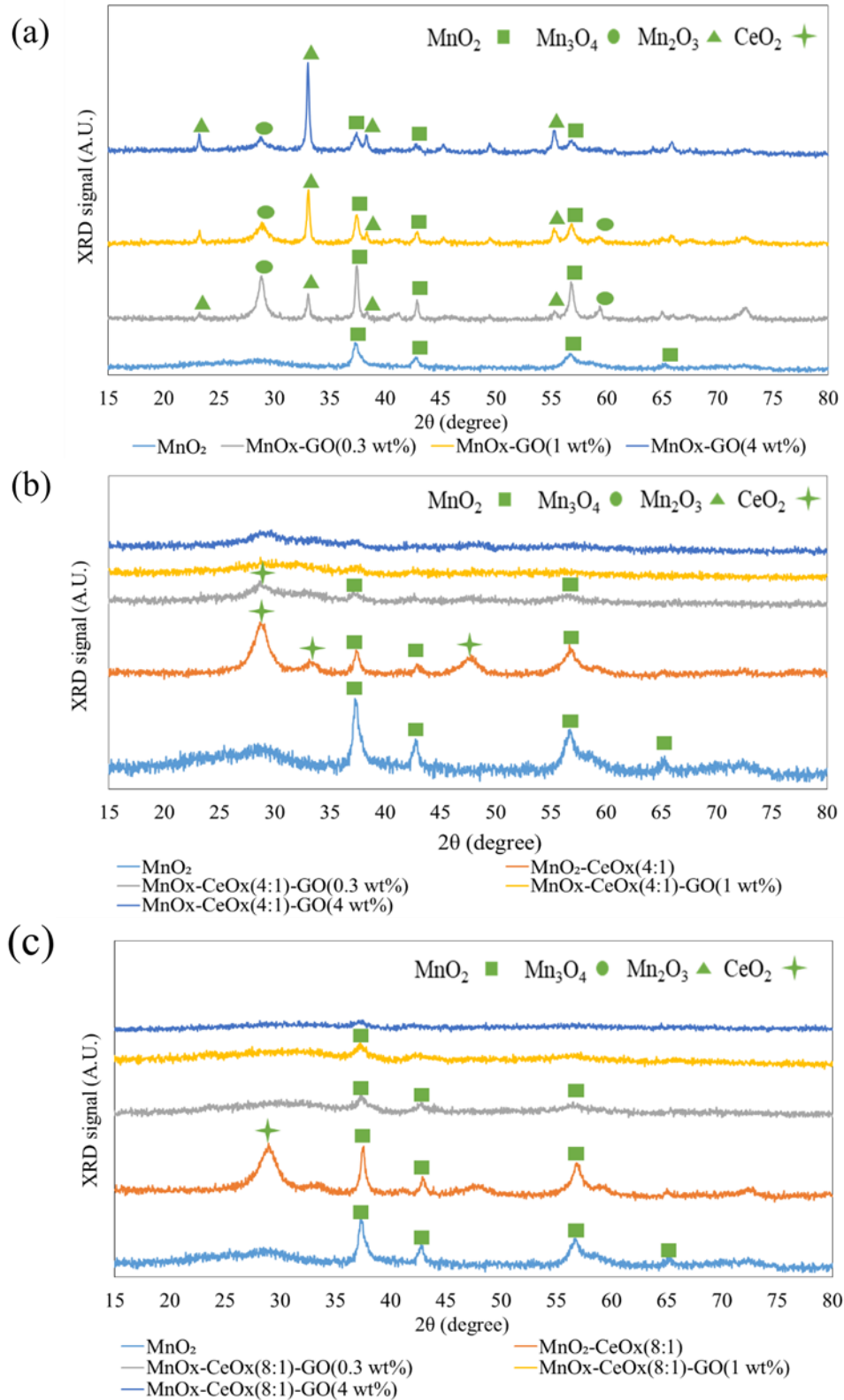
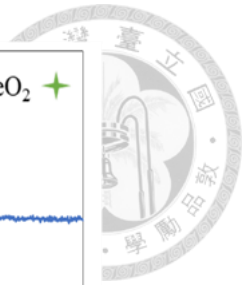


Figure 4-5. XRD pattern of (a) MnO<sub>x</sub>-GO, (b) MnO<sub>2</sub>-CeO<sub>x</sub>(4:1)-GO and (c) MnO<sub>x</sub>-CeO<sub>x</sub>(8:1)-GO catalysts with different amounts of GO addition.



#### 4.1.4. X-ray photoelectron spectroscopy (XPS)

Table 4-2 and Figures 4-6 to 4-9 show the surface composition of catalysts investigated by XPS. The Mn 2p spectra, which could be divided into three main characteristic peaks, were attributed to  $\text{Mn}^{2+}$  (639.9-641.4),  $\text{Mn}^{3+}$  (641.7-642.5), and  $\text{Mn}^{4+}$  (642.9-644)<sup>47,57,67,77</sup>. Compare with  $\text{MnO}_2$ , the Mn spectra  $\text{MnO}_2\text{-CeO}_x$  shifted lower and produced a multi-valence state (shown in Table 4-2 and Figure 4-6). However,  $\text{Mn}^{4+}$  was still the major oxidation state of Mn. For  $\text{MnO}_x\text{-CeO}_x\text{-GO}$  catalysts, Mn spectra often shift to more oxidation states with the increase of GO, and  $\text{Mn}^{4+}$  was also the major oxidation state, which is consistent with the finding of Su, et al.<sup>71</sup>.  $\text{MnO}_x\text{-CeO}_x(8:1)\text{-GO}$  catalysts possessed more multi-valence state than  $\text{MnO}_x\text{-CeO}_x(4:1)\text{-GO}$  catalysts, and  $\text{MnO}_x\text{-CeO}_x(4:1)\text{-GO}$  catalysts generally showed higher  $\text{Mn}^{4+}/\text{Mn}$  ratio than  $\text{MnO}_x\text{-CeO}_x(8:1)\text{-GO}$  catalysts. This shift on Mn valence distribution of  $\text{MnO}_x\text{-CeO}_x\text{-GO}$  catalysts may be caused by the synergistic effect from the oxygen supply from Ce and the morphology effect of GO. It is believed that a multi-valence state of active metals could promote the electronic cycle of catalytic reactions, and  $\text{Mn}^{4+}$  has also been believed to be the most active Mn species for  $\text{NH}_3\text{-SCR}$  and NO oxidation<sup>78-79</sup>.

The XPS curve of Ce 3d was deconvoluted to eight peaks: u, v, u', v', u'', v'', u''', v'''. The u', v' could be assigned to  $\text{Ce}^{3+}$ , and the others could be attributed to  $\text{Ce}^{4+}$ . From

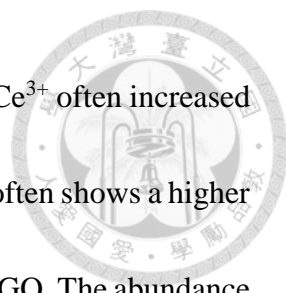
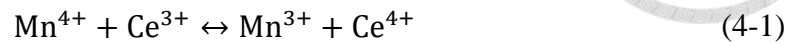


Table 4-2, it could be noticed that for the  $\text{MnO}_x\text{-CeO}_x\text{-GO}$  catalysts,  $\text{Ce}^{3+}$  often increased as the addition of GO increased. And  $\text{MnO}_x\text{-CeO}_x(8:1)\text{-GO}$  catalysts often shows a higher  $\text{Ce}^{3+}/\text{Ce}$  ratio for  $\text{MnO}_x\text{-CeO}_x\text{-GO}$  catalysts with the same amounts of GO. The abundance of  $\text{Ce}^{3+}$  is favorable to the formation of surface oxygen species and oxygen vacancy due to the charge imbalance, which could enhance the activation of surface adsorption species and the oxidation of  $\text{NO}$  to  $\text{NO}_2$ <sup>45-46, 76, 80</sup>. The ratio of chemisorbed oxygen species on  $\text{MnO}_x\text{-CeO}_x\text{-GO}$  catalysts slightly expanded as the  $\text{Ce}^{3+}$  increased.

The XPS spectra of O 1s generally could be divided into three parts: lattice oxygen species ( $\text{O}_\beta$ , 529.2-530.6 eV), chemisorbed oxygen species ( $\text{O}_\alpha$ , 531.2-532.4 eV), and adsorption of water and hydroxyl species ( $\text{O}_\gamma$ , 533.2-543.5 eV)<sup>75, 78</sup>. It is generally believed that  $\text{O}_\alpha$  was more reactive due to higher mobility. The result shows that  $\text{MnO}_2\text{-CeO}_x$  catalysts showed a higher  $\text{O}_\alpha$  peak, which indicates that the addition of Ce could enhance the generation of chemisorbed oxygen species. For  $\text{MnO}_x\text{-CeO}_x\text{-GO}$  catalysts, the increase of  $\text{O}_\alpha/\text{O}$  is not very obvious even the  $\text{Ce}^{3+}/\text{Ce}$  is risen may be caused by the adsorption of water and hydroxyl species. The signal of adsorbed water and hydroxyl species dropped the ratio of  $\text{O}_\alpha$ .

From the above results, it could be noticed that  $\text{MnO}_x\text{-CeO}_x\text{-GO}$  catalysts would exhibit more oxidative state on Mn and more reduced state on Ce, accompanied with the

increase of  $O_a/O$ , which showed that GO may promote the following dual redox cycle and shift to the left side:



By the more active  $\text{Mn}^{4+}$  species and the oxygen vacancy or reactive oxygen species accompanied with  $\text{Ce}^{3+}$ , the adsorption and activation NO could be promoted, thus the NO oxidation and  $\text{NH}_3$ -SCR could be promoted.

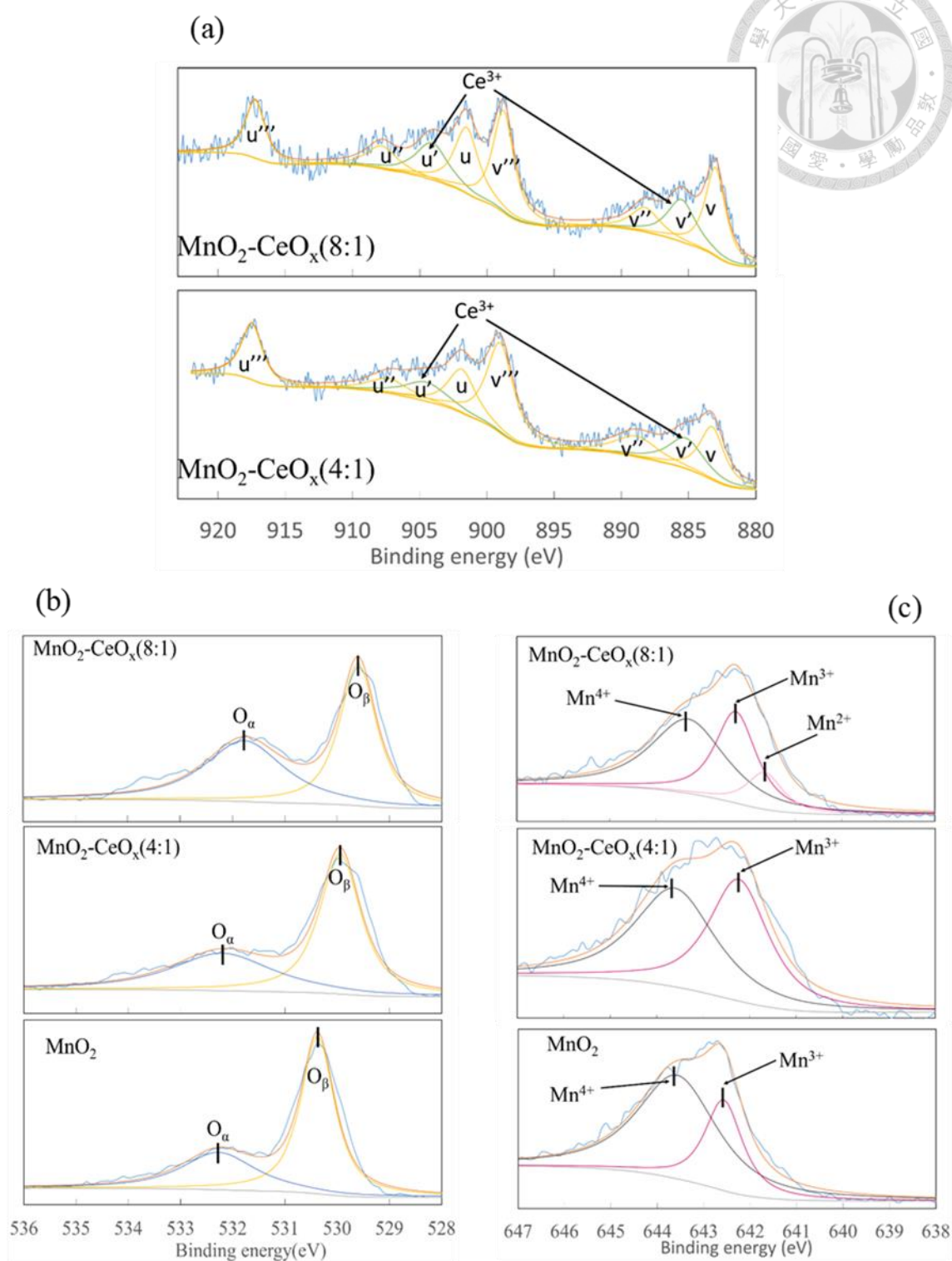


Figure 4-6. XPS spectra of Ce 3d (a), O 1s (b) and Mn 2p<sub>2/3</sub> (c) in MnO<sub>2</sub> and MnO<sub>2</sub>-CeO<sub>x</sub> catalysts.

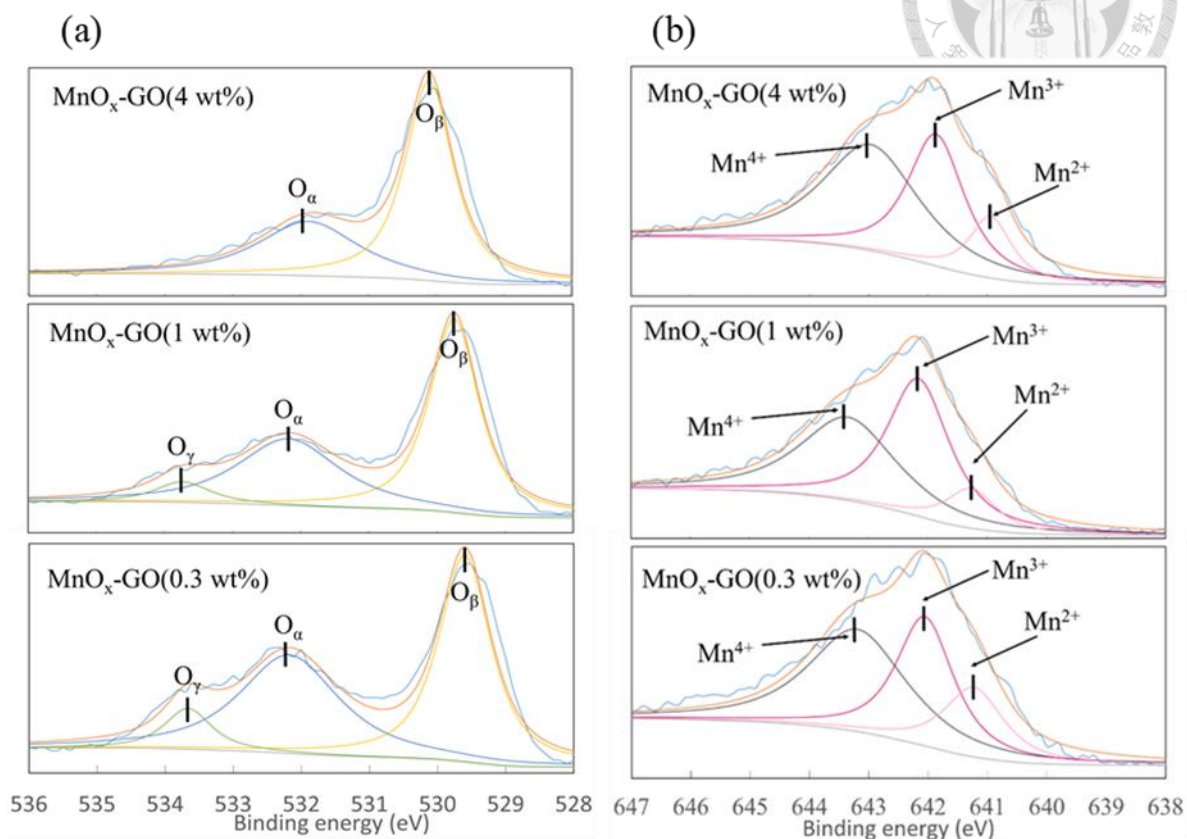


Figure 4-7. XPS spectra of O 1s (a) and Mn 2p<sub>2/3</sub> (b) in MnO<sub>x</sub>-GO catalyst

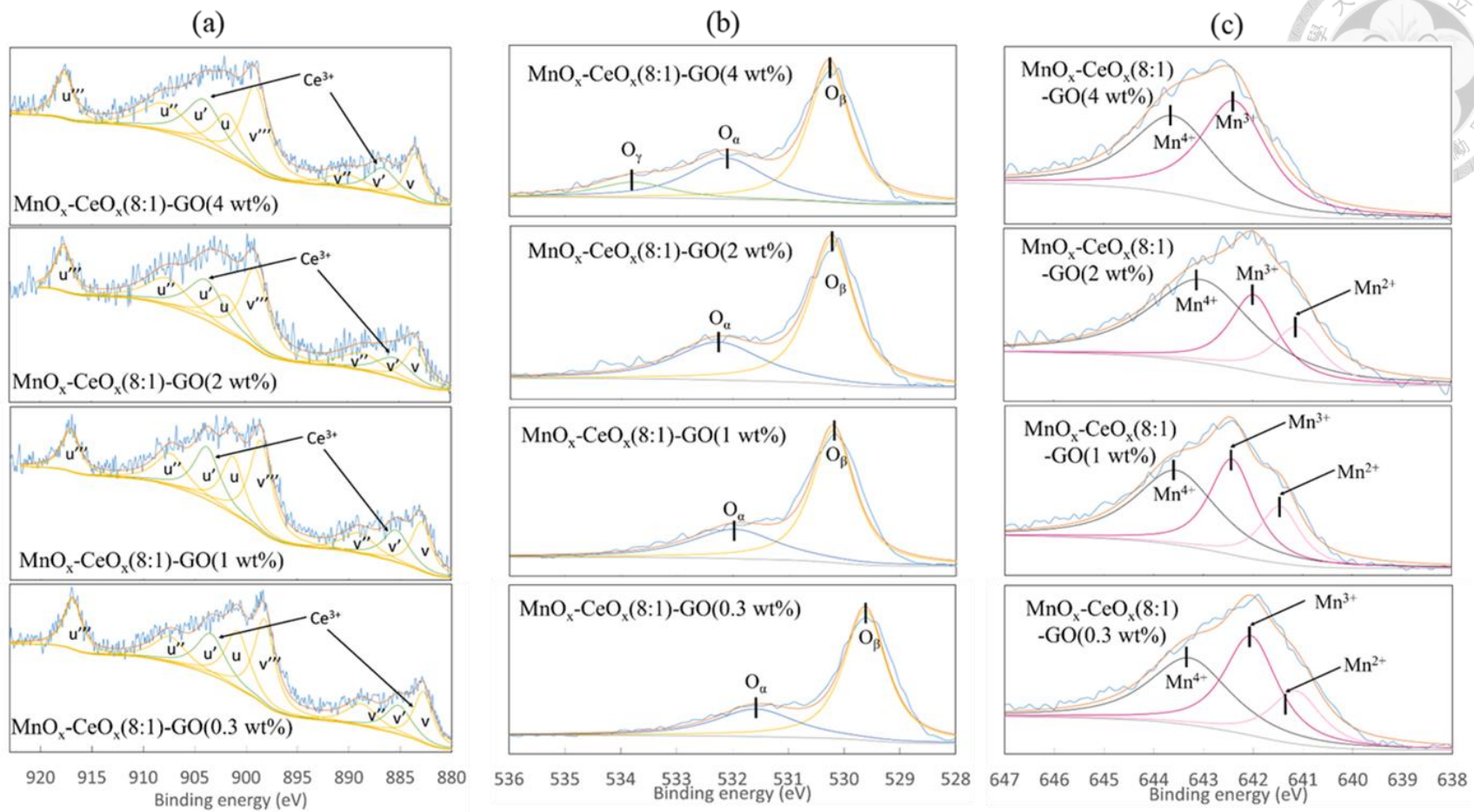


Figure 4-8. XPS spectra of Ce 3d (a), O 1s (b) and Mn 2p<sub>2/3</sub> (c) in MnO<sub>x</sub>-CeO<sub>x</sub>(8:1)-GO catalysts.

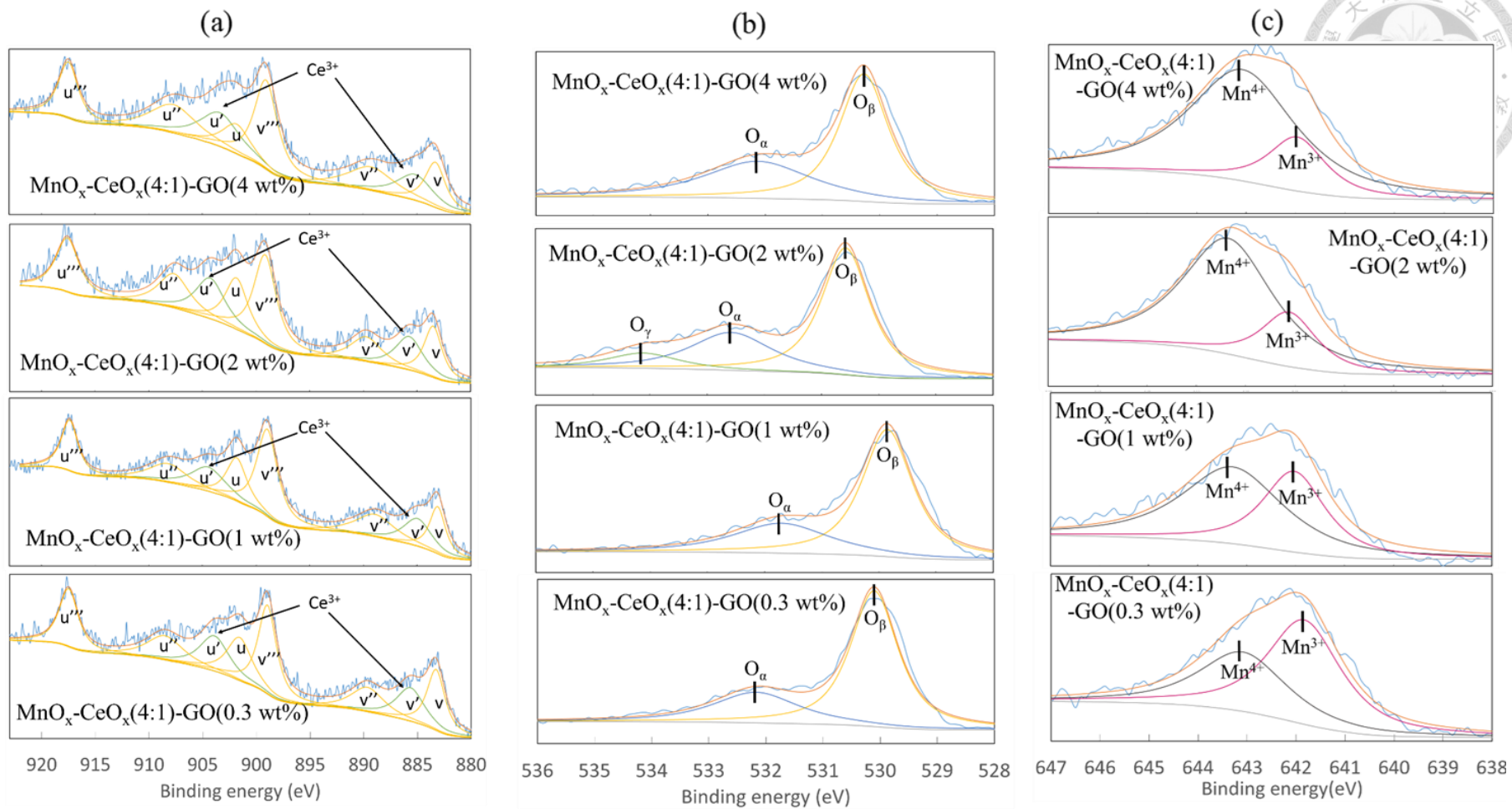


Figure 4-9. XPS spectra of Ce 3d (a), O 1s (b) and Mn 2p<sub>2/3</sub> (c) in MnO<sub>x</sub>-CeO<sub>x</sub>(4:1)-GO catalysts.



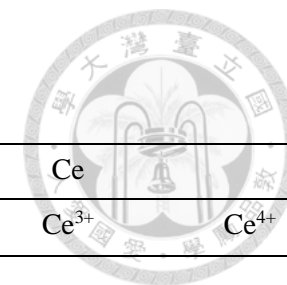
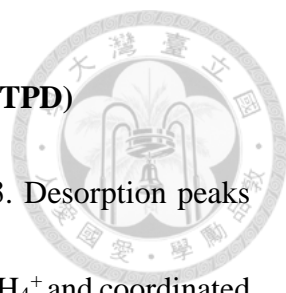


Table 4-2. Atomic surface compositions of catalysts obtained from XPS.

catalyst	Mn			O			Ce	
	Mn <sup>2+</sup>	Mn <sup>3+</sup>	Mn <sup>4+</sup>	O <sub>α</sub>	O <sub>β</sub> (lattice)	O <sub>γ</sub>	Ce <sup>3+</sup>	Ce <sup>4+</sup>
MnO <sub>2</sub>		0.29 (642.6)	0.71 (643.6)	0.34 (532.3)	0.66 (530.4)			
MnO <sub>2</sub> -CeO <sub>x</sub> (8:1)	0.12 (641.7)	0.34 (642.3)	0.54 (643.3)	0.48 (531.8)	0.52 (529.6)		0.23	0.77
MnO <sub>2</sub> -CeO <sub>x</sub> (4:1)		0.48 (642.2)	0.52 (643.7)	0.4 (532.2)	0.60 (529.9)		0.2	0.8
MnO <sub>x</sub> -GO(0.3 wt%)	0.2 (641.2)	0.34 (642.1)	0.46 (643.2)	0.43 (532.2)	0.48 (529.6)	0.09 (533.7)		
MnO <sub>x</sub> -GO(1wt%)	0.11 (641.3)	0.46 (642.2)	0.43 (643.3)	0.39 (532.2)	0.55 (529.7)	0.05 (533.7)		
MnO <sub>x</sub> -GO(4 wt%)	0.13 (640.9)	0.37 (641.9)	0.50 (643.0)	0.36 (531.9)	0.64 (530.1)			
MnO <sub>x</sub> -CeO <sub>x</sub> (8:1)-GO(0.1 wt%)	0.14 (641.5)	0.35 (642.3)	0.51 (643.5)	0.29 (532.2)	0.71 (530.2)		0.22	0.78
MnO <sub>x</sub> -CeO <sub>x</sub> (8:1)-GO(0.3 wt%)	0.2 (641.1)	0.39 (642.1)	0.41 (643.3)	0.29 (531.6)	0.71 (529.6)		0.23	0.77
MnO <sub>x</sub> -CeO <sub>x</sub> (8:1)-GO(1 wt%)	0.18 (641.3)	0.34 (642.4)	0.48 (643.5)	0.31 (532.0)	0.69 (530.2)		0.25	0.75

MnO <sub>x</sub> -CeO <sub>x</sub> (8:1)-GO(2 wt%)	0.17 (641.1)	0.25 (642.0)	0.58 (643.0)	0.34 (532.3)	0.66 (530.2)		0.25 0.75
MnO <sub>x</sub> -CeO <sub>x</sub> (8:1)-GO(4 wt%)		0.52 (642.4)	0.48 (643.6)	0.32 (532.1)	0.57 (530.3)	0.11 (533.8)	0.26 0.74
MnO <sub>x</sub> -CeO <sub>x</sub> (4:1)-GO(0.3 wt%)		0.6 (641.8)	0.4 (643.1)	0.29 (532.2)	0.71 (530.1)		0.20 0.8
MnO <sub>x</sub> -CeO <sub>x</sub> (4:1)-GO(1 wt%)		0.39 (642.0)	0.61 (643.3)	0.31 (531.7)	0.69 (529.9)		0.21 0.79
MnO <sub>x</sub> -CeO <sub>x</sub> (4:1)-GO(2 wt%)		0.22 (642.1)	0.78 (643.4)	0.31 (532.6)	0.59 (530.6)	0.10 (534.1)	0.22 0.78
MnO <sub>x</sub> -CeO <sub>x</sub> (4:1)-GO(4 wt%)		0.2 (642.0)	0.8 (643.1)	0.38 (532.1)	0.62 (530.3)		0.24 0.76

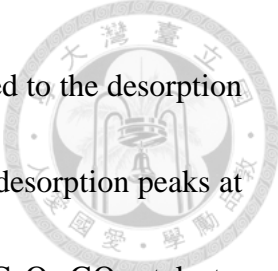
#### 4.1.5. NH<sub>3</sub>-Temperature Programmed Desorption (NH<sub>3</sub>-TPD)



The results of NH<sub>3</sub>-TPD are shown in Figure 4-10 and Table 4-3. Desorption peaks around 400°C to 600°C, and 600°C to 750°C were considered as the NH<sub>4</sub><sup>+</sup> and coordinated NH<sub>3</sub>, desorbed from Bronsted acid sites and Lewis acid sites of catalysts, respectively<sup>57, 81</sup>. The weak desorption peak around 100°C to 200°C corresponded to physical adsorption NH<sub>3</sub>. When desorption appeared at upwards of 700°C, they were considered as hydroxyl species<sup>67</sup>. The signal intensity of strong acid sites corresponded to SCR activity behavior at low temperatures<sup>7, 57</sup>.

As shown in Figure 4-10 (a), MnO<sub>2</sub> exhibited the sharp desorption peak at around 517.7°C, which could be ascribed to the NH<sub>4</sub><sup>+</sup> desorption from Bronsted acid site. With the CeO<sub>x</sub> loading, the desorption peaks became broader and shifted to higher temperatures. The desorption peaks of MnO<sub>2</sub>-CeO<sub>x</sub> implied that different kinds of active sites with different thermostability were formed due to the interaction between MnO<sub>2</sub> and CeO<sub>x</sub>. Some active sites may be similar to Lewis acid sites. The NH<sub>3</sub>-TPD profiles of MnO<sub>x</sub>-GO catalysts are shown in Figure 4-10 (b), MnO<sub>x</sub>-GO catalysts exhibited the NH<sub>4</sub><sup>+</sup> desorption from Bronsted acid sites at around 500°C. Both the desorption amounts and desorption temperatures would decrease with the GO loading.

As shown in Figure 4-10 (c) and Figure 4-10 (d), All the MnO<sub>x</sub>-CeO<sub>x</sub>-GO catalysts



showed obvious desorption peaks at around 600°C to 700°C, attributed to the desorption of coordinated NH<sub>3</sub> from the Lewis acid sites and Bronsted acid site desorption peaks at around 450°C to 550°C weaker than MnO<sub>2</sub>-CeO<sub>x</sub>. Among the MnO<sub>x</sub>-CeO<sub>x</sub>-GO catalysts, MnO<sub>x</sub>-CeO<sub>x</sub>(4:1)-GO catalysts often exhibited relatively higher ratio of Lewis acid sites desorption than MnO<sub>x</sub>-CeO<sub>x</sub>(8:1)-GO catalysts except for the catalyst with 4 wt% GO. Furthermore, the desorption temperatures of Lewis acid sites would slightly decrease with the increase of GO.

It could be noticed that the Ce loading often promote the formation of Lewis acid sites at MnO<sub>x</sub>-CeO<sub>x</sub>-GO and MnO<sub>2</sub>-CeO<sub>x</sub>, which is consistent with the finding of Ma, et al.<sup>82</sup> and Qi and Yang<sup>27</sup>. In construct, the amounts of Lewis acid sites over MnO<sub>2</sub>-CeO<sub>x</sub>(4:1) weren't greater than MnO<sub>2</sub>-CeO<sub>x</sub>(8:1), which may be attributed to the morphology difference between MnO<sub>2</sub>-CeO<sub>x</sub> catalysts and MnO<sub>x</sub>-CeO<sub>x</sub>-GO catalysts. GO loading could provide larger and flexible surface for metal oxide dispersion<sup>7, 71</sup> and further promote the interaction between metal oxide like charge transfer or structure defect formation<sup>83</sup>, which may cause the change of surface properties and promote the formation of Lewis acid site. In the case of MnO<sub>2</sub>-CeO<sub>x</sub>, CeO<sub>x</sub> was only directly impregnated on the surface of catalyst. So as compared with MnO<sub>x</sub>-CeO<sub>x</sub>-GO catalysts, the interaction was relatively restricted and CeO<sub>x</sub> loading could even formed the agglomeration and block



the active sites on  $\text{MnO}_x$ .

Desorption temperatures are consistent with the strength of acid sites for trapping the  $\text{NH}_3$ , the shift of desorption temperatures on  $\text{MnO}_x$ -GO catalysts with the loading of GO may come from the electron donor ability and charge transfer promotion effect of GO. The Bronsted acid site interaction is conducted by the H abstraction by unsaturated lone pair electrons of  $\text{NH}_3$ <sup>21</sup>, so it could be deduced that the stronger bond strength of X-H (X could be the elements that form chemical bonds or electronic interaction with H, like O in hydroxyl group), the weaker the Bronsted acid sites. XRD and XPS results showing that  $\text{MnO}_x$  was reduced with the GO loading implied that GO could act as the electron donor to Mn or other electron deficient atom, which makes the electron withdrawing power to functional groups like hydroxyl group weaker, and the electron density surrounds the hydroxyl group would attract the electron-deficient H tightly and inhibit the interaction between H and other species, causing the weaker Bronsted acid sites.

The phenomenon was not obvious in the case of  $\text{MnO}_x$ - $\text{CeO}_x$ -GO catalysts due to the contribution of  $\text{CeO}_x$ . As shown in XPS data, charge transfer and redox cycle of  $\text{MnO}_x$  and  $\text{CeO}_x$  shifted Mn to higher valance state, so the unsaturated  $\text{Mn}^{4+}$  would withdraw the electron from surrounding lattice composition or surface functional group and made the H was easier to be abstracted.

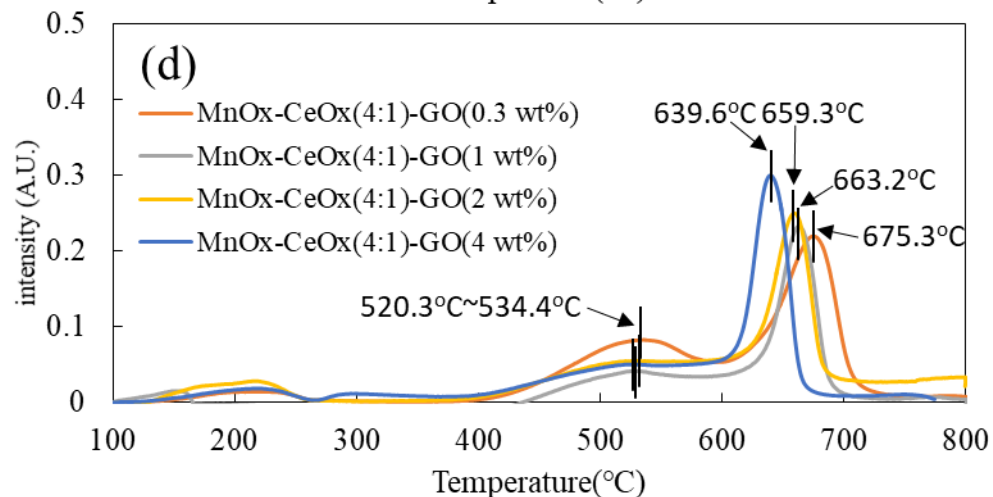
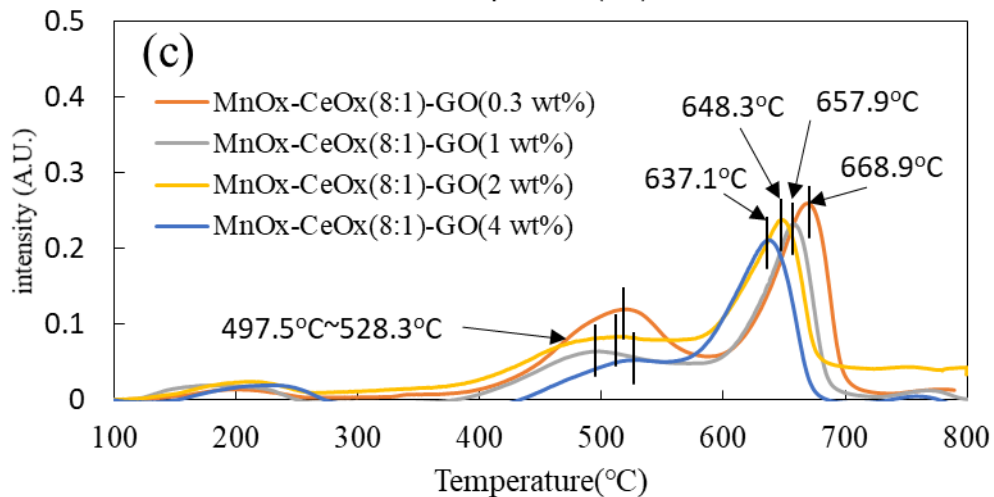
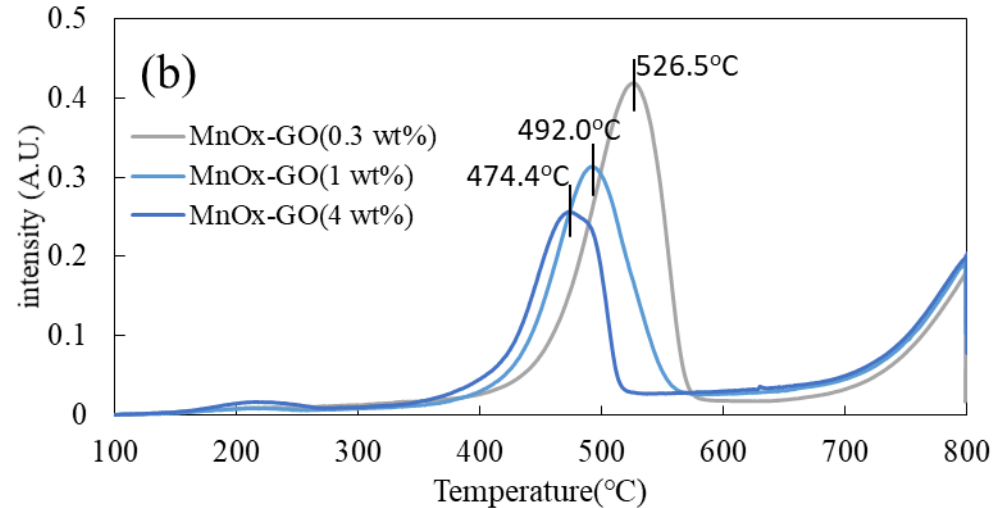
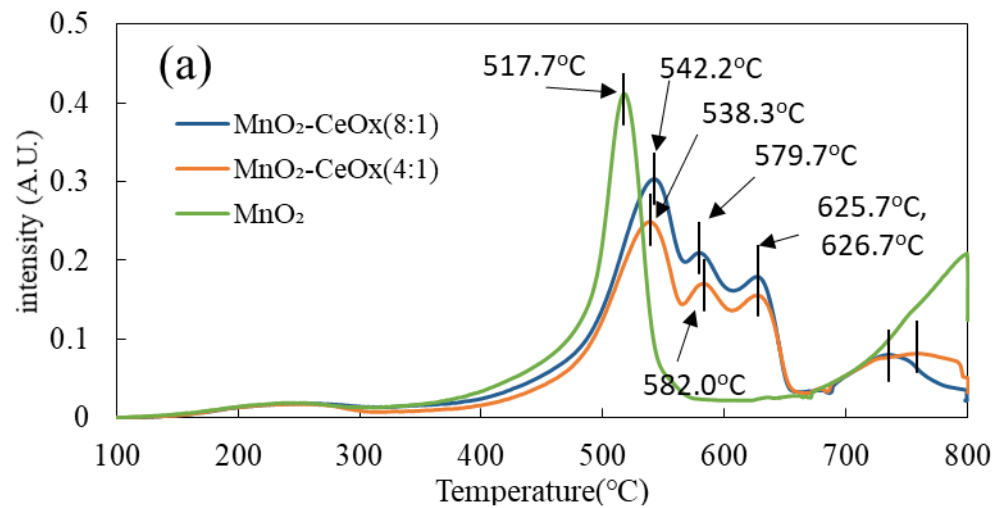


Figure 4-10. NH<sub>3</sub>-TPD profile over catalyst

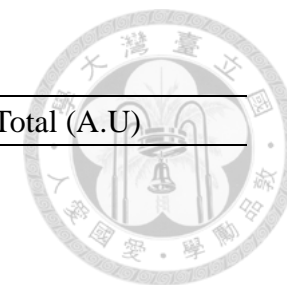
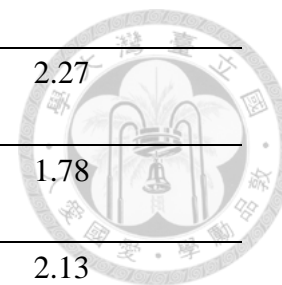


Table 4-3. Quantitative analysis of NH<sub>3</sub>-TPD over catalysts.

catalyst	Surface acid site (%)			Total (A.U)
	Physical adsorbed acid site	moderate acid sites	medium Strong and strong acid sites or hydroxyl group	
MnO <sub>2</sub>		100 (517.7 °C)		1.97
MnO <sub>2</sub> -CeO <sub>x</sub> (8:1)	2.6 (252.2 °C)	55.1 (542.2 °C) 18.1 (579.7 °C)	16.0 (626.7 °C) 8.2 (735.7 °C)	3.39
MnO <sub>2</sub> -CeO <sub>x</sub> (4:1)	4.2 (249.0 °C)	52.2 (538.3 °C) 18.4 (582.0 °C)	15.9 (625.7 °C) 9.3 (754.7 °C)	2.90
MnO <sub>x</sub> -GO(0.3 wt%)		100 (526.5 °C)		2.97
MnO <sub>x</sub> -GO(1 wt%)	1.3 (208.6 °C)	98.7 (492.0 °C)		2.25
MnO <sub>x</sub> -GO(4 wt%)	4.6 (216.1 °C)	95.4 (474.4 °C)		1.70
MnO <sub>x</sub> -CeO <sub>x</sub> (8:1)-GO(0.3 wt%)	3.2 (197.3 °C)	0.5 (382.1 °C) 44.0 (519.2 °C)	50.0 (668.9 °C) 2.3 (783.5 °C)	2.97
MnO <sub>x</sub> -CeO <sub>x</sub> (8:1)-GO(1 wt%)	7.9 (179.6 °C)	34.1 (497.5 °C)	53.8 (657.9 °C) 4.2 (767.5 °C)	2.55
MnO <sub>x</sub> -CeO <sub>x</sub> (8:1)-GO(2 wt%)	6.8 (209.0 °C)	36.2 (514.0 °C)	57.0 (648.3 °C)	2.20
MnO <sub>x</sub> -CeO <sub>x</sub> (8:1)-GO(4 wt%)	10.8 (235.5 °C)	25.1 (528.3 °C)	60.0 (637.1 °C) 4.1 (758.8 °C)	2.52
MnO <sub>x</sub> -CeO <sub>x</sub> (4:1)-GO(0.3 wt%)	4.3 (210.2 °C)	39.3 (534.4 °C)	56.3 (675.3 °C) 1.7 (786.9 °C)	2.37

MnO <sub>x</sub> -CeO <sub>x</sub> (4:1)-GO(1 wt%)	10.3 (153.0 °C)	29.6 (527.6 °C)	54.6 (663.2 °C)	2.27
	6.3 (164.3 °C)		4.2 (768.5 °C)	
MnO <sub>x</sub> -CeO <sub>x</sub> (4:1)-GO(2 wt%)	5.0 (187.8 °C)	28.6 (520.3 °C)	59.3 (659.3 °C)	1.78
	7.1 (216.4 °C)			
MnO <sub>x</sub> -CeO <sub>x</sub> (4:1)-GO(4 wt%)	6.8 (218.6 °C)	27.5 (529.1 °C)	58.3 (639.6 °C)	2.13
	4.0 (297.7 °C)		3.4 (750.6 °C)	





#### 4.1.6. H<sub>2</sub>-Temperature Programmed Desorption (H<sub>2</sub>-TPR)

The results of H<sub>2</sub>-TPR are shown in Figure 4-11 and Table 4-4. All the catalysts exhibited two main reduction peaks, which were often considered as hydrogen consumption due to a series of reduction of MnO<sub>x</sub>. From the result of XPS (Table 4-4), most of the Mn was Mn<sup>4+</sup> and Mn<sup>3+</sup>. The two reduction peaks showed the gradual reduction pathway of MnO<sub>2</sub> to Mn<sub>3</sub>O<sub>4</sub> and Mn<sub>3</sub>O<sub>4</sub> to Mn<sub>2</sub>O<sub>3</sub><sup>74-75</sup>.

Figure 4-11 (a) shows the profile of MnO<sub>2</sub>-CeO<sub>x</sub>, it could noticed that the Ce loading could slightly shift signal to lower temperature, especially at the second reduction peaks. For MnO<sub>x</sub>-GO catalysts (Figure 4-10 (b)), both the two reduction peaks were obviously shifted to lower temperature. Among all the MnO<sub>x</sub>-GO catalysts, MnO<sub>x</sub>-GO(1 wt%) exhibited the lowest temperature of two reduction peaks. GO loading also decreased the H<sub>2</sub> consumption of MnO<sub>x</sub>-GO catalysts. Figure 4-10 (c) and (d) displayed the H<sub>2</sub>-TPR profile of MnO<sub>x</sub>-CeO<sub>x</sub>-GO, which showed the lowest reduction temperature among all kinds of catalysts.

From the reduction temperature of all catalysts, we found that the more Ce or GO was added, the lower the reduction temperature of the catalyst, which implied the electron transfer was more efficient and promote the redox behavior. CeO<sub>x</sub> could perform redox cycle with MnO<sub>x</sub> and increase the charge transfer mobility and reduction activity. For the

case of  $\text{MnO}_x$ -GO catalysts, GO loading had partially reduced the  $\text{MnO}_x$ . So the multi-valence composition could enhance the charge transfer mobility and reduction activity.

The two distinctive reduction peaks of  $\text{MnO}_x$ - $\text{CeO}_x$ -GO showed the lowest reduction temperature among all kinds of catalysts. This phenomenon stemmed from the highly efficient electronic cycle between Mn and Ce and the promotive effect of electronic interaction from the  $\pi$ - $\pi$  interaction of GO<sup>7, 84</sup>. This promoted the oxygen mobility and reduction behavior of the catalysts and made the reduction cycle more efficient. None of the catalysts exhibited the reduction of  $\text{CeO}_x$

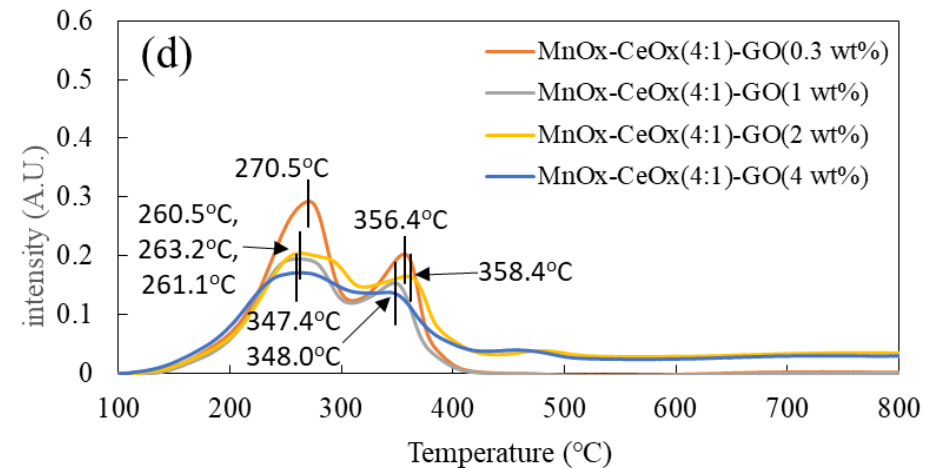
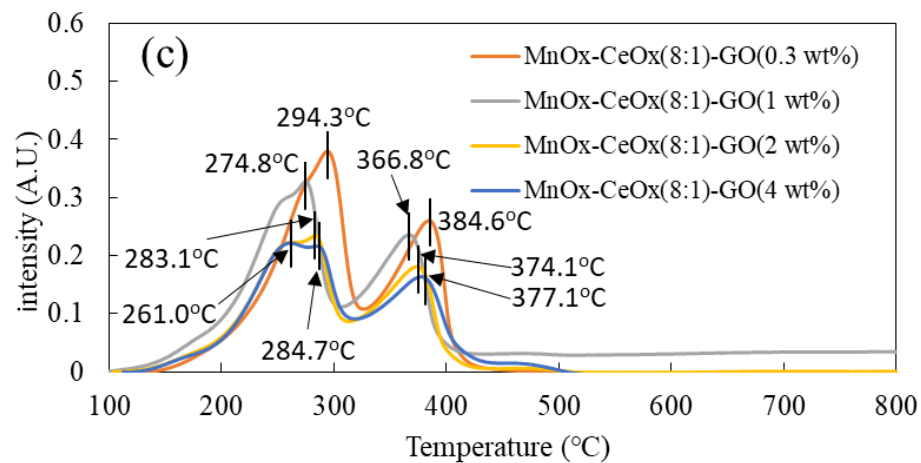
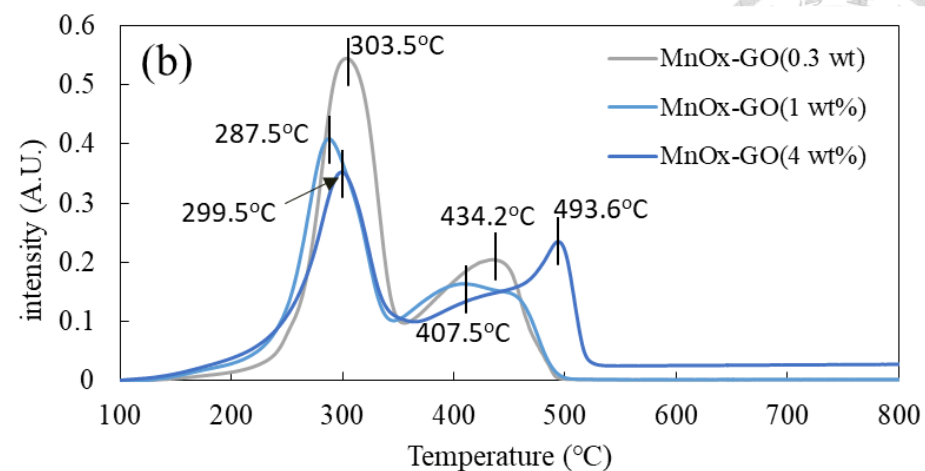
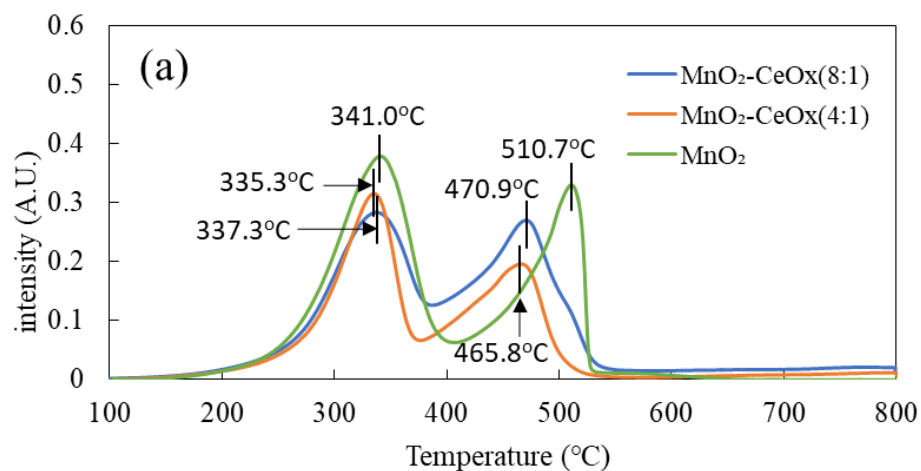


Figure 4-11. H<sub>2</sub>-TPR profile over catalysts.

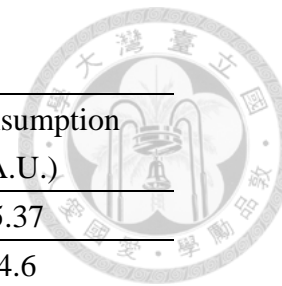
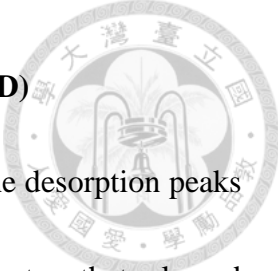


Table 4-4. Quantitative analysis of H<sub>2</sub>-TPR over catalysts.

catalyst	T <sub>I</sub> (%)	T <sub>II</sub> (%)	H <sub>2</sub> consumption (A.U.)
MnO <sub>2</sub>	61.3 (341.0 °C)	38.7 (510.7 °C)	5.37
MnO <sub>2</sub> -CeO <sub>x</sub> (8:1)	51.3 (337.3 °C)	48.7 (470.9 °C)	4.6
MnO <sub>2</sub> -CeO <sub>x</sub> (4:1)	57.9 (335.3 °C)	42.1 (465.8 °C)	3.64
MnO <sub>x</sub> -GO(0.3 wt%)	64.5 (303.5 °C)	35.5 (434.2 °C)	5.31
MnO <sub>x</sub> -GO(1 wt%)	60.9 (287.5 °C)	39.1 (407.5 °C)	4.71
MnO <sub>x</sub> -GO(4 wt%)	56.8 (299.5 °C)	43.2 (493.6 °C)	4.58
MnO <sub>x</sub> -CeO <sub>x</sub> (8:1)-GO(0.3 wt%)	64.6 (294.3 °C)	35.4 (384.6 °C)	4.23
MnO <sub>x</sub> -CeO <sub>x</sub> (8:1)-GO(1 wt%)	65.4 (274.8 °C)	34.6 (366.8 °C)	3.60
MnO <sub>x</sub> -CeO <sub>x</sub> (8:1)-GO(2 wt%)	63.0 (283.1 °C)	37.0 (374.1 °C)	3.18
MnO <sub>x</sub> -CeO <sub>x</sub> (8:1)-GO(4 wt%)	42.0 (261.0 °C)	36.8 (377.1 °C)	3.33
	18.5 (284.7 °C)	2.7 (455.3 °C)	
MnO <sub>x</sub> -CeO <sub>x</sub> (4:1)-GO(0.3 wt%)	66.8 (270.5 °C)	33.2(356.4 °C)	3.38
MnO <sub>x</sub> -CeO <sub>x</sub> (4:1)-GO(1 wt%)	66.9 (260.5 °C)	33.1 (347.4 °C)	2.66
MnO <sub>x</sub> -CeO <sub>x</sub> (4:1)-GO(2 wt%)	62.8 (263.2 °C)	33.4 (358.2 °C)	3.13
		3.9 (474.9 °C)	
MnO <sub>x</sub> -CeO <sub>x</sub> (4:1)-GO(4 wt%)	58.1 (261.1 °C)	25.3 (318.0 °C)	2.73
		16.6 (452.9 °C)	


#### 4.1.7. O<sub>2</sub>- Temperature Programmed Desorption (O<sub>2</sub>-TPD)



The results of O<sub>2</sub>-TPD are shown in Figure 4-12 and Table 4-5. The desorption peaks of O<sub>2</sub>-TPD showed the activity of different kinds of oxygen supply centers that released oxygen from different sources. Peaks from low temperatures could be divided into three parts: surface-physically adsorbed oxygen and surface superoxide ions (below 350°C), oxygen species on oxygen vacancies and chemisorbed oxygen like O<sub>2</sub><sup>2-</sup>/O<sup>-</sup> (300°C-550°C), and lattice oxygen (exceed 750°C)<sup>75, 85-86</sup>. Lattice oxygen species had also been classified as near surface lattice oxygen species (at around 600°C to 700°C) and bulk lattice oxygen species (exceed 750°C)<sup>87</sup>.

From Figure 4-12 (a) and (b), MnO<sub>2</sub>-CeO<sub>x</sub> and MnO<sub>x</sub>-GO catalysts showed desorption signal of O<sub>2</sub><sup>2-</sup>/O<sup>-</sup> at around 500°C and the desorption of bulk lattice oxygen at around 800°C to 850°C. The amount of O<sub>2</sub><sup>2-</sup>/O<sup>-</sup> and desorption temperature decreased as the amount of GO increased; on the contrary, the desorption of lattice oxygen increased as the amount of GO increased, which were consistent with the O 1s XPS peak of MnO<sub>x</sub>-GO catalysts, showing that GO increased the ratio of lattice oxygen.

From figure 4-12 (a), MnO<sub>2</sub>-CeO<sub>x</sub> catalysts displayed a broader, multi-peak oxygen desorption at around 500°C to 650°C, and a smaller lattice oxygen desorption at around 750°C to 850°C. As shown in Figure 4-12 (c) and (d), all MnO<sub>x</sub>-CeO<sub>x</sub>-GO catalysts



exhibited the desorption peak at around 600°C to 700°C, which could be attributed to near surface lattice oxygen. It could be noticed that Ce loading was accompanied with the desorption peak of near surface lattice oxygen species. Interaction between MnO<sub>x</sub> and CeO<sub>x</sub> in metal oxide solid solution could induce the charge imbalance and promote the formation of oxygen vacancy and surface defect<sup>83, 88</sup>, which may transfer the surrounding bulk lattice oxygen to a near surface lattice oxygen-like energy level. The unsaturated chemical bonds around this surface structure defect could also serve as strong active sites to adsorb and activate gas species. Obviously, the O<sub>2</sub>-TPD profile exhibited a similar behavior with NH<sub>3</sub>-TPD. It could be deduced that the active sites of NH<sub>3</sub> and may have strong association with active sites of O<sub>2</sub>.

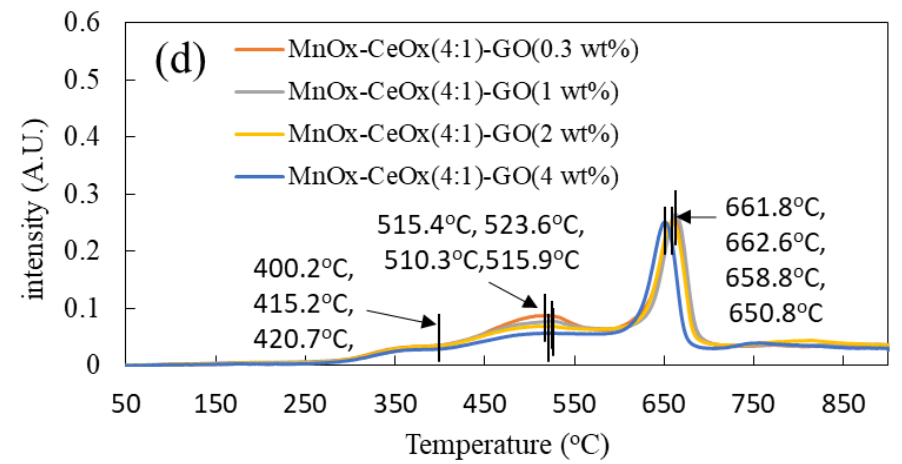
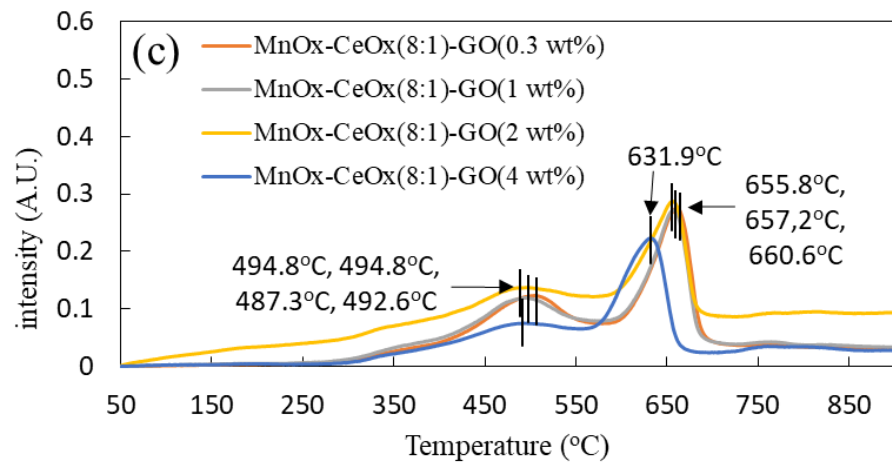
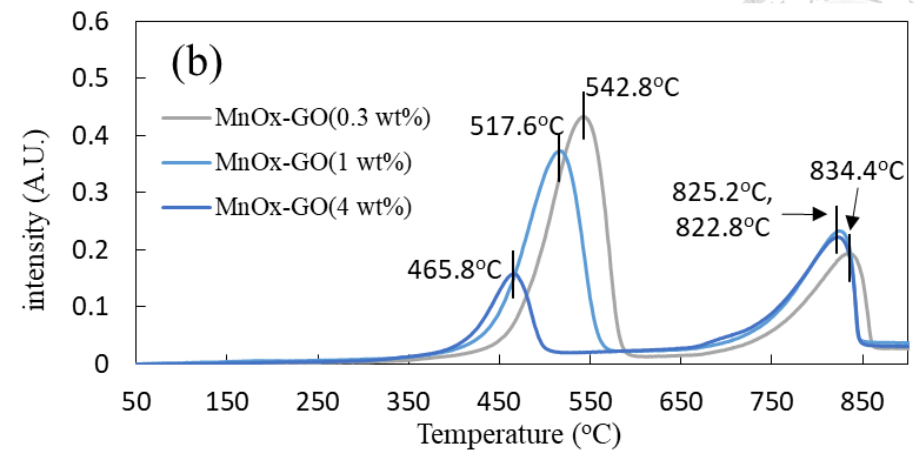
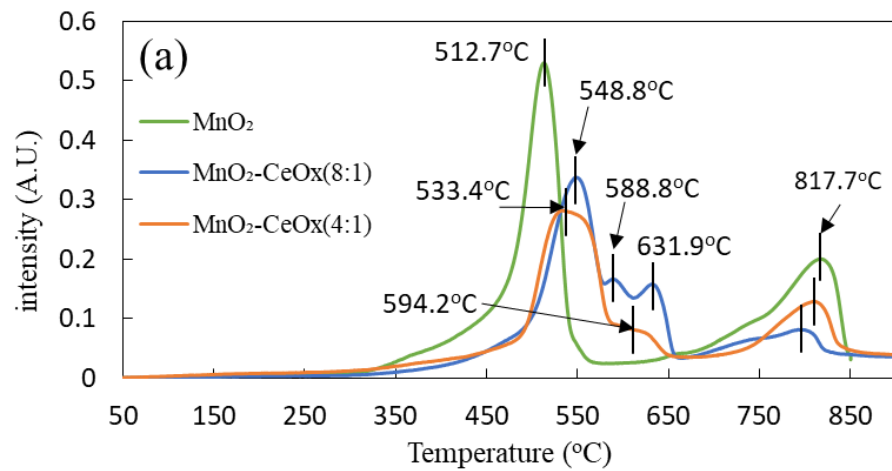


Figure 4-12. O<sub>2</sub>-TPD profile over catalyst

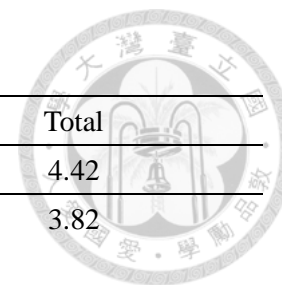
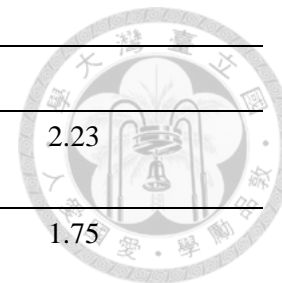


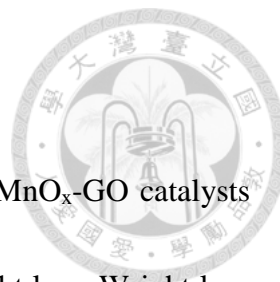
Table 4-5. Quantitative analysis of O<sub>2</sub>-TPD over catalysts.

catalyst	Chemisorbed oxygen (%)	Surface lattice oxygen (%)	Bulk lattice oxygen (%)	Total
MnO <sub>2</sub>	67.8 (512.7 °C)		32.2 (817.7 °C)	4.42
MnO <sub>2</sub> -CeO <sub>x</sub> (8:1)	59.6 (548.8 °C) 11.4 (588.4 °C)	12.8 (631.9 °C)	16.2 (795.7 °C)	3.82
MnO <sub>2</sub> -CeO <sub>x</sub> (4:1)	72.0 (533.4 °C) 7.9 (594.2 °C)		20.1 (810.3 °C)	2.98
MnO <sub>x</sub> -GO(0.3 wt%)	71.4 (542.8 °C)		28.6 (834.4 °C)	4.25
MnO <sub>x</sub> -GO(1 wt%)	65.6 (517.6 °C)		34.4 (825.2 °C)	4.00
MnO <sub>x</sub> -GO(4 wt%)	35.5 (465.8 °C)		65.5(822.8 °C)	2.32
MnO <sub>x</sub> -CeO <sub>x</sub> (8:1) -GO(0.3 wt%)	50.3 (503.0 °C)	49.7 (660.6 °C)		2.68
MnO <sub>x</sub> -CeO <sub>x</sub> (8:1) -GO(1 wt%)	50.3 (494.8 °C)	49.0 (657.2 °C)	0.7 (762.3 °C)	2.71
MnO <sub>x</sub> -CeO <sub>x</sub> (8:1) -GO(2 wt%)	56.0 (487.3 °C)	44.0 (655.8 °C)		2.82
MnO <sub>x</sub> -CeO <sub>x</sub> (8:1) -GO(4 wt%)	41.0 (492.6 °C)	55.6 (631.9 °C)	3.4 (758.8 °C)	2.21
MnO <sub>x</sub> -CeO <sub>x</sub> (4:1) -GO(0.3 wt%)	7.8 (400.2 °C) 41.5 (515.4 °C)	50.7 (661.8 °C)		2.08
MnO <sub>x</sub> -CeO <sub>x</sub> (4:1)	47.7 (523.6 °C)	52.3 (662.6 °C)		1.90





-GO(1 wt%)				
MnO <sub>x</sub> -CeO <sub>x</sub> (4:1)	10.2 (415.2 °C)	49.6 (658.8 °C)	6.6 (794.8 °C)	2.23
-GO(2 wt%)	33.6 (510.3 °C)			
MnO <sub>x</sub> -CeO <sub>x</sub> (4:1)	10.8 (420.7 °C)	54.6 (650.8 °C)	4.0 (754.1 °C)	1.75
-GO(4 wt%)	30.6 (515.9 °C)			



#### 4.1.8. Thermogravimetric analysis (TGA)

The TGA profiles of  $\text{MnO}_x\text{-CeO}_x\text{-GO}$ ,  $\text{MnO}_2\text{-CeO}_x$ ,  $\text{MnO}_2$ , and  $\text{MnO}_x\text{-GO}$  catalysts are shown in Figure 4-13.  $\text{MnO}_2$  exhibited two major stages of weight loss. Weight loss from  $100^\circ\text{C}$  to  $150^\circ\text{C}$  represented the evaporation of physically and chemically adsorbed water. Weight loss from  $500^\circ\text{C}$  to  $700^\circ\text{C}$  represented the series of phase transformations of  $\text{MnO}_x$ , mainly  $\text{MnO}_2 \rightarrow \text{Mn}_2\text{O}_3 \rightarrow \text{Mn}_3\text{O}_4 \rightarrow \text{MnO}$ <sup>47, 74</sup>. Both  $\text{MnO}_2\text{-CeO}_x(8:1)$  and  $\text{MnO}_2\text{-CeO}_x(4:1)$  catalysts adsorbed more water and had a slower weight change profile at around  $200^\circ\text{C}$  to  $500^\circ\text{C}$  and exhibited stepwise dropping profiles from around  $600^\circ\text{C}$  to  $900^\circ\text{C}$  during the metal oxide transformation stage, indicating that  $\text{MnO}_2\text{-CeO}_x$  catalysts had more thermostability than  $\text{MnO}_2$ .  $\text{MnO}_x\text{-GO}(1 \text{ wt}\%)$  and  $\text{MnO}_x\text{-GO}(0.3 \text{ wt}\%)$  catalysts underwent phase transformation at temperatures higher than  $\text{MnO}_2$  ( $600\text{-}700^\circ\text{C}$  for  $\text{MnO}_x\text{-GO}(0.3 \text{ wt}\%)$  and  $650^\circ\text{C}$  to  $750^\circ\text{C}$  for  $\text{MnO}_x\text{-GO}(1 \text{ wt}\%)$ ), and displayed a sharp weight loss profile, yet lost less weight than  $\text{MnO}_2$ .  $\text{MnO}_x\text{-GO}(4 \text{ wt}\%)$  catalyst released much more water than  $\text{MnO}_2$  and other  $\text{MnO}_x\text{-GO}$  catalysts and exhibited a slight phase transformation at about  $500^\circ\text{C}$  to  $600^\circ\text{C}$ . The extent of weight loss and the temperature from phase transformation over the  $\text{MnO}_x\text{-GO}$  catalysts is as follows:  $\text{MnO}_x\text{-GO}(0.3 \text{ wt}\%) > \text{MnO}_x\text{-GO}(1 \text{ wt}\%) > \text{MnO}_x\text{-GO}(4 \text{ wt}\%)$ . These results indicate that the addition of GO could decrease the amounts of weak Mn-O bonds and enhance the

thermostability of MnO<sub>x</sub>-GO catalysts.

All TGA curves of MnO<sub>x</sub>-CeO<sub>x</sub>-GO catalysts displayed greater water evaporation than other kinds of catalysts besides MnO<sub>x</sub>-GO(4 wt%). In the weight loss curve of the phase transformation, all MnO<sub>x</sub>-CeO<sub>x</sub>-GO catalysts exhibited the stepped-down drop from as low as 300°C and showed a sharper decline from 600°C to 800°C, which originated from the effects of Ce and GO. Ce may enhance the thermostability of the catalyst and multi-valence redox cycle of metal oxide by oxygen storage and supply ability.



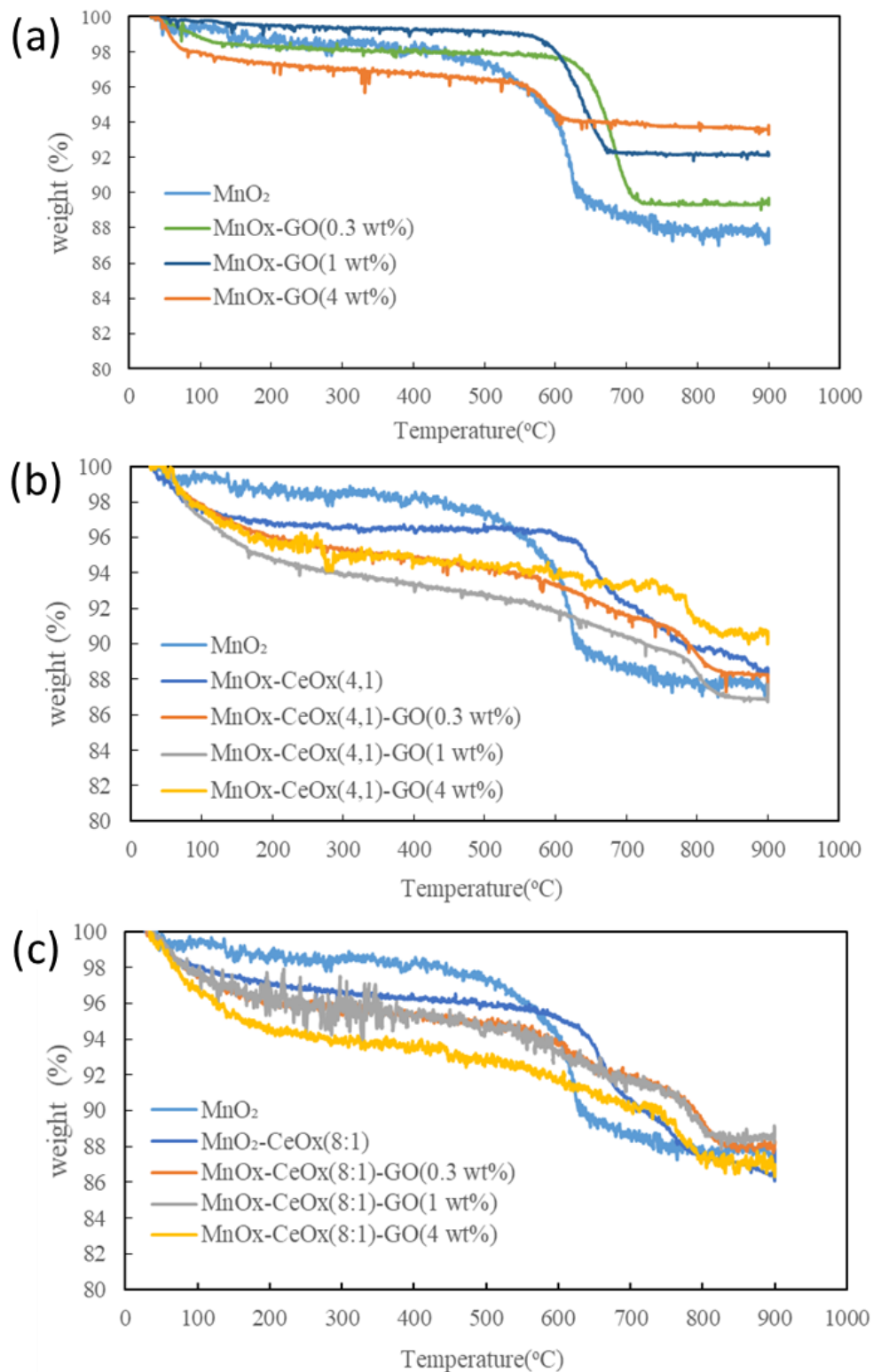


Figure 4-13. TGA curves of MnO<sub>x</sub>-GO, MnO<sub>2</sub>-CeO<sub>x</sub>(4:1)-GO and MnO<sub>x</sub>-CeO<sub>x</sub>(8:1)-GO catalysts with different amounts of GO addition.

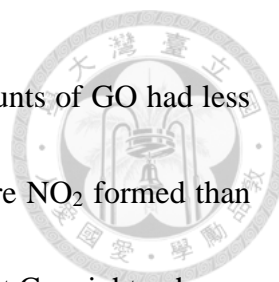


## 4.2. NO removal test

### 4.2.1. NH<sub>3</sub>-SCR and NO oxidation activity test

The NO conversion and NO<sub>2</sub> formation of different catalysts over NH<sub>3</sub>-SCR from around 60°C to 330°C are shown in the following figures. The NO conversion of most MnO<sub>x</sub>-CeO<sub>x</sub>-GO catalysts could reach up to 60% and generated less than 10 ppm NO<sub>2</sub> from 60°C to 120°C, which showed the extraordinary low-temperature NH<sub>3</sub>-SCR activity and reaction selectivity. This performance is consistent with the XPS result shown in Figures 4-8 to 4-9, Table 4-2, and Lewis acid site desorption shown in Figure 4-10. For higher temperatures at about 180°C to 270°C, the NO conversion maintained at up to 90%, but NO<sub>2</sub> formation was highly promoted. Among all the MnO<sub>x</sub>-CeO<sub>x</sub>(8:1)-GO catalysts, MnO<sub>x</sub>-CeO<sub>x</sub>(8:1)-GO(0.3 wt%) catalyst had the best NH<sub>3</sub>-SCR activity, which could reach up to 95% NO conversion at 150°C and 180°C. For MnO<sub>x</sub>-CeO<sub>x</sub>(4:1)-GO catalysts, optimized NO conversion was reached at about 210°C to 240°C with the formation of 30 ppm to 40 ppm NO<sub>2</sub>. Generally, MnO<sub>x</sub>-CeO<sub>x</sub>(8:1)-GO catalysts exhibited slightly higher NO conversion and lower NO<sub>2</sub> formation than MnO<sub>x</sub>-CeO<sub>x</sub>(4:1)-GO catalysts.

Figures 4-14(b) and 4-15(b) show the NO<sub>2</sub> formation of MnO<sub>x</sub>-CeO<sub>x</sub>(8:1)-GO and MnO<sub>x</sub>-CeO<sub>x</sub>(4:1)-GO over the NH<sub>3</sub>-SCR, respectively. For the MnO<sub>x</sub>-CeO<sub>x</sub>(8:1)-GO, MnO<sub>x</sub>-CeO<sub>x</sub>(8:1)-GO(2 wt%) catalyst generated the least NO<sub>2</sub> during the NH<sub>3</sub>-SCR



reaction. For the  $\text{MnO}_x\text{-CeO}_x(4:1)\text{-GO}$  catalysts, the additional amounts of GO had less of a relationship with  $\text{NO}_2$  formation during the  $\text{NH}_3\text{-SCR}$ , and more  $\text{NO}_2$  formed than  $\text{MnO}_x\text{-CeO}_x(8:1)\text{-GO}$  catalysts during  $\text{NH}_3\text{-SCR}$ , which indicates that Ce might enhance the reaction by strengthening the adsorption and activation of NO.

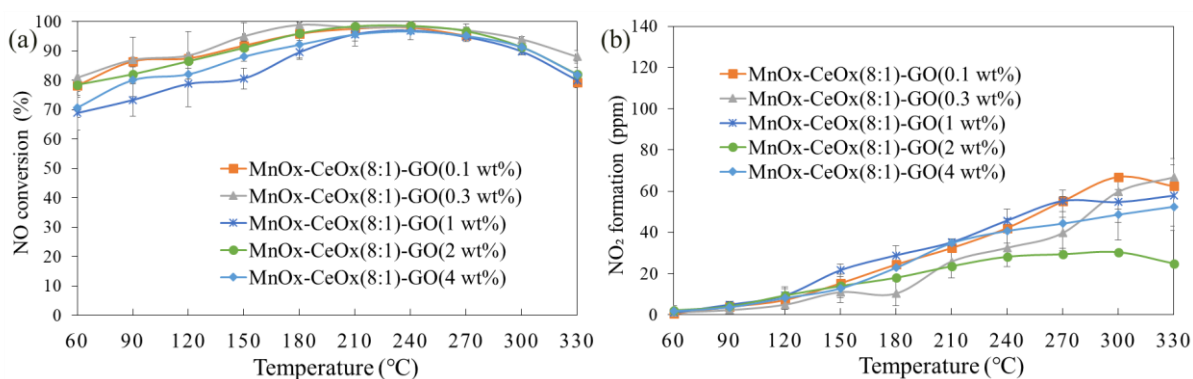


Figure 4-14. NO conversion and  $\text{NO}_2$  formation of  $\text{MnO}_x\text{-CeO}_x(8:1)\text{-GO}$  catalysts with different amounts of GO over the  $\text{NH}_3\text{-SCR}$ .

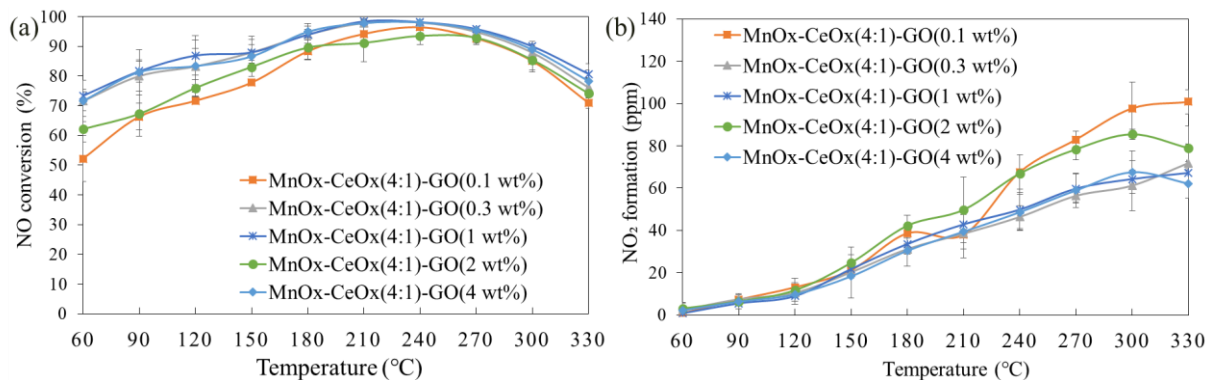
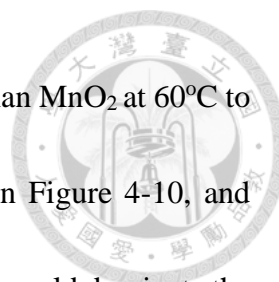


Figure 4-15. NO conversion and  $\text{NO}_2$  formation of  $\text{MnO}_x\text{-CeO}_x(4:1)\text{-GO}$  catalysts with different amounts of GO over the  $\text{NH}_3\text{-SCR}$ .

Figure 4-16 shows the NO conversion and  $\text{NO}_2$  formation of  $\text{MnO}_2$  and  $\text{MnO}_2\text{-CeO}_x$  during the  $\text{NH}_3\text{-SCR}$ , respectively.  $\text{MnO}_2$  possessed 80% NO conversion at 150°C



270°C. Both MnO<sub>2</sub>-CeO<sub>x</sub> performed slightly better NO conversion than MnO<sub>2</sub> at 60°C to 120°C, which was consistent with the result of NH<sub>3</sub>-TPD shown in Figure 4-10, and indicates that MnO<sub>2</sub>-CeO<sub>x</sub> possesses more Lewis acid active sites that could dominate the reaction in low temperatures. For the NO<sub>2</sub> formation, all three catalysts only generated slight amounts from about 60°C to 120°C, but gradually increased after 150°C. NO<sub>2</sub> formation during the NH<sub>3</sub>-SCR between three catalysts was as follows: MnO<sub>2</sub>-CeO<sub>x</sub>(4:1) > MnO<sub>2</sub>-CeO<sub>x</sub>(8:1) > MnO<sub>2</sub>.

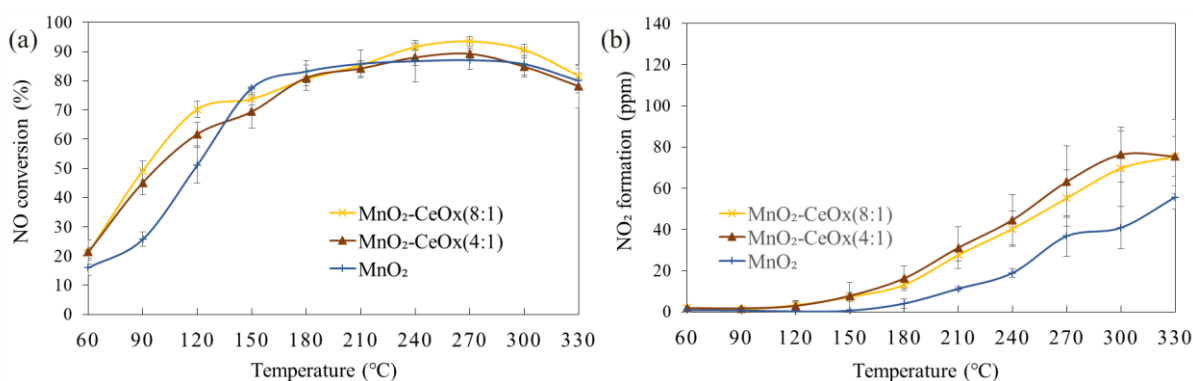
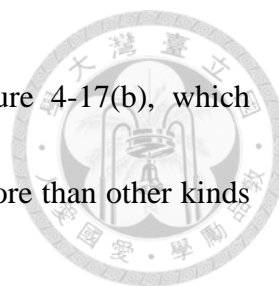


Figure 4-16. NO conversion and NO<sub>2</sub> formation of MnO<sub>2</sub> and MnO<sub>2</sub>-CeO<sub>x</sub> catalysts over the NH<sub>3</sub>-SCR.

Figure 4-17 (a) shows the NO conversion of MnO<sub>x</sub>-GO catalysts with different amounts of GO addition during the NH<sub>3</sub>-SCR. MnO<sub>x</sub>-GO(1 wt%) catalyst and MnO<sub>x</sub>-GO(4 wt%) catalyst exhibited better NO conversion than MnO<sub>2</sub> over the whole temperature profile. However, MnO<sub>x</sub>-GO(0.3 wt%) catalyst exhibited low NO conversion, which may be due to the small specific surface area as shown in Table 4-1. NO<sub>2</sub> formation



during  $\text{NH}_3$ -SCR over the  $\text{MnO}_x$ -GO catalysts is shown in Figure 4-17(b), which illustrates that  $\text{MnO}_x$ -GO catalysts could catalyze  $\text{NO}_2$  formation more than other kinds of catalysts.

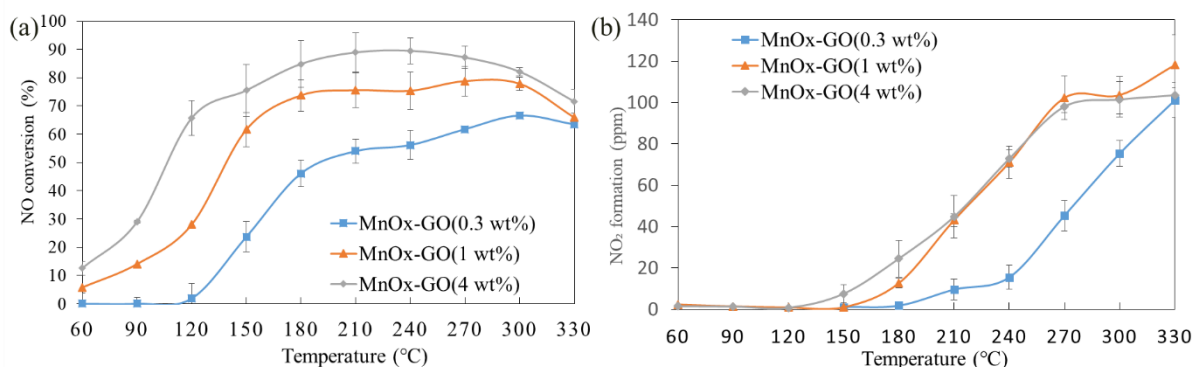



Figure 4-17. NO conversion and  $\text{NO}_2$  formation of  $\text{MnO}_x$ -GO catalysts with different amounts of GO over the  $\text{NH}_3$ -SCR.

Figure 4-18 shows the NO oxidation of all catalysts over 150°C to 330°C. For all kinds of catalysts, most of their NO oxidation activity showed a narrow peak, bell-shaped profile. The conversion of  $\text{MnO}_2$  and  $\text{MnO}_2$ - $\text{CeO}_x$  was only 10% at 150°C. As the reaction temperature increased, 75% conversion was achieved at 270°C to 300°C.  $\text{MnO}_x$ -GO(1 wt%) catalyst reached at 75% maximum NO conversion at 270°C to 300°C and  $\text{MnO}_x$ -GO(4 wt%) catalyst reached at 80% maximum NO conversion 240°C to 270°C. Nevertheless,  $\text{MnO}_x$ -GO(0.3 wt%) catalyst showed lower NO conversion than  $\text{MnO}_2$  with only 40% NO conversion at 270°C. The variation of catalytic performance may mainly originate from the difference in specific surface area.





In Figure 4-18 (a and b),  $\text{MnO}_x\text{-CeO}_x\text{-GO}$  catalysts showed more significant activity for NO oxidation than  $\text{MnO}_2$ ,  $\text{MnO}_2\text{-CeO}_x$ , and  $\text{MnO}_x\text{-GO}$  catalysts. All kinds of  $\text{MnO}_x\text{-CeO}_x\text{-GO}$  catalysts maintained at least 20% conversion at 150°C and reached nearly 80% conversion at 270°C. After the temperature raised to 270°C, the oxidation activity decayed as the temperature gradually increased. For  $\text{MnO}_x\text{-CeO}_x(8:1)\text{-GO}$  catalysts during NO oxidation test over 150°C to 210°C, NO conversion would increase with increasing amounts of GO. However, this relationship between additional GO and NO conversion was not apparent for  $\text{MnO}_x\text{-CeO}_x(4:1)\text{-GO}$  catalysts under the same reaction conditions, even if the general conversion profile over different temperatures was similar as  $\text{MnO}_x\text{-CeO}_x(8:1)\text{-GO}$  catalysts. Among all kinds of  $\text{MnO}_x\text{-CeO}_x\text{-GO}$  catalysts,  $\text{MnO}_x\text{-CeO}_x\text{-GO}(2 \text{ wt}\%)$  exhibited the best catalytic performance, with 90.1% ( $\text{Mn}/\text{Ce} = 8$ ) and 89.9% ( $\text{Mn}/\text{Ce} = 4$ ) at 240°C.

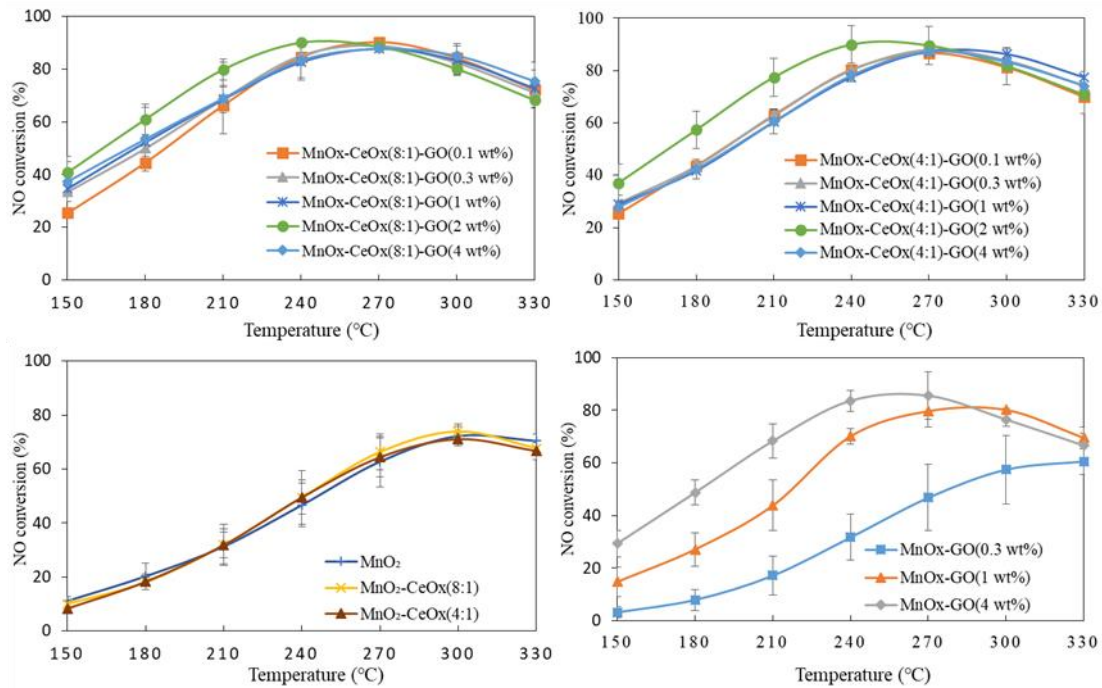
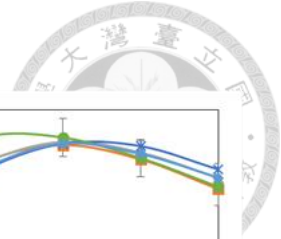
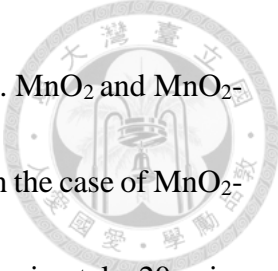


Figure 4-18. NO conversion of different catalysts over the NO oxidation.

#### 4.2.2. Sulfur and water tolerance over NH<sub>3</sub>-SCR

The deNO<sub>x</sub> catalyst bed is usually installed in a position that would be exposed to flue gas containing reactive species like SO<sub>2</sub> and H<sub>2</sub>O, which causes poisoning on the catalyst. To study the poisoning impact on the catalyst, the single and congrate effect caused by 1.5 h of purging with H<sub>2</sub>O and SO<sub>2</sub> over the NH<sub>3</sub>-SCR was evaluated in the following experiments. Figure 4-19 (a and b) shows the effect of 200 ppm SO<sub>2</sub> on the NO conversion of MnO<sub>x</sub>-CeO<sub>x</sub>-GO catalysts at 180°C. For MnO<sub>2</sub> and MnO<sub>2</sub>-CeO<sub>x</sub>, NO conversion severely declined as SO<sub>2</sub> passed through. The NO conversion of MnO<sub>2</sub> and MnO<sub>2</sub>-CeO<sub>x</sub>(8:1) declined after SO<sub>2</sub> passed for 15-30 min, and the conversion profile slightly



recovered for approximately half an hour before reaching equilibrium.  $\text{MnO}_2$  and  $\text{MnO}_2\text{-CeO}_x(8:1)$  demonstrated 50% and 35% NO conversion, respectively. In the case of  $\text{MnO}_2\text{-CeO}_x(4:1)$ , the decline happened after  $\text{SO}_2$  was passed in for approximately 20 min. Subsequently, the conversion declination of  $\text{MnO}_2\text{-CeO}_x(4:1)$  occurred and lasted for 30 min, as NO conversion would then start to recover equilibrium. After cutting off  $\text{SO}_2$ , NO conversion of  $\text{MnO}_2\text{-CeO}_x(8:1)$  again started to decay immediately to about 10% conversion.

After  $\text{SO}_2$  was cut off, NO conversion of  $\text{MnO}_2\text{-CeO}_x(4:1)$  catalysts and  $\text{MnO}_2$  decayed until NO conversion reached 10% and 20%, respectively. For  $\text{MnO}_x\text{-CeO}_x\text{-GO}$  catalysts, both the decline and slight recovery of NO conversion after  $\text{SO}_2$  was passed in also appeared. The time that NO conversion of  $\text{MnO}_x\text{-CeO}_x\text{-GO}$  catalysts declined after  $\text{SO}_2$  passing in and the time that NO conversion started to recover were longer and later than  $\text{MnO}_2\text{-CeO}_x$  catalysts and  $\text{MnO}_2$ . After cutting off  $\text{SO}_2$ , only  $\text{MnO}_x\text{-CeO}_x(4:1)$  and  $8:1\text{-GO}(0.3 \text{ wt}\%)$  and  $\text{MnO}_x\text{-CeO}_x(8:1)\text{-GO}(1 \text{ wt}\%)$  exhibited the decrease of NO conversion. For all kinds of  $\text{MnO}_x\text{-CeO}_x\text{-GO}$  catalysts, the NO conversion after 200ppm  $\text{SO}_2$  cutting off at  $180^\circ\text{C}$  was as follows:  $\text{MnO}_x\text{-CeO}_x\text{-GO}(4 \text{ wt}\%) > \text{MnO}_x\text{-CeO}_x\text{-GO}(1 \text{ wt}\%) > \text{MnO}_x\text{-CeO}_x\text{-GO}(0.3 \text{ wt}\%)$ .

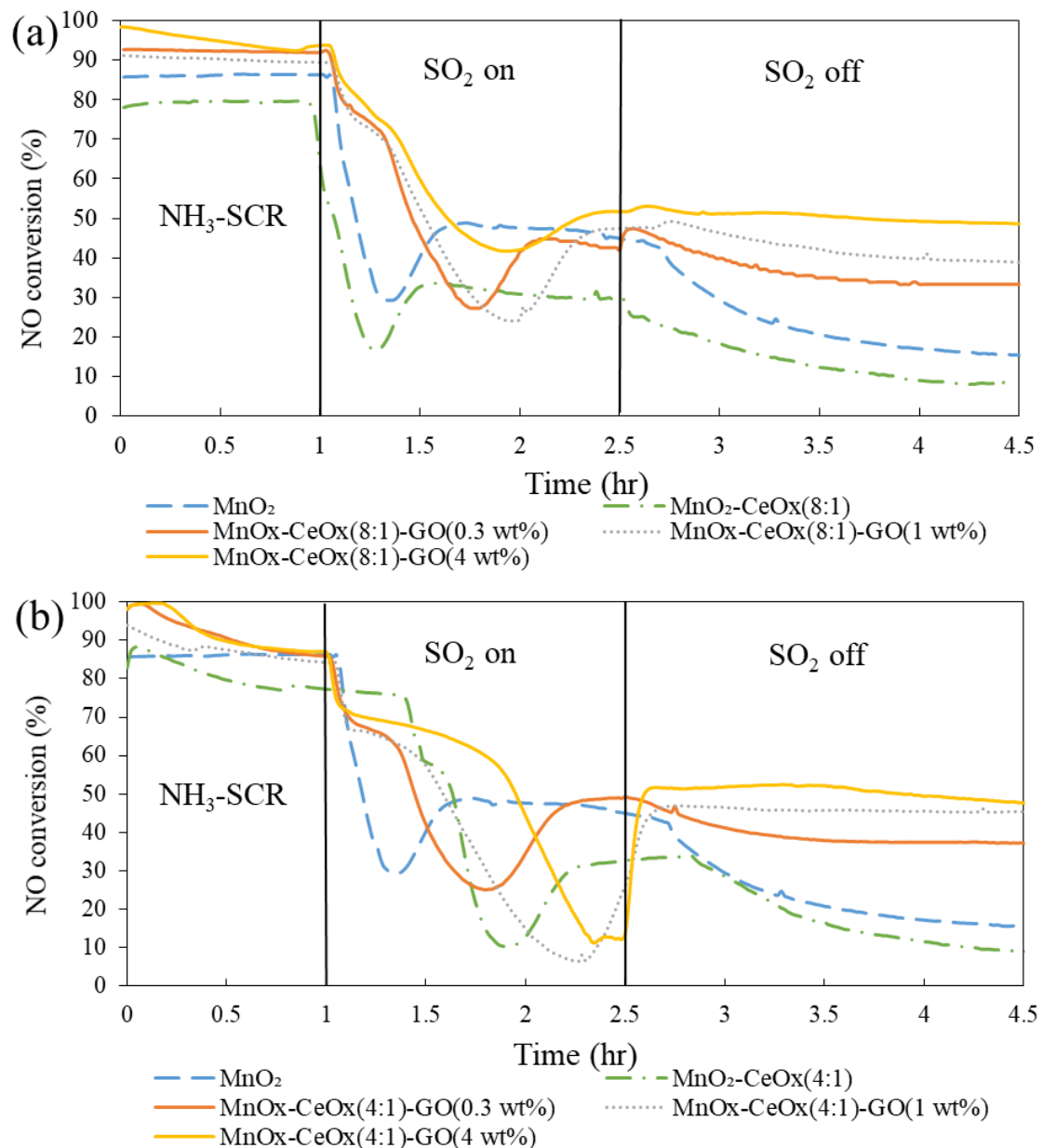
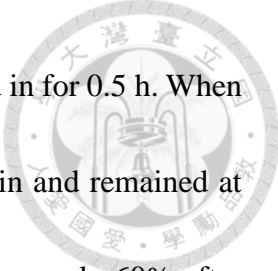


Figure 4-19. Sulfur tolerance test for NO conversion of  $\text{MnO}_x\text{-CeO}_x(8:1$  and  $4:1)\text{-GO}$  over the  $\text{NH}_3\text{-SCR}$  activity test at  $180^\circ\text{C}$ .

The sulfur effect on NO conversion of catalysts over the higher temperature was also investigated. Figure 4-20 shows the variation of NO conversion of  $\text{MnO}_2$ ,  $\text{MnO}_2\text{-CeO}_x(8:1)$  catalyst and  $\text{MnO}_x\text{-CeO}_x(8:1)\text{-GO}$  catalysts when the  $\text{SO}_2$  was treated over  $270^\circ\text{C}$ . The NO conversion of  $\text{MnO}_2$  and  $\text{MnO}_2\text{-CeO}_x(8:1)$  catalyst declined more quickly



and severely than at 180°C, but began to recover after SO<sub>2</sub> was passed in for 0.5 h. When the SO<sub>2</sub> was cut off, NO conversion of MnO<sub>2</sub> slightly decreased again and remained at about 50%. On the contrary, NO conversion of MnO<sub>2</sub>-CeO<sub>x</sub>(8:1) was nearly 60% after SO<sub>2</sub> was cut off for 20 min or so, which shows that MnO<sub>2</sub>-CeO<sub>x</sub>(8:1) possesses higher sulfur tolerance than MnO<sub>2</sub>. For MnO<sub>x</sub>-CeO<sub>x</sub>(8:1)-GO catalysts, the decline of NO conversion lasted between 0.5 to 1.5 h depending on the catalyst, where subsequently, evident recovery occurred. NO conversion of MnO<sub>x</sub>-CeO<sub>x</sub>(8:1)-GO(0.3 wt%) and MnO<sub>x</sub>-CeO<sub>x</sub>(8:1)-GO(4 wt%) recovered to 80% after SO<sub>2</sub> was cut off. Moreover, MnO<sub>x</sub>-CeO<sub>x</sub>-GO(1 wt%) recovered to 70% NO conversion.

In Figure 4-20(b), MnO<sub>2</sub>-CeO<sub>x</sub>(4:1)-GO and MnO<sub>2</sub>-CeO<sub>x</sub>(4:1) showed higher NO conversion than MnO<sub>x</sub>-CeO<sub>x</sub>(8:1)-GO and MnO<sub>2</sub>-CeO<sub>x</sub>(8:1) while SO<sub>2</sub> passed. Unlike MnO<sub>x</sub>-CeO<sub>x</sub>(8:1)-GO catalysts and MnO<sub>2</sub>-CeO<sub>x</sub>(8:1) catalyst, NO conversion of MnO<sub>2</sub>-CeO<sub>x</sub>(4:1) and MnO<sub>x</sub>-CeO<sub>x</sub>(4:1)-GO catalysts only decayed slightly. Even in the most severe case, the NO conversion only dropped to about 60% with MnO<sub>x</sub>-CeO<sub>x</sub>(4:1)-GO(4 wt%) as the catalyst. After SO<sub>2</sub> was cut off, NO conversion of MnO<sub>2</sub>-CeO<sub>x</sub>(4:1) catalysts and MnO<sub>x</sub>-CeO<sub>x</sub>(4:1)-GO catalysts recovered to about 75%.

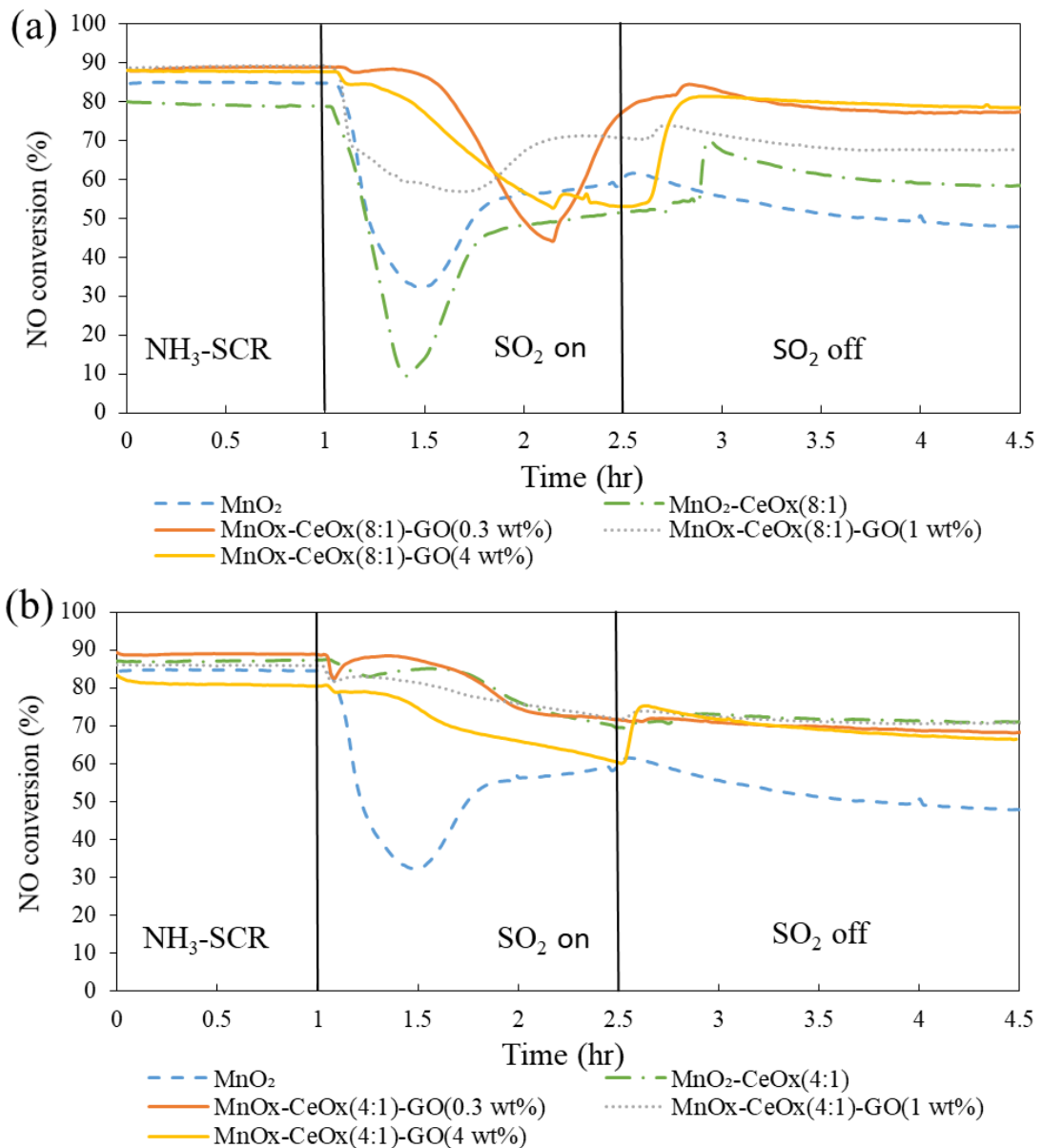



Figure 4-20. Sulfur tolerance test for NO conversion of MnO<sub>x</sub>-CeO<sub>x</sub>(8:1 and 4:1)-GO over the NH<sub>3</sub>-SCR activity test at 270°C.

The poisoning effect caused by SO<sub>2</sub> may originate from both the formation of ammonium sulfate species and metal sulfation. Ammonium sulfate species aggregate on the surface of catalysts and block the active sites of catalytic reaction<sup>55-56, 89</sup>. The sulfation



of metal oxide species hindered the significant NO-adsorbed intermediate from forming and prevented the catalytic reaction from operation<sup>59, 90</sup>. The difference between the variation of NO conversion between NH<sub>3</sub>-SCR performed at about 180°C and 270°C showed that the poisoning effect could be overcome by increasing the temperature, revealing that the SO<sub>2</sub> poisoning effect was mainly caused by the formation of ammonium sulfate species, as ammonium sulfate species can decompose at a higher temperature<sup>57-58</sup>. During the sulfur tolerance test at 180°C, the NO conversion profile of most catalysts showed a steady decrease after SO<sub>2</sub> was cut off. This phenomenon seems to contradict the assumption that SO<sub>2</sub> causes the poisoning on the catalyst, but some research has also indicated that additional Bronsted acid sites could form during the generation of cerium sulfate species, which slightly promote the NH<sub>3</sub>-SCR<sup>61, 91</sup>. As a result, the NO conversion profile variation was the result of synergistic interaction of the SO<sub>2</sub> poisoning effect and the increase of Bronsted acid sites. For lower temperatures in which ammonium sulfate species couldn't decompose, namely 180°C, the poisoning effect and the increase of the Bronsted acid sites began simultaneously, which generated the profile that decayed first and recovered slightly as SO<sub>2</sub> was introduced. When the SO<sub>2</sub> was cut off, the increase of Bronsted acid sites ceased, but the ammonium sulfate species had formed and blocked the active sites of catalysts, thus the NO conversion would decay to some extent after



cutting off SO<sub>2</sub>.

At 180°C, the NO conversion after the SO<sub>2</sub> poisoning effect of MnO<sub>x</sub>-CeO<sub>x</sub>-GO catalysts revealed that GO had a positive effect on sulfur tolerance during NH<sub>3</sub>-SCR. Su, et al.<sup>71</sup> concluded that this effect came from the pre-sulfation from GO due to the use of sulfuric acid during the synthesis of GO. Costa, et al.<sup>92</sup> proposed the mechanism of pre-sulfation: sulfate ion covered on the catalyst may prevent the gas phase SO<sub>2</sub> or SO<sub>3</sub> from attaching to the surface of the catalyst by the steric effect, which could hinder the SO<sub>2</sub> or SO<sub>3</sub> from attacking the Mn atom acid sites. You, et al.<sup>7</sup> deduced that graphene could promote the dispersion of metal, which may enhance the sulfur tolerance of catalysts by further dispersion of Ce, and may enhance the reaction between SO<sub>2</sub> and Cerium.

For reactions conducted at 270°C, the NO conversion profile of MnO<sub>x</sub>-CeO<sub>x</sub>(8:1)-GO that recovered after SO<sub>2</sub> passed in, implied that ammonium sulfate species formed on catalysts auto-decompose. For the case of MnO<sub>x</sub>-CeO<sub>x</sub>(4:1)-GO catalysts, NO conversion higher than MnO<sub>x</sub>-CeO<sub>x</sub>(4:1)-GO catalysts was shown during the exposure to SO<sub>2</sub>, but the same phenomenon was not shown for NH<sub>3</sub>-SCR at 180°C. Furthermore, NO conversion of most of the MnO<sub>2</sub>-CeO<sub>x</sub>(4:1) MnO<sub>x</sub>-CeO<sub>x</sub>(4:1)-GO catalysts started to decline when SO<sub>2</sub> was passed in at a later time than MnO<sub>x</sub>-CeO<sub>x</sub>(8:1)-GO catalysts. This may imply that a higher Ce ratio could enhance the sulfur tolerance of catalysts by the




increase of Bronsted acid sites, forming less-thermostable Ce sulfate species<sup>62</sup>, promoting the formation of ammonium sulfate species, or the interaction of all above three reasons.

This is because more Ce indicates more Bronsted acid sites promoted the NH<sub>3</sub>-SCR because Ce could trap sulfur species and generate Ce sulfate species, which could postpone the time that catalysts start to undergo more critical poisoning due to the formation of ammonium sulfate species and Ce sulfate species.

Water also appears in flue gas due to the adding of a reducing agents, or the location of the pollution control upstream of the SCR catalyst bed. Figure 4-21 showed the effect of water on NO conversion of catalysts at 180 °C. NO conversion of MnO<sub>2</sub> and MnO<sub>2</sub>-CeO<sub>x</sub> catalysts decayed after water was passed in. Catalytic performance of MnO<sub>2</sub>-CeO<sub>x</sub>(8:1) decayed the most, from 80% to 35% after water was passed in for 1 h, and the decay of catalytic performance largely recovered after cutting off the water. For MnO<sub>2</sub> and MnO<sub>2</sub>-CeO<sub>x</sub>(4:1), NO conversion as water was passed in, decayed from 80% to 55%, and recovered to its original value after water was cut off. Catalytic performance of MnO<sub>x</sub>-CeO<sub>x</sub>(8:1)-GO only decreased slightly during the purging of water, and also almost fully recovered after cutting off the water, while NO conversion of MnO<sub>x</sub>-CeO<sub>x</sub>(4:1)-GO catalysts did not notably decline.

Water tolerance of MnO<sub>x</sub>-CeO<sub>x</sub>-GO catalysts could be attributed to the hydrophobic



characteristics of the carbon-based material. Su, et al.<sup>71</sup> and You, et al.<sup>7</sup> indicated that the hydrophobic GO prevented water from being adsorbed and compete active sites with reactants like NH<sub>3</sub>. All the catalysts' ability to recover indicated that the poisoning effect caused by water is reversible.

Contribution on water tolerance ability from Ce could be seen from the difference between NO conversion of MnO<sub>x</sub>-CeO<sub>x</sub>(8:1)-GO and MnO<sub>x</sub>-CeO<sub>x</sub>(4:1)-GO catalysts when water was purged in. The enhancement of water tolerance from Ce addition may be caused by the type of acid sites. Ma, et al.<sup>82</sup> observed that Ce addition could increase the ratio of Lewis acid sites, which are more hydrophobic than Bronsted acid sites. The relative phenomenon could be observed in this study. The ratio of Lewis acid sites in the total acid sites of MnO<sub>x</sub>-CeO<sub>x</sub>(4:1)-GO catalysts was larger than MnO<sub>x</sub>-CeO<sub>x</sub>(8:1)-GO catalyst except MnO<sub>x</sub>-CeO<sub>x</sub>-GO(4 wt%) catalyst.

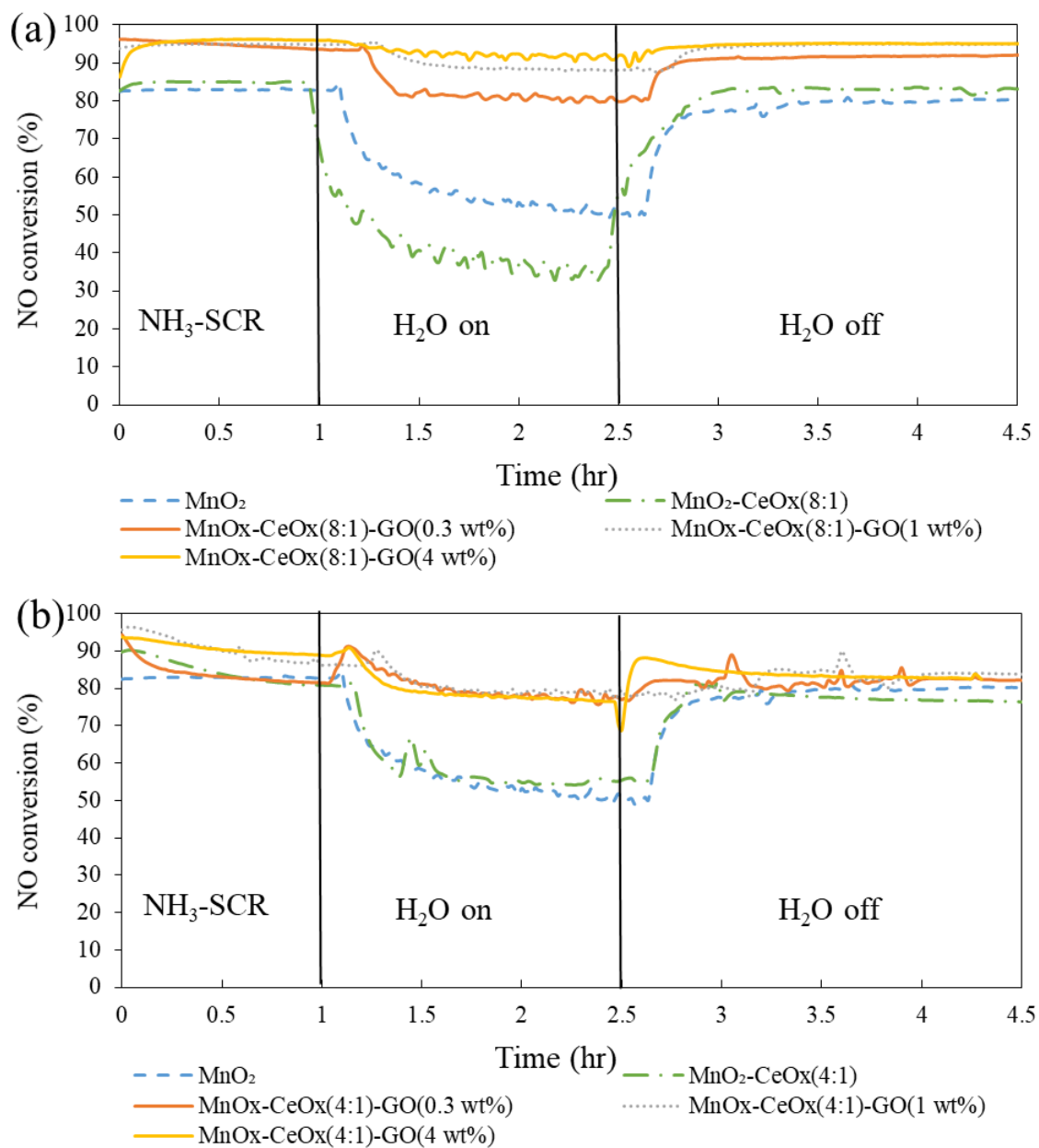


Figure 4-21. Water tolerance test for NO conversion of (a) MnO<sub>x</sub>-CeO<sub>x</sub>(8:1)-GO catalysts and (b) MnO<sub>x</sub>-CeO<sub>x</sub>(4:1)-GO catalysts over the NH<sub>3</sub>-SCR activity test at 180°C.

Figure 4-22 shows the change of catalytic performance when water and SO<sub>2</sub> were both passed in. NO conversion of MnO<sub>2</sub> and MnO<sub>2</sub>-CeO<sub>x</sub>(8:1) decreased more quickly than MnO<sub>x</sub>-CeO<sub>x</sub>(8:1)-GO catalysts, which decayed to 30% and 40% respectively after 0.5 h.



After passing in SO<sub>2</sub> and water for 0.5 h, the NO conversion started to recover to about 50-60% and 60-70% for MnO<sub>2</sub> and MnO<sub>2</sub>-CeO<sub>x</sub>(8:1), respectively. After the cut off of SO<sub>2</sub> and H<sub>2</sub>O, the NO conversion of MnO<sub>2</sub> and MnO<sub>2</sub>-CeO<sub>x</sub>(8:1) recovered to 50% and 80%, respectively. For MnO<sub>x</sub>-CeO<sub>x</sub>(8:1)-GO catalysts, NO conversion decayed slower, and even more severely than the decay situation in an atmosphere which only contained SO<sub>2</sub> at the same temperature. This may be resulted by two reasons: (1) water enhanced the formation of ammonium sulfate or even other metal sulfates; (2) the poisoning effect was caused by the SO<sub>2</sub> and water individually, though the processes occurred simultaneously.

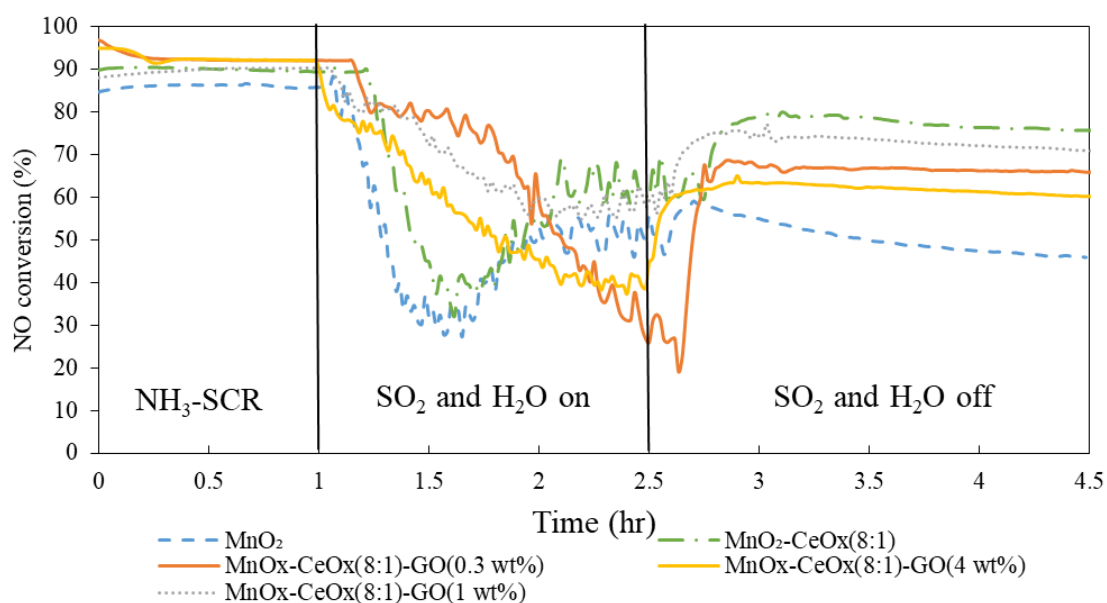


Figure 4-22. Water and sulfur tolerance test for NO conversion of MnO<sub>x</sub>-CeO<sub>x</sub>(8:1)-GO over the NH<sub>3</sub>-SCR activity test at 270°C.

### 4.3. Comprehensive discussion

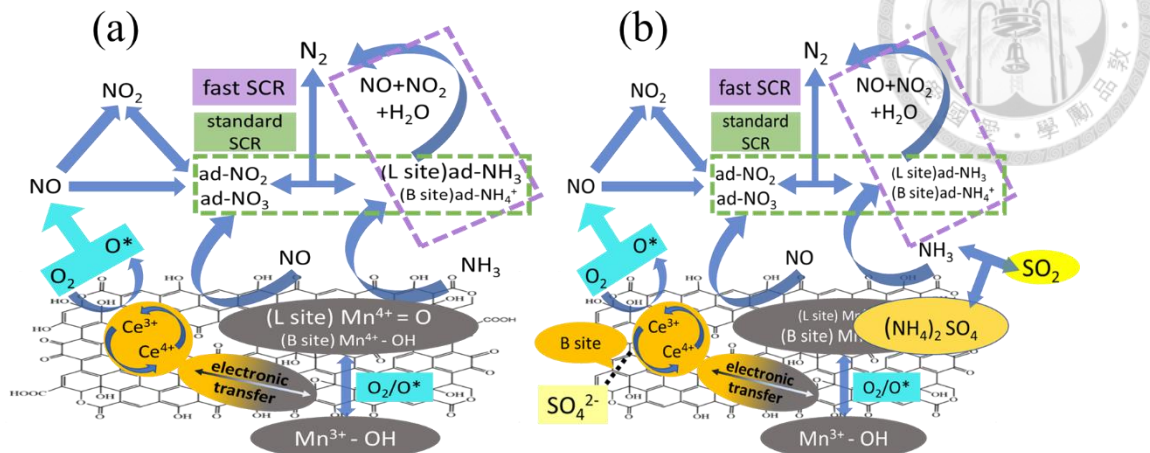
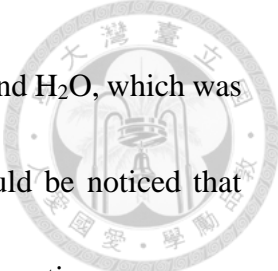


Figure 4-23. Proposed mechanism of NO<sub>x</sub> removal over MnO<sub>x</sub>-CeO<sub>x</sub>-GO catalysts. (a): in the absence of SO<sub>2</sub>; (b): in the presence of SO<sub>2</sub>

By summarizing the above results, the possible mechanism could be organized in the Figure 5-1. As shown in BET, XRD, XPS data and H<sub>2</sub>-TPR profile, GO could highly disperse the metal oxide and promote the solid solution formation, which enhanced the redox cycle between MnO<sub>x</sub> and CeO<sub>x</sub> and further promote the NH<sub>3</sub>-SCR and NO oxidation. MnO<sub>x</sub> served as the major active site. CeO<sub>x</sub> could enhance the reaction by inducing the formation of low-temperature reactive acidic sites like Lewis acid sites, maintaining the supply of reactive oxygen species for catalytic reaction and promoting the formation of high reactive active sites like oxygen vacancy.

When both NO and NH<sub>3</sub> exist in flue gas, they would adsorb on the active sites and was transformed into adsorbed NO species like nitrite or nitrate and adsorbed NH<sub>3</sub> species like coordinate NH<sub>3</sub> (in Lewis acid sites) and ammonium ion (in Bronsted acid sites),



respectively. Those intermediates may directly react and produce  $N_2$  and  $H_2O$ , which was so-called standard SCR. From the result of NO removal test, it could be noticed that  $MnO_x$ - $CeO_x$ -GO catalysts could catalyze the NO oxidation.  $NO_2$  formation may come from the reaction between NO and adsorbed oxygen species, between NO and  $O_2$  (in gas phase) or release of adsorbed NO species.  $NO_2$  may release or participate the so-called fast SCR, which is the reaction that  $NO_2$  would react with NO,  $H_2O$  and adsorbed  $NH_3$  species and generate  $N_2$  through a series of transformation.

In the presence of  $SO_2$ ,  $SO_2$  may react with ammonium and cause the blockage of active sites by ammonium sulfate species.  $CeO_x$  can promote the formation of less thermostable sulfate species and the formation of Bronsted acid sites, but the contribution from Bronsted acid sites toward  $NH_3$ -SCR couldn't fully compensate the negative effect of metal sulfation and ammonium sulfate species blockage.

## Chapter 5. Conclusion and Recommendations



### 5.1. Conclusion

This study investigates the NO removal activity by NH<sub>3</sub>-SCR and NO oxidation.

Several physicochemical methods were conducted to realize the properties of the catalysts.

The general conclusions are summarized below:

1. The result of XPS reveals the role of GO and Ce. GO could promote the dual redox cycle between Mn and Ce, which is important for the NH<sub>3</sub>-SCR and NO oxidation.
2. MnO<sub>x</sub>-CeO<sub>x</sub>-GO catalysts possess excellent activity during low-temperature NH<sub>3</sub>-SCR, which is consistent with the significant Lewis acid sites desorption revealed by NH<sub>3</sub>-TPD.
3. MnO<sub>x</sub>-CeO<sub>x</sub>-GO catalysts also show notable activity during NO oxidation at about 200°C to 300°C, which is consistent with the vigorous NO<sub>2</sub> formation during NH<sub>3</sub>-SCR.
4. Ce could enhance the sulfur tolerance during the NH<sub>3</sub>-SCR of Mn-based catalysts at higher temperature (like 270°C) by the formation of Ce sulfate and promotion on the decomposition of ammonium sulfate.
5. MnO<sub>x</sub>-CeO<sub>x</sub>-GO catalysts also shows outstanding water tolerance. In consideration of the excellent activity of low temperature NH<sub>3</sub>-SCR, it implies that this catalyst may be suitable for the usage of NH<sub>3</sub>-SCR catalyst bed installed in the position behind the WFGD.

## 5.2. Recommendations for future work



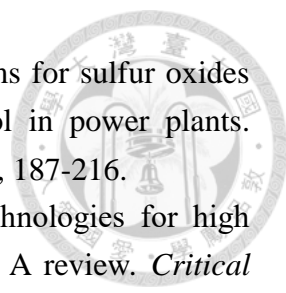
While the results from the presented study provide advances in the area of NO removal, there are still points that require further study. Some of these points are introduced below:

1. The mechanism and dynamic changes during the reaction still need to be investigated.
2.  $\text{MnO}_x\text{-CeO}_x\text{-GO}$  catalysts also show high NO oxidation activity. It may be possible for using additional oxidants like  $\text{ClO}_2$  or  $\text{O}_3$  to enhance the oxidation activity of NO further at lower temperature.
3. For the  $\text{MnO}_x\text{-CeO}_x\text{-GO}$  usage of  $\text{NH}_3\text{-SCR}$ , methods for improving the selectivity at higher temperature should be investigated to broaden the range of optimized operation temperature.

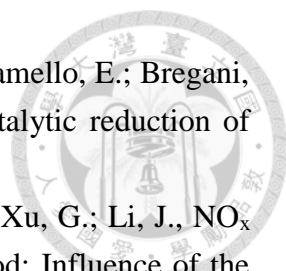


## Reference

1. Zhang, Y.; Yang, J.; Yu, X.; Sun, P.; Zhao, Y.; Zhang, J.; Chen, G.; Yao, H.; Zheng, C., Migration and emission characteristics of Hg in coal-fired power plant of China with ultra low emission air pollution control devices. *Fuel Processing Technology* **2017**, *158*, 272-280.
2. Domingo, J. L., Vanadium: A review of the reproductive and developmental toxicity. *Reproductive Toxicology* **1996**, *10* (3), 175-182.
3. Worle-Knirlschi, J. M.; Kern, K.; Schleh, C.; Adelhelm, C.; Feldmann, C.; Krug, H. F., Nanoparticulate Vanadium Oxide Potentiated Vanadium Toxicity in Human Lung Cells. *Environ Sci Technol* **2007**, *41*, 331-336.
4. Shen, B.; Zhang, X.; Ma, H.; Yao, Y.; Liu, T., A comparative study of Mn/CeO<sub>2</sub>, Mn/ZrO<sub>2</sub> and Mn/Ce-ZrO<sub>2</sub> for low temperature selective catalytic reduction of NO with NH<sub>3</sub> in the presence of SO<sub>2</sub> and H<sub>2</sub>O. *Journal of Environmental Sciences* **2013**, *25* (4), 791-800.
5. Fan, Y.; Ling, W.; Huang, B.; Dong, L.; Yu, C.; Xi, H., The synergistic effects of cerium presence in the framework and the surface resistance to SO<sub>2</sub> and H<sub>2</sub>O in NH<sub>3</sub>-SCR. *Journal of Industrial and Engineering Chemistry* **2017**, *56*, 108-119.
6. Xiao, X.; Sheng, Z.; Yang, L.; Dong, F., Low-temperature selective catalytic reduction of NO<sub>x</sub> with NH<sub>3</sub> over a manganese and cerium oxide/graphene composite prepared by a hydrothermal method. *Catalysis Science & Technology* **2016**, *6* (5), 1507-1514.
7. You, X.; Sheng, Z.; Yu, D.; Yang, L.; Xiao, X.; Wang, S., Influence of Mn/Ce ratio on the physicochemical properties and catalytic performance of graphene supported MnO<sub>x</sub>-CeO<sub>2</sub> oxides for NH<sub>3</sub>-SCR at low temperature. *Applied Surface Science* **2017**, *423*, 845-854.
8. Kroll, J. H.; Seinfeld, J. H., Chemistry of secondary organic aerosol: Formation and evolution of low-volatility organics in the atmosphere. *Atmospheric Environment* **2008**, *42* (16), 3593-3624.
9. USEPA, Nitrogen Oxides (NO<sub>x</sub>), Why and How They Are Controlled. *EPA technical bulletin* **1999**.
10. Toof, J. L., A Model for the Prediction of Thermal, Prompt, and Fuel NO<sub>x</sub> Emissions From Combustion Turbines. *Journal of Engineering for Gas Turbines and Power* **1986**, *108* (2), 340-347.
11. Miller, J. A.; Bowman, C. T., Mechanism and modeling of nitrogen chemistry in combustion. *Progress in Energy and Combustion Science* **1989**, *15*, 287-338.

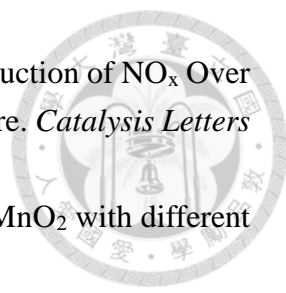
- 
12. Miller, S. F.; Miller, B. G., Advanced flue gas cleaning systems for sulfur oxides (SO<sub>x</sub>), nitrogen oxides (NO<sub>x</sub>) and mercury emissions control in power plants. *Advanced Power Plant Materials, Design and Technology* **2010**, 187-216.
  13. Sun, Y.; Zwolińska, E.; Chmielewski, A. G., Abatement technologies for high concentrations of NO<sub>x</sub> and SO<sub>2</sub> removal from exhaust gases: A review. *Critical Reviews in Environmental Science and Technology* **2015**, 46 (2), 119-142.
  14. Ding, J.; Zhong, Q.; Zhang, S.; Song, F.; Bu, Y., Simultaneous removal of NO<sub>x</sub> and SO<sub>2</sub> from coal-fired flue gas by catalytic oxidation-removal process with H<sub>2</sub>O<sub>2</sub>. *Chemical Engineering Journal* **2014**, 243, 176-182.
  15. Mondal, M. K.; Chelluboyana, V. R., New experimental results of combined SO<sub>2</sub> and NO removal from simulated gas stream by NaClO as low-cost absorbent. *Chemical Engineering Journal* **2013**, 217, 48-53.
  16. Long, X. L.; Xiao, W. D.; Yuan, W. K., Simultaneous absorption of NO and SO<sub>2</sub> into hexamminecobalt(II)/iodide solution. *Chemosphere* **2005**, 59 (6), 811-7.
  17. Wilde, J. D.; Marin, G. B., Investigation of simultaneous adsorption of SO<sub>2</sub> and NO<sub>x</sub> on Na-g-alumina with transient techniques. *Catalysis Today* **2000**, 62, 319-328.
  18. Gao, S.; Nakagawa, N.; Kato, K.; Inomata, M.; Tsuchiya, F., Simultaneous SO<sub>2</sub>/NO<sub>x</sub> removal by a powder-particle fluidized bed. *Catalysis Today* **1996**, 165-169.
  19. Chmielewski, A. G.; Sun, Y.; Licki, J.; Pawelec, A.; Witman, S.; Zimek, Z., Electron beam treatment of high NO<sub>x</sub> concentration off-gases. *Radiation Physics and Chemistry* **2012**, 81 (8), 1036-1039.
  20. Radoiu, M. T.; Martin, D. I.; Calinescu, I., Emission control of SO<sub>2</sub> and NO<sub>x</sub> by irradiation methods. *Journal of Hazardous Materials* **2003**, 145-158.
  21. Busca, G.; Berti, L. L. G. R. F., Chemical and mechanistic aspects of the selective catalytic reduction of NO<sub>x</sub> by ammonia over oxide catalysts: A review. *Applied Catalysis B: Environmental* **1998**, 18, 1-36.
  22. Zhang, S.; Zhang, B.; Liu, B.; Sun, S., A review of Mn-containing oxide catalysts for low temperature selective catalytic reduction of NO<sub>x</sub> with NH<sub>3</sub>: reaction mechanism and catalyst deactivation. *RSC Advances* **2017**, 7 (42), 26226-26242.
  23. Cho, S. M., Properly apply selective catalytic reduction for NO<sub>x</sub> removal. *Chemical Engineering Progress* **1994**, 90 (1), 39.
  24. Forzatti, P.; Lietti, L., Recent advances in de-NO<sub>x</sub>ing catalysis for stationary applications. *Heterogeneous Chemistry Reviews* **1996**, 3 (1), 33-51.
  25. Yang, S.; Xiong, S.; Liao, Y.; Xiao, X.; Qi, F.; Peng, Y.; Fu, Y.; Shan, W.; Li, J., Mechanism of N<sub>2</sub>O formation during the low-temperature selective catalytic reduction of NO with NH<sub>3</sub> over Mn-Fe spinel. *Environ. Sci. Technol.* **2014**, 48 (17),

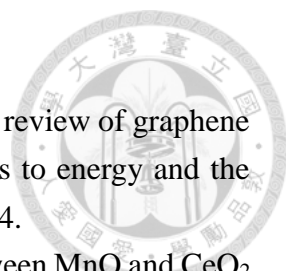
- 10354-10362.
26. Yang, S.; Qi, F.; Xiong, S.; Dang, H.; Liao, Y.; Wong, P. K.; Li, J., MnO<sub>x</sub> supported on Fe–Ti spinel: A novel Mn based low temperature SCR catalyst with a high N<sub>2</sub> selectivity. *Applied Catalysis B: Environmental* **2016**, *181*, 570-580.
27. Qi, G.; Yang, R. T., Characterization and FTIR Studies of MnO<sub>x</sub>-CeO<sub>2</sub> Catalyst for Low-Temperature Selective Catalytic Reduction of NO with NH<sub>3</sub>. *J. Phys. Chem. B* **2004**, *108* (40), 15738-15747.
28. Liu, Z.; Su, H.; Chen, B.; Li, J.; Woo, S. I., Activity enhancement of WO<sub>3</sub> modified Fe<sub>2</sub>O<sub>3</sub> catalyst for the selective catalytic reduction of NO<sub>x</sub> by NH<sub>3</sub>. *Chemical Engineering Journal* **2016**, *299*, 255-262.
29. Xiong, S.; Liao, Y.; Xiao, X.; Dang, H.; Yang, S., Novel Effect of H<sub>2</sub>O on the Low Temperature Selective Catalytic Reduction of NO with NH<sub>3</sub> over MnO<sub>x</sub>-CeO<sub>2</sub>: Mechanism and Kinetic Study. *J. Phys. Chem. C* **2015**, *119* (8), 4180-4187.
30. Zhou, G.; Zhong, B.; Wang, W.; Guan, X.; Huang, B.; Ye, D.; Wu, H., In situ DRIFTS study of NO reduction by NH<sub>3</sub> over Fe–Ce–Mn/ZSM-5 catalysts. *Catalysis Today* **2011**, *175* (1), 157-163.
31. Nova, I.; Ciardelli, C.; Tronconi, E.; Chatterjee, D.; Bandl-Konrad, B., NH<sub>3</sub>–NO/NO<sub>2</sub> chemistry over V-based catalysts and its role in the mechanism of the Fast SCR reaction. *Catalysis Today* **2006**, *114* (1), 3-12.
32. Marbán, G.; Valdés-Solís, T.; Fuertes, A. B., Mechanism of low-temperature selective catalytic reduction of NO with NH<sub>3</sub> over carbon-supported Mn<sub>3</sub>O<sub>4</sub> Role of surface NH<sub>3</sub> species: SCR mechanism. *Journal of Catalysis* **2004**, *226* (1), 138-155.
33. Grossale, A.; Nova, I.; Tronconi, E.; Chatterjee, D.; Weibel, M., The chemistry of the NO/NO<sub>2</sub>–NH<sub>3</sub> “fast” SCR reaction over Fe-ZSM5 investigated by transient reaction analysis. *Journal of Catalysis* **2008**, *256* (2), 312-322.
34. Liu, Z.; Chen, C.; Zhao, J.; Yang, L.; Sun, K.; Zeng, L.; Pan, Y.; Liu, Y.; Liu, C., Study on the NO<sub>2</sub> production pathways and the role of NO<sub>2</sub> in fast selective catalytic reduction DeNO<sub>x</sub> at low-temperature over MnO<sub>x</sub>/TiO<sub>2</sub> catalyst. *Chemical Engineering Journal* **2020**, *379*, 122288.
35. Jiang, L.; Liu, Q.; Ran, G.; Kong, M.; Ren, S.; Yang, J.; Li, J., V<sub>2</sub>O<sub>5</sub>-modified Mn-Ce/AC catalyst with high SO<sub>2</sub> tolerance for low-temperature NH<sub>3</sub>-SCR of NO. *Chemical Engineering Journal* **2019**, *370*, 810-821.
36. Ramis, G.; Busca, G.; Bregani, F.; Forzatti, P., Fourier Transform-Infrared Study of the Adsorption and Coadsorption of Nitric Oxide, Nitrogen Dioxide and Ammonia on Vanadia-Titania and Mechanism of Selective Catalytic Reduction. *Applied Catalysis* **1990**, *64*, 259-278.

- 
37. Lietti, L.; Alemany, J. L.; Forzatti, P.; Busca, G.; Ramis, G.; Giamello, E.; Bregani, F., Reactivity of V<sub>2</sub>O<sub>5</sub>-WO<sub>3</sub>/TiO<sub>2</sub> catalysts in the selective catalytic reduction of nitric oxide by ammonia. *Catalysis Today* **1996**, 143-148.
38. Gan, L.; Chen, J.; Peng, Y.; Yu, J.; Tran, T.; Li, K.; Wang, D.; Xu, G.; Li, J., NO<sub>x</sub> Removal over V<sub>2</sub>O<sub>5</sub>/WO<sub>3</sub>-TiO<sub>2</sub> Prepared by a Grinding Method: Influence of the Precursor on Vanadium Dispersion. *Industrial & Engineering Chemistry Research* **2017**, 57 (1), 150-157.
39. Ramis, G.; Yi, L.; Busca, G., Ammonia activation over catalysts for the selective catalytic reduction of NO, and the selective catalytic oxidation of NH<sub>3</sub>. An FT-IR study. *Catalysis Today* **1996**, 28, 373-380.
40. Li, X.; Li, K.; Peng, Y.; Li, X.; Zhang, Y.; Wang, D.; Chen, J.; Li, J., Interaction of phosphorus with a FeTiO<sub>x</sub> catalyst for selective catalytic reduction of NO<sub>x</sub> with NH<sub>3</sub>: Influence on surface acidity and SCR mechanism. *Chemical Engineering Journal* **2018**, 347, 173-183.
41. Trombett, M.; Ramis, G.; Busca, G.; Montanari, B.; Vaccari, A., Ammonia Adsorption and Oxidation on Cu/Mg/Al Mixed Oxide Catalysts Prepared via Hydrotalcite-Type Precursors. *Langmuir* **1997**, 13, 4628-4637.
42. Amores, J. M. G.; Escribano, V. S.; Ramis, G.; Busca, G., An FT-IR study of ammonia adsorption and oxidation over anatase-supported metal oxides. *Applied Catalysis B: Environmental* **1997**, 13, 45-58.
43. Kijlstra, W. S.; Brands, D. S.; Poels, E. K.; Bliet, A., Mechanism of the Selective Catalytic Reduction of NO by NH<sub>3</sub> over MnO<sub>x</sub>/Al<sub>2</sub>O<sub>3</sub>. *Journal of Catalysis* **1997**, 171, 208-218.
44. Liu, F.; He, H.; Zhang, C.; Shan, W.; Shi, X., Mechanism of the selective catalytic reduction of NO<sub>x</sub> with NH<sub>3</sub> over environmental-friendly iron titanate catalyst. *Catalysis Today* **2011**, 175 (1), 18-25.
45. Guo, R.-t.; Li, M.-y.; Sun, P.; Pan, W.-g.; Liu, S.-m.; Liu, J.; Sun, X.; Liu, S.-w., Mechanistic Investigation of the Promotion Effect of Bi Modification on the NH<sub>3</sub>-SCR Performance of Ce/TiO<sub>2</sub> Catalyst. *The Journal of Physical Chemistry C* **2017**, 121 (49), 27535-27545.
46. Liu, J.; Li, X.; Zhao, Q.; Ke, J.; Xiao, H.; Lv, X.; Liu, S.; Tadé, M.; Wang, S., Mechanistic investigation of the enhanced NH<sub>3</sub>-SCR on cobalt-decorated Ce-Ti mixed oxide: In situ FTIR analysis for structure-activity correlation. *Applied Catalysis B: Environmental* **2017**, 200, 297-308.
47. Gao, L.; Li, C.; Li, S.; Zhang, W.; Du, X.; Huang, L.; Zhu, Y.; Zhai, Y.; Zeng, G., Superior performance and resistance to SO<sub>2</sub> and H<sub>2</sub>O over CoO<sub>x</sub>-modified

- MnO<sub>x</sub>/biomass activated carbons for simultaneous Hg<sup>0</sup> and NO removal. *Chemical Engineering Journal* **2019**, 371, 781-795.
48. France, L. J.; Yang, Q.; Li, W.; Chen, Z.; Guang, J.; Guo, D.; Wang, L.; Li, X., Ceria modified FeMnO<sub>x</sub> —Enhanced performance and sulphur resistance for low-temperature SCR of NO<sub>x</sub>. *Applied Catalysis B: Environmental* **2017**, 206, 203-215.
49. Yang, Y.; Liu, J.; Liu, F.; Wang, Z.; Ding, J.; Huang, H., Reaction mechanism for NH<sub>3</sub>-SCR of NO<sub>x</sub> over CuMn<sub>2</sub>O<sub>4</sub> catalyst. *Chemical Engineering Journal* **2019**, 361, 578-587.
50. Zhu, L.; Zhong, Z.; Yang, H.; Wang, C., NH<sub>3</sub>-SCR Performance of Mn-Fe/TiO<sub>2</sub> Catalysts at Low Temperature in the Absence and Presence of Water Vapor. *Water, Air, & Soil Pollution* **2016**, 227 (12).
51. Heck, R. M., Catalytic abatement of nitrogen oxides—stationary applications. *Catalysis Today* **1999**, 53, 519–523.
52. Wu, Z.; Jiang, B.; Liu, Y.; Zhao, W.; Guan, B., Experimental study on a low-temperature SCR catalyst based on MnO<sub>x</sub>/TiO<sub>2</sub> prepared by sol-gel method. *J Hazard Mater* **2007**, 145 (3), 488-94.
53. Gao, C.; Shi, J.-W.; Fan, Z.; Gao, G.; Niu, C., Sulfur and Water Resistance of Mn-Based Catalysts for Low-Temperature Selective Catalytic Reduction of NO<sub>x</sub>: A Review. *Catalysts* **2018**, 8 (1), 11.
54. Lu, X.; Song, C.; Jia, S.; Tong, Z.; Tang, X.; Teng, Y., Low-temperature selective catalytic reduction of NO<sub>x</sub> with NH<sub>3</sub> over cerium and manganese oxides supported on TiO<sub>2</sub>–graphene. *Chemical Engineering Journal* **2015**, 260, 776-784.
55. Zhang, L.; Li, L.; Cao, Y.; Yao, X.; Ge, C.; Gao, F.; Deng, Y.; Tang, C.; Dong, L., Getting insight into the influence of SO<sub>2</sub> on TiO<sub>2</sub>/CeO<sub>2</sub> for the selective catalytic reduction of NO by NH<sub>3</sub>. *Applied Catalysis B: Environmental* **2015**, 165, 589-598.
56. Xu, W.; He, H.; Yu, Y., Deactivation of a Ce/TiO<sub>2</sub> Catalyst by SO<sub>2</sub> in the Selective Catalytic Reduction of NO by NH<sub>3</sub>. *J. Phys. Chem. C* **2009**, 113, 4426–4432.
57. Tang, X.; Li, C.; Yi, H.; Wang, L.; Yu, Q.; Gao, F.; Cui, X.; Chu, C.; Li, J.; Zhang, R., Facile and fast synthesis of novel Mn<sub>2</sub>CoO<sub>4</sub> @rGO catalysts for the NH<sub>3</sub>-SCR of NO<sub>x</sub> at low temperature. *Chemical Engineering Journal* **2018**, 333, 467-476.
58. Guo, K.; Fan, G.; Gu, D.; Yu, S.; Ma, K.; Liu, A.; Tan, W.; Wang, J.; Du, X.; Zou, W.; Tang, C.; Dong, L., Pore Size Expansion Accelerates Ammonium Bisulfate Decomposition for Improved Sulfur Resistance in Low-Temperature NH<sub>3</sub>-SCR. *ACS Appl Mater Interfaces* **2019**, 11 (5), 4900-4907.
59. Jiang, B. Q.; Wu, Z. B.; Liu, Y.; Lee, S. C.; Ho, W. K., DRIFT Study of the SO<sub>2</sub> Effect on Low-Temperature SCR Reaction over Fe-Mn/TiO<sub>2</sub>. *J. Phys. Chem. C* **2010**,

- 114, 4961–4965.
60. Guo, X.; Bartholomew, C.; Hecker, W.; Baxter, L. L., Effects of sulfate species on V<sub>2</sub>O<sub>5</sub>/TiO<sub>2</sub> SCR catalysts in coal and biomass-fired systems. *Applied Catalysis B: Environmental* **2009**, *92* (1-2), 30-40.
61. Peng, Y.; Wang, D.; Li, B.; Wang, C.; Li, J.; Crittenden, J.; Hao, J., Impacts of Pb and SO<sub>2</sub> Poisoning on CeO<sub>2</sub>-WO<sub>3</sub>/TiO<sub>2</sub>-SiO<sub>2</sub> SCR Catalyst. *Environ Sci Technol* **2017**, *51* (20), 11943-11949.
62. Jin, R.; Liu, Y.; Wang, Y.; Cen, W.; Wu, Z.; Wang, H.; Weng, X., The role of cerium in the improved SO<sub>2</sub> tolerance for NO reduction with NH<sub>3</sub> over Mn-Ce/TiO<sub>2</sub> catalyst at low temperature. *Applied Catalysis B: Environmental* **2014**, *148-149*, 582-588.
63. Esch, F.; Fabris, S.; Zhou, L.; Montini, T.; Africh, C.; Fornasiero, P.; Comelli, G.; Rosei, R., Electron Localization Determines Defect Formation on Ceria Substrates. *Science* **2005**, *309* (5735), 752-755.
64. Liu, Z.; Zhu, J.; Li, J.; Ma, L.; Woo, S. I., Novel Mn-Ce-Ti mixed-oxide catalyst for the selective catalytic reduction of NO<sub>x</sub> with NH<sub>3</sub>. *ACS Appl Mater Interfaces* **2014**, *6* (16), 14500-8.
65. Chang, H.; Wu, Q.; Zhang, T.; Li, M.; Sun, X.; Li, J.; Duan, L.; Hao, J., Design Strategies for CeO<sub>2</sub>-MoO<sub>3</sub> Catalysts for DeNO<sub>x</sub> and Hg<sup>0</sup> Oxidation in the Presence of HCl: The Significance of the Surface Acid-Base Properties. *Environ Sci Technol* **2015**, *49* (20), 12388-94.
66. Thirupathi, B.; Smirniotis, P. G., Co-doping a metal (Cr, Fe, Co, Ni, Cu, Zn, Ce, and Zr) on Mn/TiO<sub>2</sub> catalyst and its effect on the selective reduction of NO with NH<sub>3</sub> at low-temperatures. *Applied Catalysis B: Environmental* **2011**, *110*, 195-206.
67. Yao, X.; Kong, T.; Yu, S.; Li, L.; Yang, F.; Dong, L., Influence of different supports on the physicochemical properties and denitration performance of the supported Mn-based catalysts for NH<sub>3</sub>-SCR at low temperature. *Applied Surface Science* **2017**, *402*, 208-217.
68. Shu, Y.; Zhang, F.; Wang, H., Manganese–cerium mixed oxides supported on rice husk based activated carbon with high sulfur tolerance for low-temperature selective catalytic reduction of nitrogen oxides with ammonia. *RSC Advances* **2019**, *9* (41), 23964-23972.
69. Hummers, W. S.; Offeman, R. E., Preparation of graphitic oxide. *J. Am. Chem. Soc.* **1958**, *80*, 1339.
70. Achari, A.; Datta, K. K.; De, M.; Dravid, V. P.; Eswaramoorthy, M., Amphiphilic aminoclay-RGO hybrids: a simple strategy to disperse a high concentration of RGO in water. *Nanoscale* **2013**, *5* (12), 5316-20.

- 
71. Su, W.; Lu, X.; Jia, S.; Wang, J.; Ma, H.; Xing, Y., Catalytic Reduction of NO<sub>x</sub> Over TiO<sub>2</sub>-Graphene Oxide Supported with MnO<sub>x</sub> at Low Temperature. *Catalysis Letters* **2015**, *145* (7), 1446-1456.
72. Chen, H.; Wang, Y.; Lv, Y.-K., Catalytic oxidation of NO over MnO<sub>2</sub> with different crystal structures. *RSC Advances* **2016**, *6* (59), 54032-54040.
73. 溫桓正; 李建平; 蔡慶達; 杜悅元, 台中發電廠五至八號機 SCR 脫硝效率提升報告. *The Combustion Institute of R.O.C.* **2002**, *11* (1), 16-26.
74. Zhao, B.; Ran, R.; Wu, X.; Weng, D., Phase structures, morphologies, and NO catalytic oxidation activities of single-phase MnO<sub>2</sub> catalysts. *Applied Catalysis A: General* **2016**, *514*, 24-34.
75. Wang, H.; Chen, H.; Wang, Y.; Lyu, Y.-K., Performance and mechanism comparison of manganese oxides at different valence states for catalytic oxidation of NO. *Chemical Engineering Journal* **2019**, *361*, 1161-1172.
76. Wang, W.; Guo, R.; Pan, W.; Hu, G., Low temperature catalytic oxidation of NO over different-shaped CeO<sub>2</sub>. *Journal of Rare Earths* **2018**, *36* (6), 588-593.
77. Jia, J.; Ran, R.; Guo, X.; Wu, X.; Chen, W.; Weng, D., Enhanced low-temperature NO oxidation by iron-modified MnO<sub>2</sub> catalysts. *Catalysis Communications* **2019**, *119*, 139-143.
78. Yang, J.; Ren, S.; Zhang, T.; Su, Z.; Long, H.; Kong, M.; Yao, L., Iron doped effects on active sites formation over activated carbon supported Mn-Ce oxide catalysts for low-temperature SCR of NO. *Chemical Engineering Journal* **2020**, *379*, 122398.
79. Liu, C.; Shi, J.-W.; Gao, C.; Niu, C., Manganese oxide-based catalysts for low-temperature selective catalytic reduction of NO<sub>x</sub> with NH<sub>3</sub>: A review. *Applied Catalysis A: General* **2016**, *522*, 54-69.
80. Gao, Y.; Luan, T.; Zhang, W.; Li, H., The promotional effects of cerium on the catalytic properties of Al<sub>2</sub>O<sub>3</sub>-supported MnFeO<sub>x</sub> for NO oxidation and fast SCR reaction. *Research on Chemical Intermediates* **2018**, *45* (2), 663-686.
81. Gu, T.; Liu, Y.; Weng, X.; Wang, H.; Wu, Z., The enhanced performance of ceria with surface sulfation for selective catalytic reduction of NO by NH<sub>3</sub>. *Catalysis Communications* **2010**, *12* (4), 310-313.
82. Ma, S.; Tan, H.; Li, Y.; Wang, P.; Zhao, C.; Niu, X.; Zhu, Y., Excellent low-temperature NH<sub>3</sub>-SCR NO removal performance and enhanced H<sub>2</sub>O resistance by Ce addition over the Cu<sub>0.02</sub>Fe<sub>0.2</sub>Ce<sub>y</sub>Ti<sub>1-y</sub>O<sub>x</sub> (y = 0.1, 0.2, 0.3) catalysts. *Chemosphere* **2020**, *243*, 125309.
83. Jiang, D.; Zhang, S.; Zeng, Y.; Wang, P.; Zhong, Q., Active Site of O<sub>2</sub> and Its Improvement Mechanism over Ce-Ti Catalyst for NH<sub>3</sub>-SCR Reaction. *Catalysts*

- 
- 2018**, 8 (8), 336.
84. Chabot, V.; Higgins, D.; Yu, A.; Xiao, X.; Chen, Z.; Zhang, J., A review of graphene and graphene oxide sponge: material synthesis and applications to energy and the environment. *Energy & Environmental Science* **2014**, 7 (5), 1564.
85. Wu, X.; Yu, H.; Weng, D.; Liu, S.; Fan, J., Synergistic effect between MnO and CeO<sub>2</sub> in the physical mixture: Electronic interaction and NO oxidation activity. *Journal of Rare Earths* **2013**, 31 (12), 1141-1147.
86. Liang, H.; Hong, Y.; Zhu, C.; Li, S.; Chen, Y.; Liu, Z.; Ye, D., Influence of partial Mn-substitution on surface oxygen species of LaCoO<sub>3</sub> catalysts. *Catalysis Today* **2013**, 201, 98-102.
87. Zhang, X.-m.; Deng, Y.-Q.; Tian, P.; Shang, H.-h.; Xu, J.; Han, Y.-F., Dynamic active sites over binary oxide catalysts: In situ/operando spectroscopic study of low-temperature CO oxidation over MnO<sub>x</sub>-CeO<sub>2</sub> catalysts. *Applied Catalysis B: Environmental* **2016**, 191, 179-191.
88. Li, X.; Zhang, S.; Jia, Y.; Liu, X.; Zhong, Q., Selective catalytic oxidation of NO with O<sub>2</sub> over Ce-doped MnO<sub>x</sub>/TiO<sub>2</sub> catalysts. *Journal of Natural Gas Chemistry* **2012**, 21 (1), 17-24.
89. Park, T. S.; Jeong, S. K.; Hong, S. H.; Hong, S. C., Selective Catalytic Reduction of Nitrogen Oxides with NH<sub>3</sub> over Natural Manganese Ore at Low Temperature. *Ind. Eng. Chem. Res* **2001**, 40 (21), 4491-4495.
90. Gao, F.; Tang, X.; Yi, H.; Li, J.; Zhao, S.; Wang, J.; Chu, C.; Li, C., Promotional mechanisms of activity and SO<sub>2</sub> tolerance of Co-or Ni-doped MnO<sub>x</sub>-CeO<sub>2</sub> catalysts for SCR of NO<sub>x</sub> with NH<sub>3</sub> at low temperature. *Chemical Engineering Journal* **2017**, 317, 20-31.
91. Zhang, H.; Zou, Y.; Peng, Y., Influence of sulfation on CeO<sub>2</sub>-ZrO<sub>2</sub> catalysts for NO reduction with NH<sub>3</sub>. *Chinese Journal of Catalysis* **2017**, 38 (1), 160-167.
92. Costa, C. N.; Savva, P. G.; Fierro, J. L. G.; Efstathiou, A. M., Industrial H<sub>2</sub>-SCR of NO on a novel Pt/MgO-CeO<sub>2</sub> catalyst. *Applied Catalysis B: Environmental* **2007**, 75 (3-4), 147-156.